An experimentally validated continuum damage mechanics model of the micro-damage process zone during cortical bone fracture

by

Daniel Yaw Dapaah

A thesis

presented to the University Of Waterloo

in fulfilment of the

thesis requirement for the degree of

Master of Applied Science

in

Systems Design Engineering

Waterloo, Ontario, Canada, 2018

Author’s declaration

I hereby declare that I am the sole author of this thesis. This is a true copy of the thesis, including any required final revisions, as accepted by my examiners.

I understand that my thesis may be made electronically available to the public.

Abstract

Bone fractures remain a significant concern worldwide especially with aging and bone damaging diseases. These fractures not only lead to a high rate of morbidity and mortality but also place a considerable burden on the economy. This burden is as a result of the unmet need for better mechanical tools for predictive and preventive measures of bone fractures. This can be traced to the fact that there is still an incomplete mechanistic understanding of how bone resists fracture, specifically not understanding what changes cause fracture resistance to decline with aging and in bone damaging diseases. In this study, a continuum damage mechanics (CDM) approach was investigated to model the microdamage process zone (MDPZ), a primary toughening mechanism in cortical bone fracture. The CDM model was then validated against experimentally generated microdamage process zones using digital image correlation. The CDM model was able to replicate MDPZ formation observed experimentally. Results demonstrate that continuum damage mechanics provides a robust means of modelling the microdamage process zone in cortical bone fracture. With further development this work could yield a useful tool to better understand the fracture process in cortical bone in terms of its MDPZ formation.

Acknowledgements

First, my profound gratitude goes to my supervisor, Dr. Thomas Willett, for his guidance, expertise, encouragement, thoughtful questions and suggestions as well as his ever-present assistance in completing this study. This study would not have been possible without you. I would also like to thank Dr. John Montesano, a collaborator on this study, for his assistance and very helpful inputs. To Aram Bahmani and Raphael Badaoui, I express my gratitude, for your technical input, advice and encouragement on this journey. I would like to also thank my committee members, Dr. Maud Gorbet and Dr. Stewart McLachlin for their time in reviewing and offering comments and feedback on this work. I will also like to thank all my friends especially my lab group members for their support. Lastly, I would like to express immense gratitude to my family especially my parents who without them my dream of pursuing a Masters' degree would not be possible.

Table of Contents

List of figures

List of tables

List of abbreviations

2D	two-dimensional
CAD	Canadian dollar
CDM	continuum damage mechanics
CNC	computer numerical control
CZM	cohesive zone model/modelling
DEXA	dual energy X-ray absorptiometry
DIC	digital image correlation
EPFM	elastic plastic fracture mechanics
FE	finite element
FEM	finite element method
HA	hydroxyapatite
LEFM	linear elastic fracture mechanics
MDPZ	microdamage process zone
ROI	region of interest
SENB	single-edged notched bending
XFEM	extended finite element method

Chapter 1

Introduction

1.1 Motivation

The most critical failure mode in bone, the major load bearing organ in the human body, is fracture (Figure 1.1). Roughly 8.9 million bone fractures occur worldwide annually [1]. Not only does the high occurrence of bone fractures lead to morbidity and mortality [2], it places a high financial burden on the world's economy. For instance, 650 million Canadian dollars are spent in treating approximately 30,000 hip fractures and their related implications annually in Canada[3]. If not alarming enough, the figure is projected to increase to $2.4 billion CAD by 2041[3]. The major reason for the four-fold increase in the projected cost is the expected increase in the segment of the population over 65 years old. In the next 25 years, the population over 65 years old in Canada is expected to double and this will represent 25% of the entire population [4]. Though a number of factors contribute to the elderly population (over 65 years old) having the highest risk of bone fracture, a major contributor is the deterioration of the bone tissue's mechanical competence [5,6]. Competence of bone was attributed to loss of bone mineral density as one ages, with a relationship found between bone mineral density and fracture risk [7]. Consequently, current clinical tools examine bone mineral density to predict fracture risk [8]. However, there is a disproportion between bone density loss and bone strength decrease, with bone strength declining at a faster rate than bone density with aging [9]. Furthermore, Hui et al. uncovered that, independent of bone mineral density measures, there is about a ten-fold increase in fracture risk with aging [6]. More so, in certain diseases, such as diabetes and kidney disorders, there is a higher risk of fracture without a significant decrease in bone mass density [10,11]. This has led to the

Figure 1.1: A femoral fracture. Licensed under CC-BY-SA [133]

general conclusion that bone mineral density is not the sole indicator of fracture risk. Recent studies on bone fracture have consequently shifted focus from just bone mineral density to a broader term “bone quality” which encompasses the constituents of bone (mainly hydroxyapatite crystals and collagen) and their arrangement at the different length scales including the presence of pores and flaws [12–15]. Despite this shift, there is still no consensus on the mechanisms taking place to cause increased fracture risk with aging and in bone damaging diseases. In addition, there is still an unmet need for better mechanical tools for predictive and preventive measures in terms of bone fracture. The two highlighted issues can be traced to the fact that there is still not a complete mechanistic understanding of how bones resist fracture. A more complete understanding of this will better inform the possible changes occurring in the bone tissue to result in its declining fracture resistance with aging and in bone damaging diseases. Therefore, there is a need for further studies to gain a better mechanistic understanding of the fracture resistance mechanisms of bone.

1.2 Composition and structure of bone

Bone is a very important organ as it does not only have structural functions but also biological and chemical functions. Its main function is to provide support to the framework of the body but it also serves as a mineral reservoir and regulator for certain ions such as calcium and phosphate, the initiating site for the formation of blood cells, as well as providing mechanical protection for other vital organs in living organisms [16].

The building blocks of bone can be divided into three major phases: an inorganic phase, an organic phase and a fluid phase. They constitute roughly by volume, 45%, 45% and 10% of bone respectively [17]. The inorganic phase is made of carbonated apatite crystals known as hydroxyapatite [$Ca_5(PO_4,CO_3)_3(OH)$]. The organic phase consists of type-I collagen, making up about 90% of this phase with the remaining portion consisting of non-collagenous proteins such as osteocalcin, osteopontin, sialoprotein and osteonectin [16]. The fluid phase is basically water.

Bone is considered as a natural fiber reinforced composite material because of its structural organization [18]. It has a hierarchal structure with unique structural organization at different length scales. Hence the structure can be described by defining the organization at these different length scales moving from the sub-nanoscale to macro-scale (Figure 1.2)

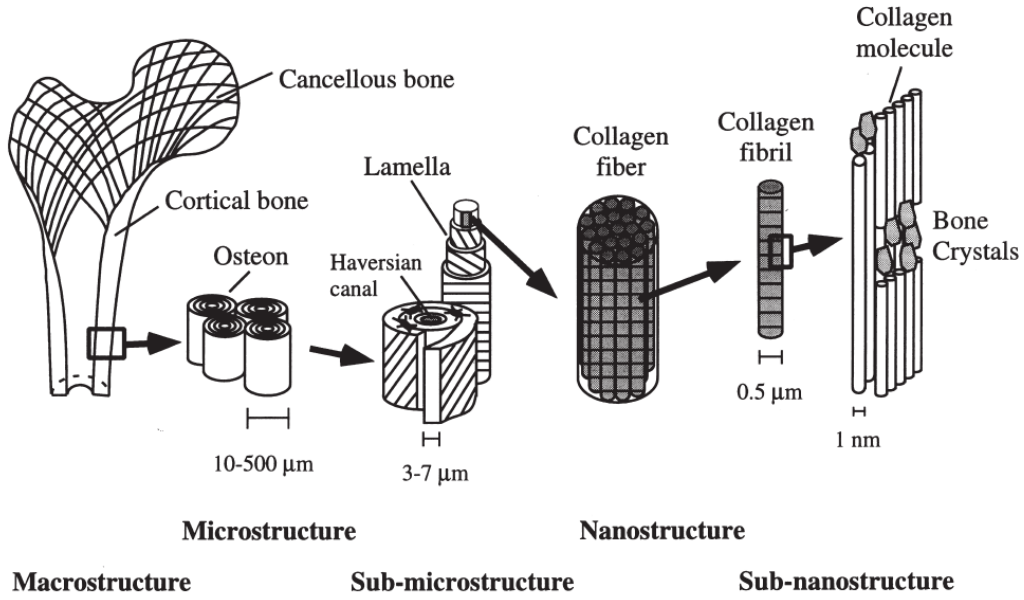

Figure 1.2: The different length scales structures of bone moving from the macroscale to sub-nanoscale. Reprinted from Rho et al.,1998 [16]

At the nanoscale level, cortical bone is characterized by its main constituents: the collagen molecules and hydroxyapatite crystals. The bone collagen molecule comprises three polypeptide chains which form a triple helical structure (Figure 1.3) [19,20]. This molecule, due to its structure, is cylindrically shaped with a radius and length of approximately 0.75 and 280 nm respectively [19–21]. The hydroxyapatite crystals, on the other hand, are plate-like shaped with average dimensions of 50×25×3nm [16,18–20]. These collagen molecules align parallel to each other but in a staggered manner with an offset of 67nm moving from one molecule to the next (Figure 1.3) [18,19]. Along the long axis of bone, the collagen molecules stack up on top of each other with the unique feature of gaps between one molecule to the next (Figure 1.3). The size of these gaps is between 35 to 40nm [18,19,22]. These gaps serve as sites for the formation of the hydroxyapatite (HA) crystals which become embedded in between the collagen molecules [12,19]. The crystals align with the long axis of the collagen molecules. The organisation of these staggered collagen molecules embedded with the hydroxyapatite crystals is referred to as the mineralised collagen

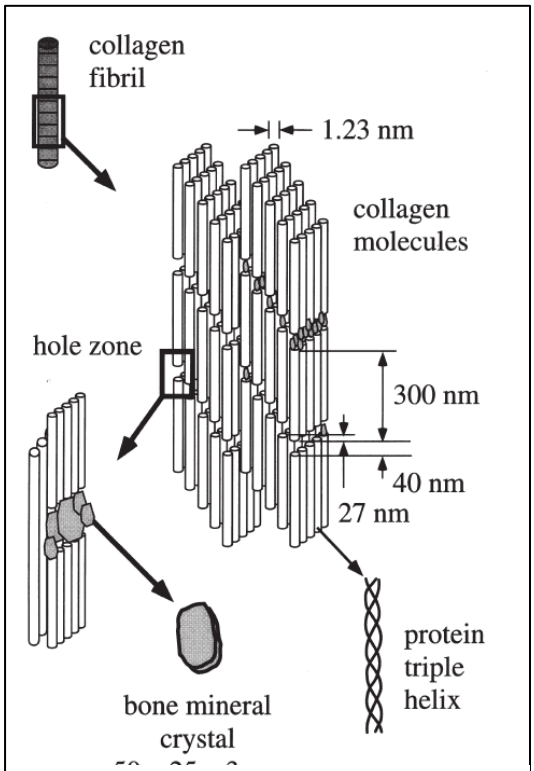

Figure 1.3: Organisation structure of collagen and crystals in the mineralised collagen fibril of bone. Reprinted from Rho et al.,1998 [16]

fibril [20]. These fibrils define the organisation at the sub-microscale level. These fibrils have a diameter between 0.5 to 1µm [20]. The collagen fibril becomes stronger and stiffer due to the mineralisation by the crystals [23]. Further, the rough alignment of the minerals with the long axis of the collagen fibril leads to the anisotropic nature of bone with the long axis direction of bone been stiffer and stronger compared to the direction perpendicular to the long axis [24].

At the microscale level, cylindrically shaped collagen fibers are formed by the mineralised collagen fibrils lining up parallel to each other [18,19,21]. These collagen fibers may then be organised in one of two ways. They may cluster into a well defined planar arrangement called lamellae which gives rise to lamellar bone or form an irregular configuration consequently forming woven bone [16]. Lamellar bone is more prevalent in cortical bone than woven bone[25]. The lamellae that may form are typically 3-7µm in thickness. The planar lamellae arrangement may then form plexiform or osteonal bone types [16,20]. Plexiform bone is more common in animals such as bovines but is not found in humans. . Plexiform bone has a brick-like structure with non lamellar bone layers sandwiching the lamellae [20]. Alternatively, 3 to 8 concentric layers of lamellae arrange around a canal which contains a blood vessel. This organisation of concentric layers of lamellae surrounding a blood vessel filled canal is known as Haversian systems or the osteon[16]. Osteons are the predominant microstructure in human bone and have also been observed in bovine bone. These arrange in the same direction as the long axis of the bone[16,20]. The osteon also has a cylindrical structure with a diameter in between 200- 250µm[16]. A popular concept in the arrangement of the collagen fibers in these lamellae of the osteon is the change in orientation of the fibers moving from one lamellae layer to the next (Figure 1.4). However, the collagen fibers are more or less parallel to each other in a specific lamella [16,26]. The orientation can reach an angle of ±30˚ with respect to the long axis of the osteon[20]. This configuration of neighbouring lamellae of an osteon

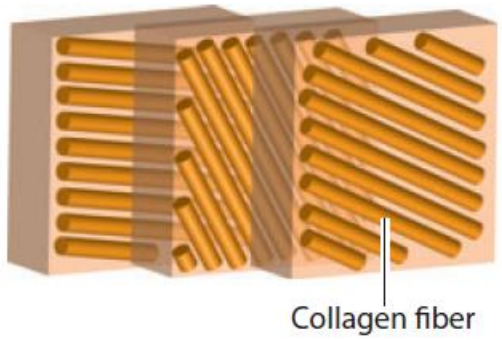

Figure 1.4: The arrangement of collagen fibers in adjacent lamellae of the osteon. Reprinted from Launey et al.,2010 [35]

portraying different progressive orientations from one to the next is known as the twisted plywood architecture[26]. At the same length scale of the lamellae, other structures which form part of the osteon exist. These are the cement lines, lacunae and canaliculi [25]. The cement line serves as the interface between the various layers of lamellae and have thickness between 1 to 5µm[27]. The bone cells known as osteocytes are found in the lacunae and canaliculi, which occur as holes in the micro-level organisation of the Haversian canal[28]. These osteocytes are matured osteoblasts. The osteoblasts are the bone making cells and they lay down the molecular building blocks for bone. During the process of mineralisation, the osteoblasts become trapped within the collagen fibrils which becomes holes called the lacunae and have a diameter ranging between 10 to 20µm [28]. The different lacunae are inter-connected by channels referred to as the canaliculi.

At the macroscale, bone can be categorised into cortical and trabecular bone. Cortical bone is typified by its defined osteonal arrangement; concentric layers of lamellae surrounding a blood and nerve filled channel. However, for trabecular bone, the lamellae align predominantly longitudinally instead of concentrically and form a cell foam matrix of collagen fiber rods and lamellae plates interconnected with each other [29]. The thickness of this foam-like structure is roughly 200µm[19]. A level of lacunae and its connecting canaliculi exist in the trabecular bone structure[19]. Further, due to the structure of the trabecular bone, it is more porous than the cortical bone reaching a porosity of almost 80% whereas the porosity of cortical bone is around 6% hence more dense and compact [19,29]. For long bones such as the humerus and femur and even to an extent in the vertebrae, the trabecular bone is surrounded by cortical bone and serves as an outer covering and shield for the more porous trabecular bone.

1.3 Cortical bone fracture

1.3.1 Basic concept of fracture

Cortical bone like other naturally occurring biological materials, has the unique feature of being stiff, strong and tough simultaneously, unlike structural engineering materials that often trade strength for toughness and vice versa [30]. However, it is highly susceptible to fractures due to the presence of numerous cracks and other stress concentrators in its structure. A stress concentrator is a void that causes a localised area of higher stress flow around it as compared to the rest of the material. The presence of flaws (voids) in materials are the basis from which fracture occurs. For a perfect material, the theoretical strength can be calculated as[31]:

$$\sigma_c = \frac{E}{10} \tag{1.1}$$

where σ_c represents the theoretical strength and E represents the Young's modulus.

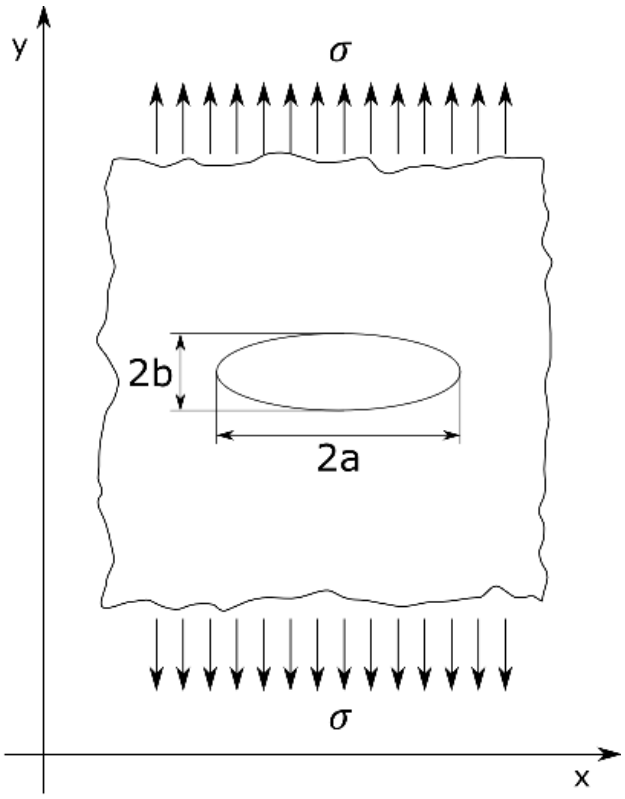

Figure 1.5: Infinite thin plate with crack showing the dimensions of the crack. Licensed under CC-BY-SA [134]

However, commercially produced materials do not obey this equation, as these materials fail/ fracture at stresses 10 to 100 times lower than their theoretical strength. This is mainly due to the presence of flaws in their structure serving as stress concentrators, hence failing at stresses far lower than theoretically, they should. From Griffith's work[32], a flaw will increase the stress around it by a factor of $(1 + \frac{2a}{b})$ as compared to the stress at a flawless area in an infinite plate, where a and b are half the length of the long and perpendicular axes of the flaw (Figure 1.5). For instance, for a circular hole in a plate (where a = b), the stress imposed around the hole is three times larger than that imposed in the regions further away from the hole with no flaws. For a crack, the variable b becomes very small and an infinitely large stress will be induced at that region of the material even with the smallest load applied, leading to instant failure. Therefore, the stress concentration factor stated $(1 + \frac{2a}{b})$ is impractical in terms of dealing with cracks as stress concentrators. Hence, other approaches in fracture mechanics are used to determine the stresses induced and will be discussed later. There are three main modes of fracture: Mode I, II and III [31]. Mode I is referred to as the opening mode and occurs when tensile loading is applied normal to the crack tip. Mode II is referred to as the shearing mode and occurs when in-plane shear stresses are applied parallel to the crack tip. Mode III is refereed to as the tearing mode and occurs when out of plane shear stresses are applied normal to the crack tip [31]. Despite, the above detailing how dire the presence of cracks is to bone in terms of fracture risk, bone employs fascinating mechanisms to increase its toughness to resist fracture.

1.3.2 Toughening mechanisms

For a fracture to occur, adequate energy is needed to create new crack surfaces across the cross-sectional area of the material. Anytime a material deforms elastically, it stores up elastic energy. If a portion of the material fails, a portion of the stored elastic energy is released. So, for a pre-existing crack to grow, the available elastic energy stored in the material must be equal or greater than the energy needed to create the new surfaces of the crack. To prevent cracks from propagating, bone employs various mechanisms to dissipate the stored elastic energy that would otherwise grow the crack, thereby toughening up the bone. The various mechanisms bone utilises to resist crack growth by dissipating the elastic energy stored is referred to as toughening mechanisms[33]. In bone, specifically cortical bone, toughening mechanisms can be put into two categories: intrinsic and extrinsic (Figure 1.6). Intrinsic toughening mechanisms occur before crack initiation. In other

words, these mechanisms take place to delay the start of crack growth. These mechanisms occur by engaging the structure of bone below the microscale level, predominantly, the mineralised collagen fibrils [34,35]. Due to the fact they slow down the commencement of crack growth, they typically occur ahead of the crack tip.

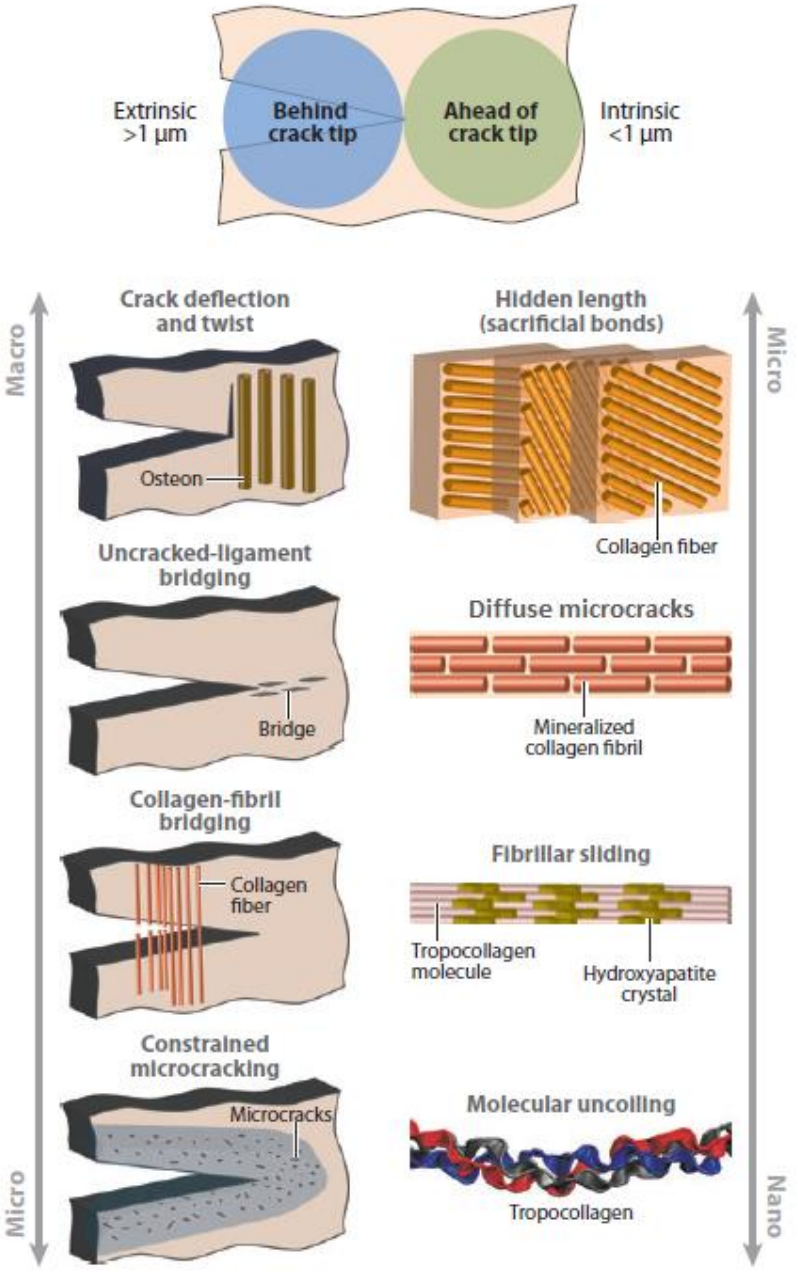

Figure 1.6: Intrinsic and extrinsic toughening mechanisms in cortical bone. Reprinted from Launey et al.,2010 [35]

The slowing down of crack growth is accomplished by irreversible deformation processes in the mineralised collagen fibers [33,35]. The primary means of this irreversible deformation is the uncoiling and extending of the individual collagen molecules in the mineralized collagen fibrils [23]. The hydrogen bonds between the three different amino acid chains that form the collagen molecule break apart after yielding, allowing the collagen molecule to stretch out depleting energy that will otherwise be available for crack growth [36].

In addition, there is sliding or breaking of bonds (crosslinks) between neighbouring collagen molecules also contributing to energy dissipation [33]. Furthermore, due to the stiffer and stronger nature of the hydroxyapatite particles, there is constant slipping and sliding at the junctions between the collagen molecules and the hydroxyapatite crystals in the mineralised collagen fibril as the collagen molecule unravels leading to a large amount of energy also been dissipated[23]. This sliding process at the junctions of the two main constituents of bone is the precursor for the creation of diffuse microcracks. These are voids in the bone structure ranging in a few tens of micrometers further dissipating energy [35]. These diffuse microcracks also serve as an intrinsic toughening mechanism. However, microcracking is a unique toughening mechanism because it qualifies also as an extrinsic toughening mechanism because it continues to form even after crack growth initiation. Sacrificial bonds are another dissipative mechanism that contributes to the intrinsic toughness of bone [37,38]. In the collagen fiber, the grouped mineralised collagen fibrils are bonded to each other by thin layers of the extrafibrillar matrix [38]. When the fibrils are stressed in tension, the extrafibrillar matrix which is acting as a glue between the fibrils is stressed in shear[39]. This causes the bonds at the interface between the extrafibrillar matrix and the fibrils to break at a force which is approximately 10% to 50% of what will be required to break the molecules in the mineralised collagen fibrils. After these bonds break, the extrafibrillar matrix been weak but very ductile, plastically deforms. The bond between the matrix and the fibrils are then reformed after the deformation [37,38]. This process of the matrix ‘sacrificing’ bonds, dissipates energy allowing the bone to further resist fracture. These intrinsic toughening mechanisms are important precursors that allow the formation of a local “damage” region around cracks in cortical bone. In other words, there is considerable localised failure around the region of the crack without large scale bone tissue failure [35].

For extrinsic toughening mechanisms, the bone engages structure at the microscale level and higher which is mainly the osteon/Haversian system [33,35]. Interestingly, these mechanisms occur after crack growth has initiated, with the organisation and structure of the osteons providing preferable pathways for crack propagation which tend to make fracture more difficult to occur. In other words, they act to slow down the crack from growing further and are crack path dependent. The mechanisms happen behind the crack tip or in the crack wake. These mechanisms act by shielding or diverting the growing crack tip from its driving force. As mentioned earlier, microcracking serves as both an intrinsic and extrinsic toughening mechanism. The cement line, which is the boundary between the osteon and the extracellular matrix of bone, provides the weakest path for crack growth due to its highly mineralised nature [40,41]. The cement line consequently is thought to be a site for the formation of numerous microcracks in the order of tens to hundreds of micrometers as means of both intrinsically and extrinsically resisting crack initiation and growth. Microcracks are thought to be important precursors to other extrinsic toughening mechanisms [41]. Crack bridging is considered the dominant extrinsic toughening mechanism during fracture in the longitudinal direction (long axis direction). In this direction, microcracks forming due to the presence of cracks along the cement line, lie in the same plane as the crack front. The microcracks then lead to the formation of smaller daughter cracks formed ahead of the single mother crack with unbroken or uncracked regions (regions with no small cracks) existing between these daughter cracks [14, 41–43]. These unbroken regions normally referred to as uncracked ligaments, bear a portion of the load, decreasing the force available to keep the mother crack growing and hence resisting fracture [34,41,43]. In addition, at a lesser length scale of a few micrometers, collagen fibrils may span the opening of the crack behind the crack tip and probably some of the larger microcracks providing closing traction forces that limit the driving force accessible to the crack tip [44]. Though for an isolated crack, this type of fibrillar or fiber bridging may be minimal in terms of providing fracture toughness, its collective effect in the many microcracks makes it significant [40]. It must be mentioned, though uncracked ligament bridging as well as fibril bridging are potent toughening mechanisms, they are less proficient as compared to crack deflection/twisting. This is the predominate mechanism in transverse directed fracture in bone. Crack deflection occurs due to the alignment of the osteons. When a crack is growing transversely, the osteons are aligned roughly perpendicular to it. That means the cement line which provides an easier route for crack growth is also perpendicular to the direction the crack

is growing. This causes the growing transverse crack to divert upon interaction with the cement lines which acts as a delamination barrier [33,35]. This greatly reduces the driving force available for crack growth as the growing crack deflects to a direction roughly perpendicular to the direction of the maximum tensile force [40,45]. For further crack growth, a greater force needs to be applied hence toughening the bone. This crack deflection leads to a highly twisted crack path for transverse fracture which is visible by its very rough fracture surfaces. It has been showed that for 500μm crack extension, the fracture toughness in the transverse direction is 500% greater than its equivalent in the longitudinal direction [40]. This is due to the orientation of the osteons, more specifically, the cement lines as described above and explains why bone is easier to split longitudinally than break transversely [40].

1.3.3 The role of collagen in fracture resistance

The presence of the hydroxyapatite crystals contributes largely to the stiffness and strength of cortical bone. On the contrary, the presence of type I collagen contributes significantly to bone's toughness. The ductile property of the collagen allows the bone tissue to sustain a considerable level of post yield behaviour in the longitudinal direction. As mentioned above, for intrinsic toughening, the collagen molecules are thought to unwind and stretch out, dissipating energy in the process, and preventing failure in the microstructure of bone. It has been shown for other similar natural materials that individual collagen molecules can attain up to 50% strain in tension before failure and they may reach an ultimate stress level of 10-20GPa [36,46]. As described above, the collagen fibrils may also span microcrack openings, providing traction forces that rid the crack of a portion of its driving force. Recently, it was shown that bone's collagen integrity correlates very well with its fracture toughness [47]. The collagen integrity was measured by a thermomechanical method known as hydrothermal isometric tension. Both the collagen integrity and fracture toughness of bone was found to decrease with age [47,48]. All of these show the significance of collagen to bone's ability to resist fracture.

1.3.4 Measuring bone fracture toughness

The putative importance of toughening mechanisms to bone's fracture resistance creates the necessity of quantifying them. The measure of bone's resistance to fracture is termed as bone's fracture toughness. Currently in clinical settings, an X-ray approach referred to as dual energy X-ray absorptiometry (DEXA) is commonly used in assessing the risk of fracture [15]. However, this

method works by quantifying the amount of radiative energy absorbed by the bone which is predominately done by the bone crystals, neglecting the contribution of bone's organic phase to bone's fracture toughness [49]. Due to this, DEXA, though it has been capable of predicting fracture in greatly depleted bone mass patients, has done a poor job predicting fracture risk on an individual patient basis [50]. In recent studies, to integrate the importance of the organic (mostly collagen) phase of bone, fracture mechanics approaches have been adopted to quantify fracture toughness in bone. Initially, a linear elastic fracture mechanics(LEFM) approach was used [51–53]. In linear elastic fracture mechanics, the stress and displacement fields local to a pre-existing crack tip are characterised by a parameter known as the stress intensity factor (K). This stress intensity gives a measure of how much more intense the stress at the crack tip region is compared to the nominal stress imposed further away from the crack. When the stress intensity factor is measured/calculated just before unstable crack growth (sudden fracture), it is referred to as the critical stress intensity factor (K_{1c}) and quantifies the fracture toughness of the material in question. Linear elastic fracture mechanics works on the assumption that the material is perfectly brittle and that there is no or very little inelasticity/plasticity before fracture. However, from section 1.3.1, bone is a microcracking material. The microcracks form a damage zone around the crack tip before crack growth initiation and increase as the bone undergoes stable crack growth. Since microcracking is an inelastic material behaviour, it renders linear elastic fracture mechanics as an inaccurate means of quantifying bone's fracture toughness. Consequently, in more recent studies there has been a shift to non-linear or elastic-plastic fracture mechanics approaches.

Nalla et al. [13,54], Vashishth et al. [55,56] and Malik et al. [57] investigated bone fracture resistance using K resistance curves, otherwise known as R curves. R curves work by evaluating the fracture resistance during stable crack growth. Hence, fracture toughness is not a single value but rather a curve. R curves are defined by plotting fracture resistance against the stable crack extension. In bone, due to the growing damage zone as stable crack growth occurs, there is greater energy dissipation leading to increased fracture resistance with crack extension. Hence bone is reported to have a rising R curve. Although this approach accounted for the increasing fracture resistance as the damage zone grows with crack extension, the underlying principle is still based on LEFM [31]. Hence it does not accurately predict fracture toughness as the damage zone leads to the re-distribution of the stress around the crack tip [58,59] (Figure 1.7).

Yan et al.[58] proposed the use of elastic plastic fracture mechanics (EPFM). This quantifies fracture toughness using the J-integral. It accounts for the energy dissipated both by elastic and plastic mechanisms, and therefore, accounting for large scale yielding effects on the fracture resistance of materials. Furthermore, this J-integral can be used with the concept of resistance curves to form J resistance curves, which evaluate the increasing fracture resistance with crack growth [15,60,61].

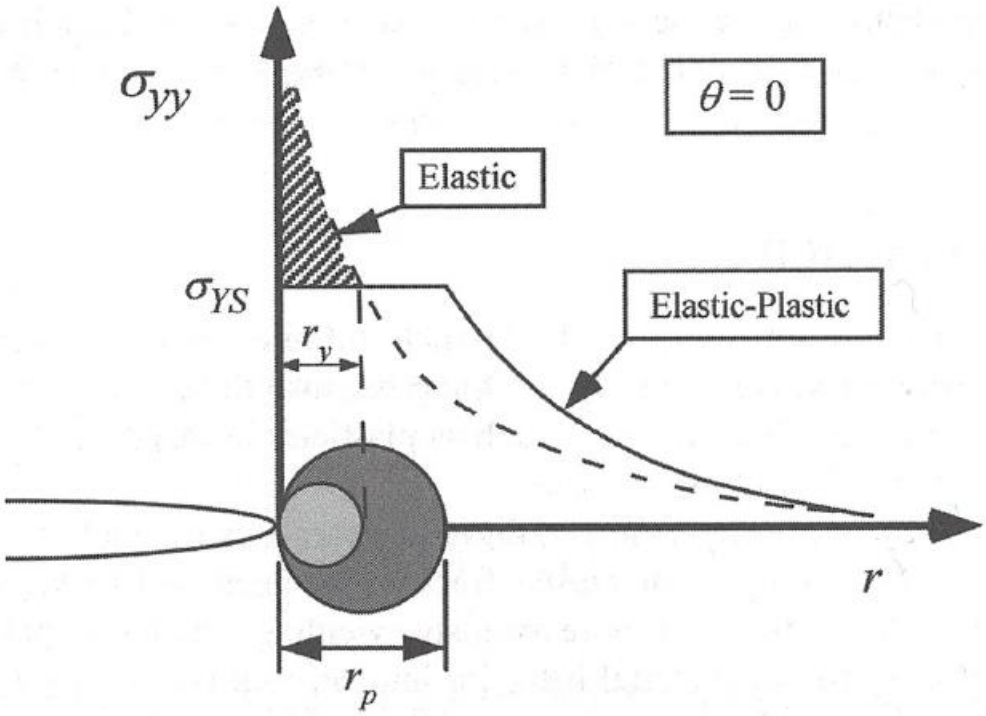

Figure 1.7: Stress re-distribution ahead of a crack tip due to the presence of a damage/plastic zone (represented by the more darkened circular zone). The broken line indicates the stress distribution if there was no plastic zone whiles the black solid line shows the re-distribution of stress with the presence of the damage/plastic zone. Reprinted from Anderson, 2005 [125]

Another approach that has been used to characterise bone's fracture behaviour is cohesive zone modelling (CZM) [14,63]. CZM operates by assuming two cohesive surfaces ahead of the crack tip. These cohesive surfaces are held together by cohesive traction forces (Figure 1.8). These traction forces are representative of the effective non-linear material behaviours (crazing in polymers, necking in metals or microcracking/bridging in quasi-brittle materials) have on the fracture process [31].

External loading acts against these cohesive forces, leading to the gradual separation of the two cohesive surfaces starting from the surfaces right ahead of the physical crack tip. This separation is reminiscent of crack growth. A cohesive law relates the traction forces to the relative displacement between the two surfaces and separation occurs when a critical displacement value is reached. The cohesive law is normally based on the energy dissipated to fracture.

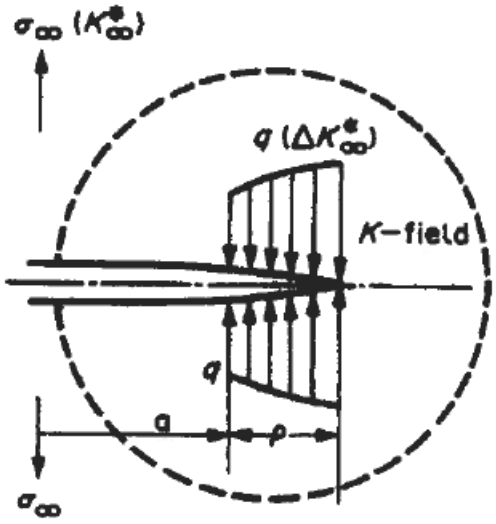

Figure 1.8: Cohesive zone model represented by traction forces on both sides of a crack that separate according to a cohesive law. Reprinted from Zhonghua et al,1993 [62]

A common feature of all these non-linear fracture mechanics approaches is the desire to better model the effect of the damage zone that forms ahead of the crack tip in cortical bone to its fracture resistance. The damage zone leads to two main effects: (1) a shift in the distribution of stress and strain fields ahead of the crack tip and (2) an increasing fracture toughness with crack extension.

These two consequences relay the importance of the damage zone, specifically its shape and size, to understanding and quantifying its contribution to the overall fracture resistance of bone.

1.4 The microdamage process zone

The concept of microcracking has been introduced as a toughening mechanism and stated to be vital to bone's fracture resistance. It impacts the fracture mechanics approaches that can be used to quantify bone's fracture toughness. The formation of microcracks leads to the development of a process zone around the crack tip (Figure 1.9). It has been proposed that this happens in two stages [64]. First, the formation of a frontal process zone ahead of the crack tip. This frontal process zone causes the bone material ahead of the crack tip to soften, eventually leading to the propagation of the crack. As the crack propagates, a second stage is engaged where microcracks reside in the wake of the crack [64,65].

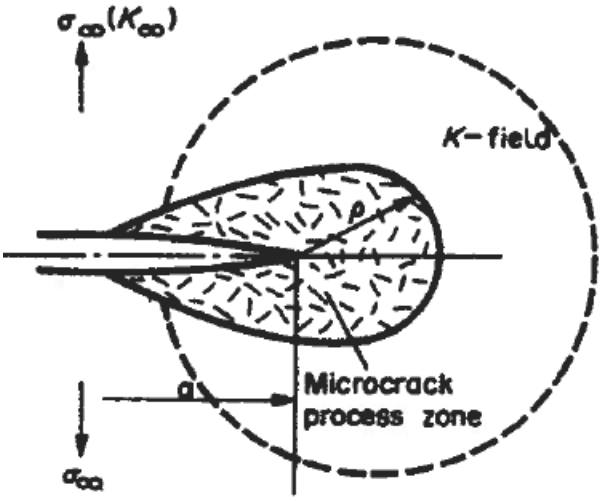

Figure 1.9: Process zone developed ahead of crack tip due to microcracking. Reprinted from Zhonghua et al,1993[62]

The region ahead of the crack softens as microcracking causes loss in apparent stiffness seen in a load-deflection curve in the "post-yield" region [66]. Interestingly, it has been found that the microcracks that form in cortical bone are of two distinct types: a linear type and more diffuse type[64]. The linear form referred to as linear microcracks was first observed using a staining technique developed by Frost then later improved by Burr and Stafford [64,67,68] and has been extensively studied in the past twenty years [55], [69–71]. The linear microcracks (Frost-Burr type) have a length between 60-130μm [65] making them bigger than a canaliculus but smaller than an osteon [64]. They are characterised by lines that are clearly defined and their edges stain more distinctly than the space between [68,72]. On the other hand, the diffuse type is made up of a network of fine submicroscopic cracks (<1μm) spread across a confined region [64,65,73].

The formation of linear microcracks has been found to correlate greatly with lamellar boundaries while the diffuse microcracks do not [74]. The diffuse microcracks transcend lamellar boundaries and therefore suggest that they form at a smaller length scale than the lamellae, that is, at the mineralised collagen fibril level [64]. Additionally, the diffuse type is considered a more effective

energy dissipative mechanism, as compared to the linear type [72]. It has therefore been suggested that the diffuse type may be a precursor for the linear type [64,75]. This is supported by a study that demonstrated that the early stages of bone's fatigue life is associated with diffuse form of microcrack whiles the later stage is associated with linear microcracks, which leads eventually to catastrophic fracture [72]. Further, in tensile loading of young bone, it has been shown that the microcracks formed were more of the diffuse type of microcracking [76]. Additionally, Akkus et al. [77] reported the diffuse type of microcrack formation when investigating fracture in both the transverse and longitudinal directions using histology. All these suggest that the formation of the process zone ahead and in the wake of a crack as a toughening mechanism, forms by means of this diffuse type of microcracking which eventually may grow into linear microcracks leading to frank crack formation and growth Hence, this study will deal with this diffuse type of microcracking as it is, essentially, the effective toughening mechanism of the two types. Because of the finer meshwork nature of the diffuse type of microcracking and to prevent confusion with the "more popular" linear microcracks, the process zone will be referred to as the microdamage process zone (MDPZ). This process zone is synonymous to the damage zone referred to in section 1.3.4.

Interestingly, the relative importance of microdamage to bone's fracture toughness has been questioned [42] and this might be because until recently the shape and size, which is important to its contribution in bone's fracture toughness was not known. Willett et al.[78] measured in detail, the size and shape of the MDPZ during transverse directed fracture in bovine bone. The MDPZ was imaged using barium sulphate staining and high resolution (3.5μm) micro-computed tomography (microCT). During the study, bovine tibia cortical bone was machined into single edged notched bending (SENB) specimens. These specimens were loaded in a three-point bending test to different percentage secant modulus loss (5, 10 and maximum) represented as P% values, hence a P10 value meant 10% secant modulus loss. For each specimen the shape and size were imaged and measured in 3D. They confirmed that microdamage formation started at the onset of non-linearity and that the size of the MDPZ grew quadratically until failure. The shape of the MDPZ was the characteristic 'tear drop' reported for other quasi brittle microcracking materials[79] (Figure 1.10). They confirmed that the size of the MDPZ was meaningfully large, hence non-linear fracture mechanics approaches such as the J-integral are necessary to adequately quantify fracture toughness in cortical bone. Further, they found a second-order polynomial relationship between the volume of the MDPZ and the fracture toughness measured using the J-

integral approach. This hints that changes in the size of the MDPZ will correlate with a change in fracture toughness. Therefore, investigations into how changes to bone's mechanical competency affect the formation of the MDPZ may provide further insight into the bone fracture process.

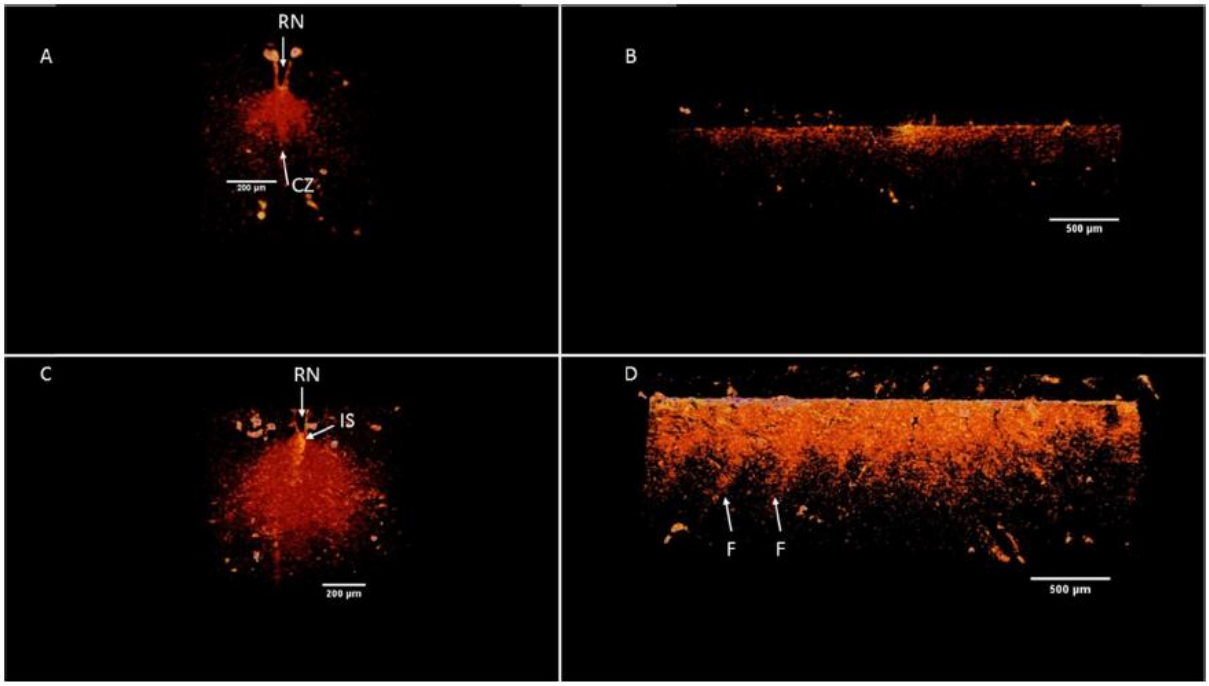

Figure 1.10: Results from imaging the microdamage process zone in *Willett et al, 2017 [78]*. (A) and (C) represent the microdamage process zone stained at 10% secant modulus loss and maximum secant modulus loss (i.e. modulus=0) respectively in the plane of the crack tip. (B) and (D) represent the microdamage formed across the thickness ahead of the crack front for 10% secant modulus loss and maximum secant modulus loss. Reprinted from Willett et al, 2017 *[78]*

1.5 Computational modelling

1.5.1 Description and process

Computational modelling is the study of the behaviour, evolution and characteristics of complex structures, systems or phenomena by means of computer simulations [80]. Computational modelling has grown to become a key component in the fields of engineering and science with major applications in biological, structural, aerospace, mechanical, electromagnetic, fluid dynamics, chemical, control, electrical domains and so forth. The aim of computational models is to mimic the behaviour of systems in the real world using relevant quantitative properties or measures known of the system. To expand on that, computational modelling proceeds in three

main stages: input, engine and output stages [81]. The input stage involves identifying quantifiable features or properties that are vital to the operation of the system or process to the modelled. These are called state variables as they define the current state of the system. The state variables are measured from the system or may be estimated in some cases. The engine stage seeks to replicate the changes or interactions that goes on in the system in the physical world. This is accomplished using mathematical relationships and computational algorithms. In some systems, the mathematical relationships may be simplified by making assumptions. However, these assumptions must not cause the model to deviate from the system's behaviour in the physical world significantly. The most widely used computational technique in the engine stage in modelling is the finite element method (FEM)[81]. The engine stage returns an outcome (outcomes) from the interaction within the system. This is the output stage and the results in the output stage is usually represented graphically for easy interpretation. The output stage is important as, in the development of models, the results generated in this stage are used to validate the model. In the validation process, the model is run for a number of interactions for which the output in the physical world is known. The output from the model is then compared to the corresponding values of the system in the physical world. If there are good agreements, the model is validated and can be relied upon to be used to simulate other similar interactions[81].

1.5.2 Merits over physical experiments

Traditionally, physical systems are studied using physical experiments. Experiments make use of observations and sometimes manipulation of the system especially when investigating the mechanisms, the system employs in its interaction. This is where computational models have an advantage over physical experiments. The methods employed to observe or manipulate the system in experiments may modify the mechanisms/variable being studied/ measured and this is highly undesirable. However, with properly constructed computational models, this concern is alleviated. Computational models have further benefits over physical experiments as listed below:

- The starting configuration of an experimental design is highly repeatable with a computational model whereas they are bound to be differences for physical experiments.
- Variations in specimens especially from biological systems used in physical experiments can be eliminated by using a computational model if the experimental design requires so.

- State variables can be easily manipulated to further investigate and understand the behaviour of the system. Manipulations sometimes can be done quite accurately experimentally but may involve large sample sizes therefore costly and a large amount of time to prepare and test specimens as well as analyse results.
- Computational models allow for easier analysis and interpretation of results as they can be presented graphically and easier exportation of results to other software if necessary.

1.5.3 Applications and limitations

Computational models have a variety of uses in the various fields of engineering and science. A few general applications are listed below:

1. Computational models provide a simple way to investigate whether a hypothesis is true or not
2. Since they can be used to test hypotheses, they can be used to suggest experiments to undertake or changes that may have to be made in the experimental designs
3. They are also used to investigate mechanisms that might be in play in the interactions of a system.
4. They can be used to easily test how changes in the state variables may affect the behaviour of the system.

Though computational models are very useful and carry certain advantages over physical experiments, they have two main limitations. First, they cannot replace physical experimentation. State variables are required for models and these quantifiable features/characteristics are measured from physical experiments. The second is, though they can disprove mechanisms, that they cannot prove mechanisms on their own. Through modelling, a mechanism may be shown to produce an output identical to that observed in the physical world but that does not necessarily mean that mechanism produced the observation in the real world.

Because of these limitations, computational models are regarded as complementary tools and when used together with experimentation and theory can accelerate discoveries as models may fill up the loopholes that experiments and theory cannot.

1.6 Computational modelling of cortical bone fracture

Extensive work has been carried out in computational modelling of the fracture process of cortical bone. The most common computational method used in these studies is the FEM. These models have been used to investigate the contribution of bone's structure and mechanical properties at the different length scales to the fracture process.

At the nano and sub-micro length scale, a 2D finite element (FE) model was used to study the effect the collagen-mineral platelets interface had on the propagation of fracture [82]. This was accomplished by defining a cohesive law (traction-separation law) for the interface. They investigated three types of interface interaction: ionic (strong), hydrogen bond with van der Waal (intermediate) and Van der Waal with viscous shear (weak). They found that the intermediate was more representative of the propagation of fracture in bone. A 3D FE model of a single mineralised collagen fibril was developed by Barkaoui et al. [83]. This model incorporated five collagen molecules interconnected with crosslinks modelled as linear springs and surrounded by hydroxyapatite (HA) crystals. This model was used to investigate the effect of the volume fraction of the HA crystals as well the number of crosslinks present on the failure properties of fibril. There was a considerable increase in both damping capacity and initiation fracture stress of the fibril with increasing number of crosslinks. There was however, no further increase of damping capacity and fracture stress initiation after more than 20 crosslinks were added. A higher volume fraction of HA resulted in a decrease in damping capacity and initiation fracture stress. This suggests the importance of the organic phase to the damping capacity and delayed fracture initiation of the fibril.

Structures at the microscale, predominantly the osteons and their cement lines, have also been modelled and their influence on microcrack propagation investigated. Najafi et al. [84] using an 2D FE model showed that the propagation of microcracks is impeded by the presence of osteons by deviating the microcrack trajectory away from the osteon. This behaviour of deviation of the microcrack growth is consistent with experimental observations [85].

Further, another widely used FEM approach in modelling fracture at the microscale is the cohesive finite element method. In this approach, a traction-separation law is defined and a pre-crack grows when this law is met. For instance, using this method, Mischinski and Ural[86] developed a 2D model of an osteon surrounded by a cement line and the interstitial bone tissue and studied the

interaction of crack growth with these microstructures. They showed that the low strength of the cement lines aided in the crack diversion regardless of the cement line's fracture toughness whereas the fracture properties of the osteon influenced crack growth path irrespective of its elastic modulus. Further, they discovered shorter cracks require cement lines of higher strength and fracture toughness to deflect them into the cement line. Also, they found that the orientation of the crack affected the crack propagation path. This model was extended to include a larger number of osteons [87]. However, this cohesive FE method requires the crack pathway to be pre-defined.

To rectify this limitation in microscale fracture studies, another finite element approach known as the extended finite element method (XFEM) has been used in modelling bone fracture. This method allows a path independent analysis of crack growth and also allows discontinuities to exist in modelling crack propagation [88]. Budyn et al. [89], employing this method, developed a multi-faceted model of the osteonal system and simulated multiple crack growths in the system. Using experiment data from actual human bone specimens, the arrangement of microstructure and their randomised mechanical properties were assigned to the model. This produced a model geometry with mechanical properties that closely mimicked the real-world equivalent. They studied the effect of aging, disease, microstructural arrangement and porosity on the fracture process at the microscale level. Additionally, the Silberschmidt group has used XFEM to analyse crack growth at the micro-scale level [90,91]. They built a 2D model of the Haversian system of the cortical bone and using data from microscopy developed the morphology of the microstructure. The mechanical properties assigned to the microstructural components were those measured using nanoindentation. They also showed how microstructure changes greatly influences crack propagation.

Though these models have been very useful in showing the significance of the microstructure to crack propagation, toughening mechanisms that play a vital role in the fracture process of cortical bone are mostly not explicitly incorporated into them.

1.7 Basic concept of continuum damage mechanics (CDM)

Continuum damage mechanics (CDM) seeks to create mathematical models of damage accumulation in materials [92]. Damage is identified as the loss of continuity in the material. This

can be either the formation of voids or cracks. The accumulation of damage therefore affects the mechanical properties of the material. A key mechanical property measured to show the effect of damage is stiffness [93]. This is because damage accumulation causes softening in materials and this is reflected by a decrease in its initial stiffness. Damage accumulation in CDM is characterised by a damage variable normally represented as "d" or "D". This damage variable, in a simple uniaxial case, is given as [94]:

$$D = \frac{A_D}{A} \tag{1.2}$$

where A_D represents the total area of the material that is damaged and A represents the total cross-sectional area of material. This means when there is no damage, $D = 0$ and $D = 1$ when the material is completely damaged.

Extending this concept to the load-displacement relationship of an elastic material, if there is no damage, the relationship is given as:

$$P = \frac{EA}{L}(\delta) \tag{1.3}$$

where P is the load, E is the elastic modulus of the undamaged material, L is the length of material and δ is the deflection

After damage accumulation, this equation evolves to

$$P = \frac{E(A - A_D)}{L}(\delta) \tag{1.4}$$

Substituting equation (1.2) into equation (1.4), the equation can be written as:

$$P = \frac{EA(1 - D)}{L}(\delta) \tag{1.5}$$

Writing this in terms of stress and strain we have

$$\frac{P}{A} = E(1 - D)\frac{\delta}{L} \tag{1.6}$$

$$\sigma = E(1 - D)\varepsilon \tag{1.7}$$

From the above, a damaged material can be considered as a material with a modulus that has decreased by a factor of $(1 - D)$. Furthermore, it is important to note that σ as represented here is known as the apparent stress. This stress is referred to as apparent because it assumes the initial area of the material remains the same. It doesn't consider that a portion of the material's initial area has been damaged. This formulation rather assigns the damage to a degradation in stiffness.

To represent the degradation of stiffness in a general state of stress form, two concepts are applied. First, the concept of effective stress will be applied [94]. The effective stress is the load acting per unit undamaged area of the material. From the definition, it can be considered as a measure of the true stress induced in the material. Mathematically it is calculated as:

$$\sigma_a = \frac{P}{(A - A_{D)}} \tag{1.8}$$

$$\sigma_a = \frac{\sigma}{(1 - D)} \tag{1.9}$$

where σ_a is the effective stress and σ is the apparent stress.

Representing the above in a general state of stress form gives[95]:

$$\widetilde{\sigma_a} = \tilde{M}\tilde{\sigma} \tag{1.10}$$

where $\widetilde{\sigma_a}$ represents the effective stress tensor, $\tilde{M}$ is the damage effect tensor, and $\tilde{\sigma}$ is the apparent stress tensor.

$\tilde{M}$ is a fourth order linear transformer tensor operator and is a function of the damage variable/operator D.

The simplest form of $\tilde{M}$ is obtained in a uniaxial stress state of a material that undergoes isotropic damage. Such a damage effect tensor is given as

$$\tilde{M} = \frac{1}{1 - D}\tilde{I} \tag{1.11}$$

where $\tilde{I}$ is a fourth order identity matrix.

Further, applying the principle of stress equivalence [96], which states, " the strain associated with a damaged state under the apparent stress is equal to the strain associated with the undamaged state under the effective stress", the effective stress tensor can be expressed as

$$\widetilde{\sigma_a} = \tilde{C}^0 \cdot \tilde{\varepsilon} \tag{1.12}$$

whereas the apparent stress tensor will be expressed as

$$\tilde{\sigma} = \tilde{C} \cdot \tilde{\varepsilon} \tag{1.13}$$

where $\tilde{C}^0$ is the stiffness tensor of the undamaged material, $\tilde{C}$ is the stiffness tensor of the damaged material and $\tilde{\varepsilon}$ is the strain tensor.

Substituting equations (1.12) and (1.13) into equation (1.10) gives:

$$\tilde{C}^0 \cdot \tilde{\varepsilon} = \widetilde{M} \cdot \tilde{C} \cdot \tilde{\varepsilon} \tag{1.14}$$

Therefore, the effective stiffness tensor at any point for an elastic material undergoing damage can be expressed as:

$$\tilde{C} = \widetilde{M}^{-1} \tilde{C}^0 \tag{1.15}$$

This is the product of the inverse of the damage effect tensor and the undamaged stiffness tensor. Using equation (1.15), the evolution of the stiffness of a material undergoing damage can be defined.

1.8 Digital image correlation

Digital image correlation (DIC) is an optical method that uses digital processing of images to calculate displacements and strains on the surface of a specimen experiencing deformation. This method can measure two-dimensional displacement and strain on a planar surface when used with a single camera while with multiple cameras displacement can be measured on three dimensional, non-planar surfaces [97].

DIC operates by comparing images taken before and after deformation. The image taken before deformation is known as the reference image and the image after deformation will be referred to

as the ‘deformed image’. To calculate displacement, a region of interest (ROI) must be defined on the reference image. DIC then divides this ROI into smaller evenly spaced areas called subsets. Each subset is made up of the same number of pixels. The number of pixels that make up a subset is known as the subset size. Each pixel has a grayscale value and these values are summed up for the pixels in each subset. This gives each subset a specific grayscale value. For DIC to work accurately, it requires that each subset gets a unique grayscale value. Therefore, it is necessary for the surface being imaged to have a random grayscale distribution on its surface. Hence in some instances, the specimen’s surface is modified by creating a random speckle pattern to enhance unique grayscale values for the subsets. For every subset in the reference image, a similar sized area as the subset, is sought in the deformed image that will have the best matching grayscale value to it. This is also known as the area with the maximum grayscale correlation coefficient. Mathematically, this may be computed as [97]:

$$C(x, y, x^*, y^*) = \frac{\sum F(x, y) G(x^*, y^*)}{\sqrt{\sum F(x, y)^2 \sum G(x^*, y^*)^2}} \tag{1.16}$$

where $C(x, y, x^*, y^*)$ represents the correlation coefficient

$F(x, y)$ represents the grayscale value of the subset undergoing correlation in the reference image

$G(x^* y^*)$ represents the grayscale value of the different subsets prescribed in the deformed image

(x, y) represents the center position of the subset in the reference image

$(x^* y^*)$ represents the center position of the different subsets prescribed in the deformed image

Other correlation coefficient equations than the one given above may be used [98]. Once, the subset has been matched to an area on the deformed image, the displacement is initially calculated at the center positions of the matched subsets. Mathematically, this can be expressed as [97]:

$$u_x = x^* - x \tag{1.17}$$

$$u_y = y^* - y \tag{1.18}$$

where: u_x represents the displacement in the x-axis

u_y represents the displacement in the y-axis

x and y are the x-component and y-component of the center position of the reference image subset

x^* and y^* are the x-component and y-component of the center position of the deformed image subset

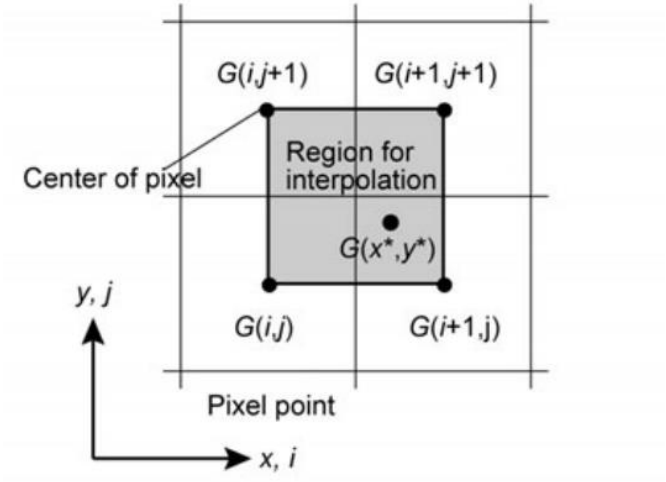

Figure 1.11: Figure showing the neighbouring pixels involved in the interpolation scheme for calculating the displacemnt of point $G(x^*, y^*)$ located in between pixel centers in a deformed image. Reprinted fom Yoneyama., 2015 [97]

This gives a displacement distribution across the ROI at the center points of the subsets in the deformed image. However, the displacements of these center points in the deformed image do not always occur as an integer multiple of the pixel size. This leads to some of these deformed center points occurring in between pixel centers for the deformed image as shown in Figure 1.11. For accurate displacement measurements, DIC must account for this. DIC therefore uses interpolation schemes to deal with these sub-pixel displacements [99]. The interpolation schemes are used to calculate the greyscale values between pixels. The calculation is done using the grayscale values of the neighbouring pixels about that point. The most common interpolation schemes used are the bilinear and bicubic functions. The bilinear uses four neighbouring pixels to interpolate the greyscale value of the point (Figure 1.11) while the bicubic uses sixteen neighbouring pixels to interpolate. It has been shown that the bicubic functions produces a smaller measurement error compared to the bilinear function [99,100]. Since greyscale values can be estimated in between pixels, the correlation coefficient criteria can be used to match the points in between pixels in the deformed image to its corresponding points in the reference image. The displacements can then be calculated using equations (1.17) and (1.18). Note that these displacements will not be a multiple integer of a pixel size but will include sub pixel displacements.

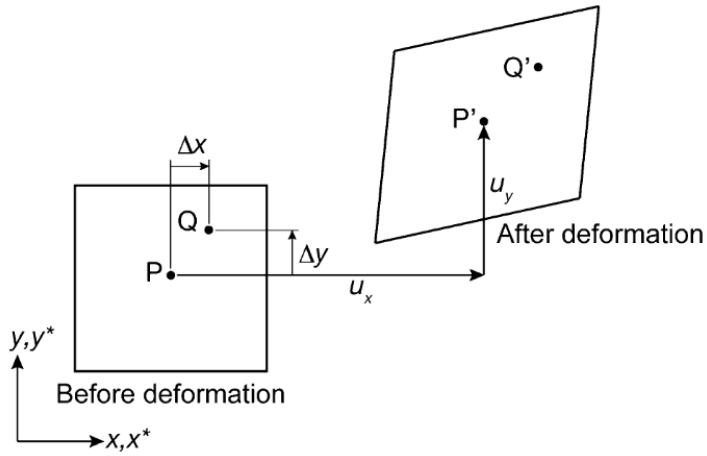

Figure 1.12: Possible deformation of subset in deformed image. Reprinted fom Yoneyama S., 2015 [97]

Furthermore, the subsets may deform as the specimen's surface undergoes deformation as shown in Figure 1.13. This means for accurate measurement of displacement, the deformed subset must be taken into consideration. Assuming the deformation is very small and therefore uniform, a displaced point (x^*, y^*) in the deformed image subset can be related to the corresponding point (x, y) in the reference image subset using shape functions expressed as [101]:

$$x^* = x + u_x + \frac{\partial u_x}{\partial x}\Delta x + \frac{\partial u_x}{\partial y}\Delta y \tag{1.19}$$

$$y^* = y + u_y + \frac{\partial u_y}{\partial x}\Delta x + \frac{\partial u_y}{\partial y}\Delta y \tag{1.20}$$

where: u_x represents the displacement in the x-axis from the center point of the subset

u_y represents the displacement in the y-axis from the center point of the subset

Δx represents the distance of point (x,y) from the center point of the subset in the x-direction

Δy represents the distance of point (x,y) from the center point of the subset in the y-direction

From the earlier discussed correlation criterion and interpolation schemes, calculating u_x and u_y have been shown (equations (1.17) and (1.18)). This leaves six unknowns from equations (1.19) and (1.20) ($\Delta x, \Delta y, \frac{\partial u_x}{\partial x}, \frac{\partial u_x}{\partial y}, \frac{\partial u_y}{\partial x}, \frac{\partial u_y}{\partial y}$).

$\Delta x, \Delta y$ can be easily calculated by finding the distances between point (x, y) and the center point of the subset in the x and y direction respectively.

The other four unknowns, referred to as the displacement gradients, are calculated by revising the correlation coefficient equation (equation (1.16)) to include a **u** vector [102]. This **u** vector is a representation of the displacements and displacement gradient given as [102]:

$$\boldsymbol{u} = \left\{u_x, u_y, \frac{\partial u_x}{\partial x}, \frac{\partial u_x}{\partial y}, \frac{\partial u_y}{\partial x}, \frac{\partial u_y}{\partial y}\right\} \tag{1.21}$$

Therefore, the correlation coefficient becomes [97]:

$$C(x, y, x^*, y^*, u) = \frac{\sum F(x,y) G(x^*, y^*, u)}{\sqrt{\sum F(x,y)^2 \sum G(x^*, y^*, u)^2}} \tag{1.22}$$

The **u** vector is determined by finding a set of displacement and displacement gradients values that gives the maximum correlation coefficient. This means that the partial derivatives of the above equation with respect to each of the displacements and displacement gradients must equal zero.

When this non-linear simultaneous equation is solved, the displacement gradients are obtained. The non-linear simultaneous equation is solved by DIC using an initial guess system and iterative processes such as Newton-Raphson, Levenberg-Marquardt or Gaussian-Newton methods [101–103]. With all these variables determined, the displacement of point (x, y) in the deformed image can be calculated.

It is important to note that due to the interpolation scheme used to estimate the grayscale value at sub-pixel points and the approximate iterative solutions used to solve for the displacement, errors are incurred in the calculations. To minimise these errors, it has been found that the size of the dots that make up the speckle pattern on the surface must occupy about 3 -5 pixels [104]. This is the ideal case and the size of the pixel will depend on the magnification of the image and the resolution of the optical system acquiring the images.

The calculated displacements are then differentiated to compute the strains across the specimen's surface. The equations are given as [104]:

$$\varepsilon_x = \frac{\partial u_x}{\partial x} + \frac{1}{2}\left[\left(\frac{\partial u_x}{\partial x}\right)^2 + \left(\frac{\partial u_y}{\partial x}\right)^2\right] \tag{1.23}$$

$$\varepsilon_y = \frac{\partial u_y}{\partial y} + \frac{1}{2}\left[\left(\frac{\partial u_x}{\partial y}\right)^2 + \left(\frac{\partial u_y}{\partial y}\right)^2\right] \tag{1.24}$$

$$\gamma_{xy} = \frac{1}{2}\left(\frac{\partial u_y}{\partial x} + \frac{\partial u_x}{\partial y}\right) + \frac{1}{2}\left[\left(\frac{\partial u_x}{\partial x}\right)\left(\frac{\partial u_x}{\partial y}\right) + \left(\frac{\partial u_y}{\partial x}\right)\left(\frac{\partial u_y}{\partial y}\right)\right] \tag{1.25}$$

where ε_x, ε_y and γ_{xy} represent the normal strains in the x and y-direction (longitudinal and transverse directions respectively) and shear strain respectively.

However, it is important to note that the errors incurred in calculating displacements in DIC, affect the calculation of strains. When these displacements are differentiated to calculate strains, the errors are doubled leading to greater errors in the strain calculations. DIC algorithms therefore use different methods, such as the least squares or FEM to reduce the errors [103]. These methods will not be discussed in this dissertation but it is worth noting that these methods decrease error in the strain calculations contributing to the accuracy of DIC.

Chapter 2

Objectives and hypothesis

2.1 Objectives

The overall objective of this study was to develop and validate a computational model that simulates the formation of the microdamage process zone (MDPZ) in cortical bone using a continuum damage mechanics (CDM) approach. To the best of our knowledge this will be the first model of its kind for cortical bone.

This study can be further broken down into these four objectives:

1. Identify and model CDM theory applicable for microdamage generation in cortical bone using FE software (ABAQUS);
2. Validate the FE model using experimentally generated full field strain measurements from DIC;
3. Compare the results from the FE model against previous experimental work in which the MDPZ was imaged using microCT; and
4. Compare results from FE model for irradiated bone against previous experimental work in which the MDPZ size was measured for irradiated bone

2.2 Hypothesis

It was hypothesized that a CDM model can replicate the microdamage formation observed experimentally, reflecting a similar MDPZ size and shape.

Chapter 3

Methods

To model the microdamage process zone (MDPZ), a continuum damage mechanics approach was implemented in the commercial finite element software ABAQUS 2017 (Abaqus Inc., USA). ABAQUS allows the bone specimen to be modelled by dividing it into a finite number of smaller portions called elements (i.e. the finite element method). These elements are assigned the mechanical properties and behaviours of cortical bone required to simulate the formation of the MDPZ. A three-point single edge notched bending (SENB) test of bovine cortical bone specimens was simulated and validated with experimental results from Willett et al.[78] and new experiments. A SENB specimen contains a sharpened noch of known dimensions machined into the side of the specimen that experiences tension during a bending test. The notch was directed such that the resulting crack grew in the circumferential direction on the transverse plane of the diaphysis. The modelling was done in 2D because CDM has only been formulated in 2D for ABAQUS.

3.1 Theory for modelling

A typical load versus load-line deflection curve for a cortical bone specimen subjected to bending can be divided into two regions: linear and non-linear (Figure 3.1). The non-linear region represents the softening of the cortical bone specimen with increasing deflection. The softening is the result of the formation of the microdamage process zone (MDPZ)[66]. The onset of non-linearity represents the initiation of microdamage formation in the cortical bone specimen. The continual formation of microdamage leads to continual degradation in the stiffness of the region of microdamage formation leading to the overall reduction in the specimen's secant stiffness until complete specimen rupture.

Therefore, to model this material behaviour of microdamage formation, two important parameters must be defined:

1. The load (stress) at which microdamage formation initiates, and
2. The rate of stiffness degradation with continual formation of the MDPZ until fracture.

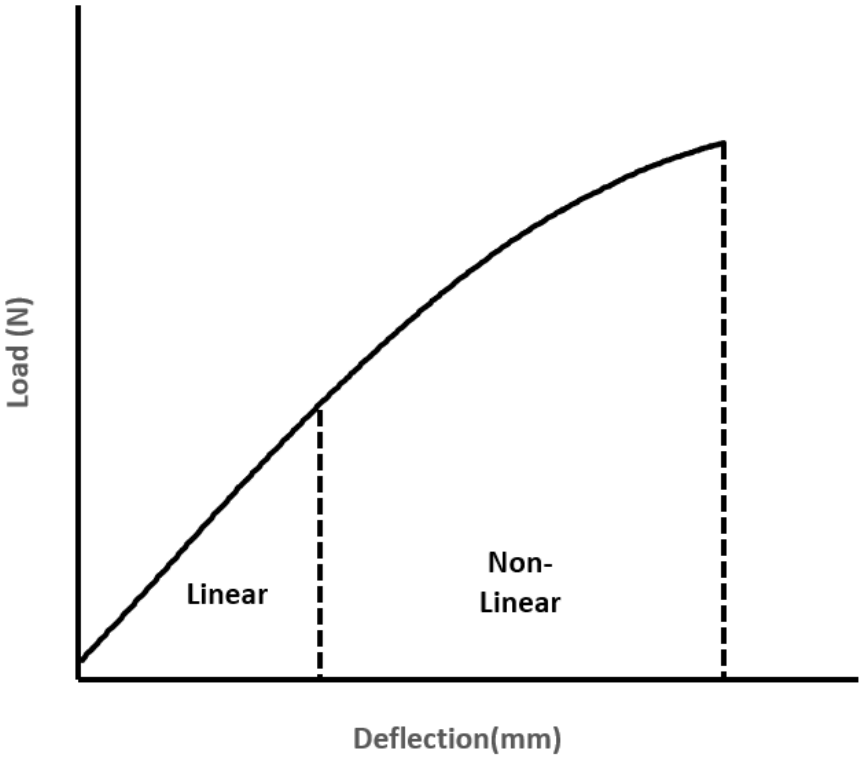

Figure 3.1: A typical load versus load-line deflection curve for bovine cortical bone

3.1.1 Initiation of microdamage formation

The initiation of microdamage signifies the start of stiffness degradation in the specimen. Up to this point, the specimen behaves as a linearly elastic material. To define this point of microdamage formation initiation, the Hashin failure criteria was used [105]. The Hashin criteria is a frequently utilised failure criteria for fiber reinforced composites. Bone can be considered a fiber reinforced composite because of the orientation of its predominant microscale structure, the osteon, and its established approximate transverse isotropy [106]. At the microstructural level, the osteons align along the axis of the long bone serving as the reinforcing fibers, while the interstitial bone tissue around them serve as the matrix [106]. Further, the Hashin criteria defines failure separately for tension and compression in the both the longitudinal (fiber) and transverse (matrix) directions. Cortical bone exhibits anisotropic material behaviour as well as asymmetric strength. Therefore, the Hashin criteria becomes a suitable failure criterion to account for these. ABAQUS 2017 has an in-built function that allows the definition of failure by the Hashin failure criteria [107]. The Hashin criteria is improved in ABAQUS by incorporating a modification based on work done by Davila and Camacho [108]. In their work they formulated changes to the failure criteria for both longitudinal and transverse compression failure modes to allow more accurate predictions of

failure in these modes [108]. The general forms of the criteria in the different directions are given as [107]:

$$F_X^t = \left(\frac{\sigma_{11}}{X^T}\right)^2 + \alpha\left(\frac{\tau_{12}}{X^S}\right)^2 \qquad \sigma_{11} \geq 0 \qquad (3.1)$$

$$F_X^c = \left(\frac{\sigma_{11}}{X^c}\right)^2 \qquad \sigma_{11} \geq 0 \qquad (3.2)$$

$$F_Y^t = \left(\frac{\sigma_{22}}{Y^T}\right)^2 + \left(\frac{\tau_{12}}{X^S}\right)^2 \qquad \sigma_{22} \geq 0 \qquad (3.3)$$

$$F_Y^c = \left(\frac{\sigma_{11}}{2Y^S}\right)^2 + \left[\left(\frac{Y^C}{2Y^S}\right)^2 - 1\right]\frac{\sigma_{22}}{Y^C} + \left(\frac{\tau_{12}}{X^S}\right)^2 \qquad \sigma_{22} \geq 0 \qquad (3.4)$$

where $\sigma_{11}, \sigma_{22}, \tau_{12}$ are the effective longitudinal, transverse and shear stresses respectively and X^T, X^c, X^S are the longitudinal tensile, compressive and shear strengths respectively, and Y^T, Y^C, Y^S are the transverse tensile, compressive and shear strengths respectively, α is a coefficient that determines the contribution of the shear stress to the longitudinal tensile initiation criterion (α=0 for this model). $F_X^{t,c}$ represents the value of the failure variable in the longitudinal direction when in tension or compression respectively and $F_Y^{t,c}$, the value of the failure variable in the transverse direction when in tension or compression respectively.

When any of the failure mode variables ($F_{X,Y}^{t,c}$) reaches a value of 1, the failure criterion for that mode is met. This means the start of microdamage formation begins when the failure variable reaches 1. Hence the initiation point of the microdamage formation for the model is achieved using the Hashin failure criteria function in ABAQUS. ABAQUS provides an output variable, HSNFTCRT, which is used to define the microdamage process zone in the model. This output represents the Hashin failure criterion in the longitudinal tension direction. Any element with a HSNFTCRT value equal to 1 or above signifies that microdamage formation has initiated in that element.

3.1.2 Evolution of stiffness degradation

After microdamage formation has been initiated, the stiffness of the bone material will begin to degrade. It is important that the rate at which the stiffness degrades for the model adequately mimics the rate at which the stiffness degrades in the physical world. To evaluate this evolution of stiffness degradation, ABAQUS allows a bi-linear continuum damage mechanics (CDM) law to

be defined (Figure 3.2). This bi-linear CDM law is similar and consistent with the cohesive zone modelling (CZM) law mentioned in Section 1.3.4. The difference is that while the CZM law considers only the opening of the crack tip (crack growth) in relation to the stress-strain field distribution around it, the bi-linear CDM law considers degrading the stiffness of the material around the crack tip in relation to the stress-strain field distribution. The bi-linear CDM law uses the concept of continuum damage mechanics to degrade stiffness by establishing a relationship between applied stress, displacement (deformation of an element) and the damage variable.

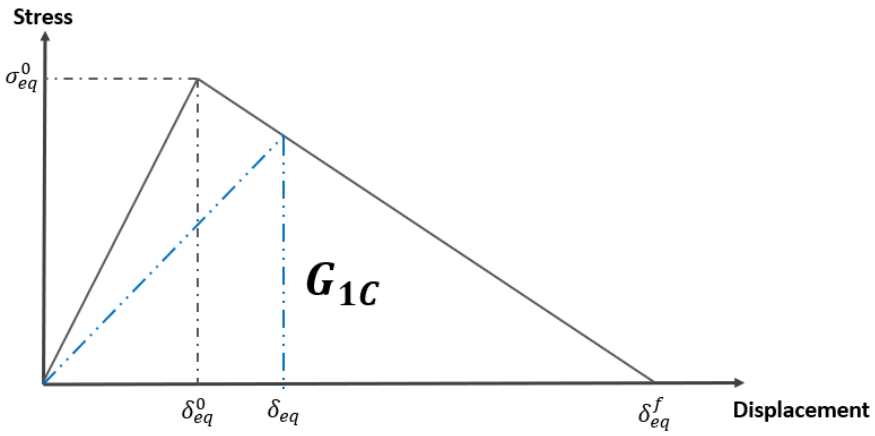

Figure 3.2: Bi-linear law defining evolution of stiffness degradation after Hashin failure initiation

The damage variable was introduced in Section 1.6. The total area under the bi-linear law represents the fracture energy (G_{1C}) (Figure 3.2). The fracture energy is the energy that will be dissipated to completely damage (fracture) the material. The first part of the law, up to the maximum stress (σ_{eq}^{0}), is characterised by the constant initial stiffness of the undamaged bone material in that particular direction (longitudinal or transverse). The Hashin failure criterion for a particular failure mode (longitudinal tension or compression, transverse tension or compression) is met at this maximum stress value. For pure mode-I loading, where no shear stresses are induced around the area of crack propagation, the maximum stress in a particular failure mode is equivalent to the proportional limit stress in that failure mode.

Once this maximum stress is reached, microdamage formation begins. Accompanying this is a decrease in stiffness of the bone material which is controlled by the damage variable. The damage variable for any particular failure mode is given as [107] :

$$d_{fm} = \frac{\delta_{eq}^{f}(\delta_{eq} - \delta_{eq}^{0})}{\delta_{eq}(\delta_{eq}^{f} - \delta_{eq}^{0})} \tag{3.5}$$

where d_{fm} is the damage variable, δ_{eq}^{0} is the displacement at initiation of stiffness degradation, δ_{eq}^{f} is the displacement at complete damage (fracture) and δ_{eq} is the current displacement of the material.

The value of δ_{eq}^{0} is dependent on the initial stiffness and strength defined for that mode while δ_{eq}^{f} is determined by the failure strain of cortical bone in this model. Note that the bi-linear law provided by ABAQUS is defined using displacements. To convert these to their strain equivalence, ABAQUS uses a variable known as the characteristic length [107]. This characteristic length is dependent on the type and size of mesh used in the model and is analogous to the original length parameter used in calculating engineering strain. This characteristic length is particularly important as fracture in cortical bone has been found to be strain controlled [41]. This means, it is more accurate to use the strain at fracture for determining the point of complete damage. The characteristic length provides a means of establishing a relationship between the strain at fracture (ε_{eq}^{f}) and its equivalent displacement represented as δ_{eq}^{f} in the bi-linear law. This is given as:

$$\varepsilon_{eq}^{f} = \frac{\delta_{eq}^{f}}{l_c} \tag{3.6}$$

Considering the bi-linear law in Figure 3.2, the total area under the curve can be calculated based on the equation for calculating the area of a triangle. Since this area is equal to the fracture energy, this becomes:

$$G_{1C} = \frac{1}{2} \cdot \sigma_{eq}^{0} \cdot \delta_{eq}^{f} \tag{3.7}$$

Substituting equation (3.6) into (3.7) gives

$$G_{1C} = \frac{1}{2} \cdot \sigma_{eq}^{0} \cdot l_c \cdot \varepsilon_{eq}^{f} \tag{3.8}$$

σ_{eq}^{0} and ε_{eq}^{f} can be determined experimentally and l_c can be calculated if the type and size of the mesh is known. With all these variables determined, G_{1C} can be calculated and the bi-linear law can be established to control the evolution of the damage variable. The bi-linear law and therefore

the damage variable are defined for all failure modes in the Hashin failure criteria (longitudinal (fiber) tension and compression and transverse (matrix) tension and compression).

With these damage variables determined, the corresponding stiffness tensor of the bone material at any point can be obtained by:

$$C_d = \frac{1}{D}\begin{bmatrix} (1-d_1)E_1 & (1-d_1)(1-d_2)v_{21}E_1 & 0 \\ (1-d_1)(1-d_2)v_{12}E_2 & (1-d_2)E_2 & 0 \\ 0 & 0 & D(1-d_{12})G_{12} \end{bmatrix} \quad (3.9)$$

where $D = 1 - (1-d_1)(1-d_2)v_{21}v_{21}$

$$d_1 = \begin{cases} \text{damage variable in fiber tension} & \sigma_{11} \geq 0 \\ \text{damage variable in fiber compression} & \sigma_{11} < 0 \end{cases}$$

$$d_2 = \begin{cases} \text{damage variable in matrix tension} & \sigma_{22} \geq 0 \\ \text{damage variable in matrix compression} & \sigma_{22} < 0 \end{cases}$$

$$d_{12} = 1 - (1-d_1)(1-d_2)$$

E_1, E_2 *and* G_{12} are the undamaged (initial) longitudinal, transverse and shear Young moduli

v_{12}, v_{21} are the undamaged Poisson's ratios.

With the damaging stiffness matrix defined, the stress response of the bone material can be computed using:

$$\{\sigma\} = [C_d]\{\varepsilon\} \quad (3.10)$$

where $\{\sigma\}$ is the effective stress tensor

$[C_d]$ is the damaging stiffness tensor

$\{\varepsilon\}$ is the strain tensor

3.1.3 Model analysis

As depicted in Figure 3.1, the solution of the model involved a considerable amount of non-linearity. This means the stress-strain relationship involved a system of non-linear equations. To solve this system of non-linear equations, ABAQUS employs the Newton-Raphson technique. Foremost, this technique divides the whole analysis into smaller portions, known as time steps. For each time step, the stiffness matrix of the model is solved. This is achieved by initially guessing

the stiffness matrix solution to the system of non-linear equations and iteratively re-solving the systems of equations until the solution is within a tolerance limit relative to the solution of the equivalent system of linear equations. This tolerance limit is defined by ABAQUS.

Furthermore, because this analysis involved considerable degradation of the stiffness matrix, the model suffered convergence difficulties. In other words, the stiffness matrix becomes negative at a point. To rectify this difficulty, ABAQUS allows the introduction of a viscous regularisation scheme. It works by slowing down the degradation of the stiffness matrix and allowing a positive stiffness matrix to exist for each time step. This viscous regularisation is based on the regularisation model of Duvant and Lions [109]. The viscous regularisation introduces a viscous damage variable in place of the damage variable and this is computed as [107]:

$$\frac{d(d_v)}{dt} = \frac{1}{\eta}(d - d_v) \tag{3.11}$$

where d_v is the viscous damage variable, $\frac{d(d_v)}{dt}$ is the first derivative of the viscous damage variable with respect to step time, d is the inviscid damage variable, and η is a viscosity parameter that represents the characteristic stress relaxation time of the viscous system/material. How this parameter is determined will be discussed later in this chapter.

Solving the differential equation gives

$$d_v = d(1 - e^{\frac{-t}{\eta}}) \tag{3.12}$$

where t is the time step.

When $\frac{t}{\eta} \to \infty$, equation (3.12) reduces to $d_v = d$. This means the effect of the viscous regularisation scheme on the results will be negligible. However, for a larger value of η in comparison to *t*, viscosity effects are introduced into the analysis of the model by slowing down the rate of increase in damage and therefore the rate of stiffness degradation. This function can be utilised as a means of incorporating rate-dependent behaviour in the model [88]. In modelling the MDPZ in this case, this function was exploited to add viscoelastic effects to the model.

Altogether, the stiffness matrix of the model was generally computed from one time step to the next as [107]:

$$\frac{\partial \sigma}{\partial \varepsilon} = C_d + \varepsilon : \sum \frac{\partial C}{\partial d_v} \frac{\partial d_v}{\partial d} \frac{\partial d}{\partial \varepsilon} \tag{3.13}$$

where C_d is the damaged elasticity matrix from the previous step time and the second term represents the degradation of elasticity matrix as a result of increased damage in the failure modes of interest.

If there is no damage generation in a time step, then the damaged elasticity matrix remains the same and the model will behave linearly elastic over that time step.

3.2 Modelling in Abaqus

3.2.1 Geometry, boundary conditions and meshing

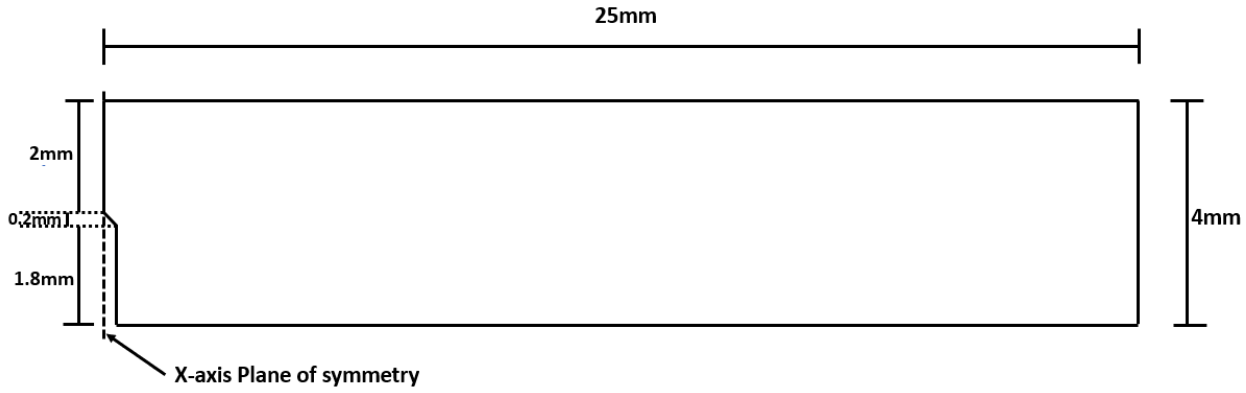

Figure 3.3: Details of the geometry of the model and its plane of symmetry

The specimen was modelled as a 2D solid deformable body. Transverse isotropy was assumed for the model. This is a reasonable assumption as the mechanical properties of cortical bone have been found to be comparable in the radial and circumferential directions but significantly different in the longitudinal directions [110,111]. The geometry of the SENB bovine cortical bone specimen in Willett et al. [78] was closely replicated as represented in Figure 3.3. A plane of symmetry was applied in the X-axis along the center line of the notch. Therefore, only half of the specimen was modelled and an X-symmetry function applied to it in ABAQUS (Figure 3.3). To replicate the testing configurations, a roller boundary condition was applied at the point at the base of specimen 5mm away from the edge of the specimen (Figure 3.4). A displacement-controlled load was applied at the top of the specimen along the center line of the notch ((Figure 3.4). This is representative of the loading carried out in a real SENB test.

A rectangular region of interest (ROI) was defined around the crack tip. This ROI was the perceived region of the model that will undergo the formation of the MDPZ. The ROI was 2mm in height and 1.5mm in width. The dimensions were chosen based on known geometry of the MDPZ from experimental results [78]. This ROI had a finer mesh compared to the rest of the model to accurately capture the formation of the MDPZ (Figure 3.5). The mesh size for the ROI was 10µm and the rest of the model was mostly meshed with 500µm sized elements.

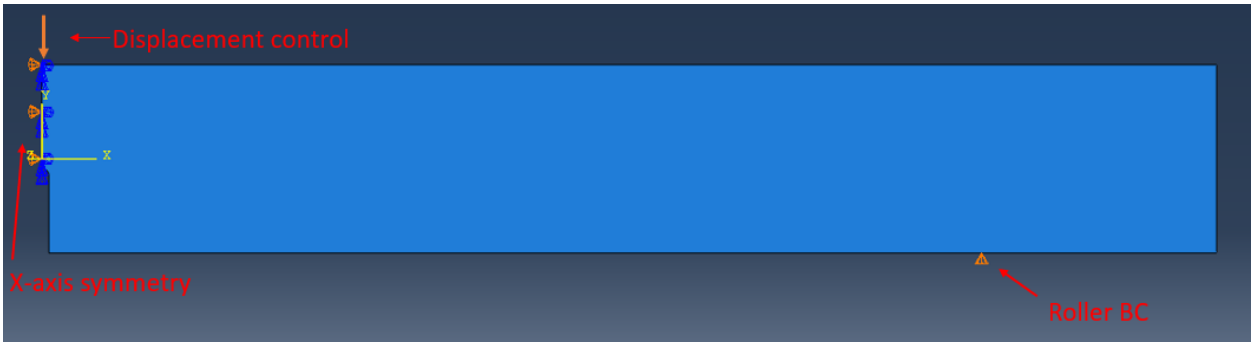

Figure 3.4: The boundary conditions defined for the model

The ROI was meshed with square quadratic plane stress elements while the rest of the model was meshed square linear plane stress elements. The variation in mesh size and elements was performed to reduce computational cost. The region expected to form the microdamage was given a higher degree of mesh and element type to accurately capture the mechanism of microdamage formation while the rest of the model did not require the same level of detail. A stress field distribution of the model is presented in the results section to confirm this mesh pattern as an accurate approach.

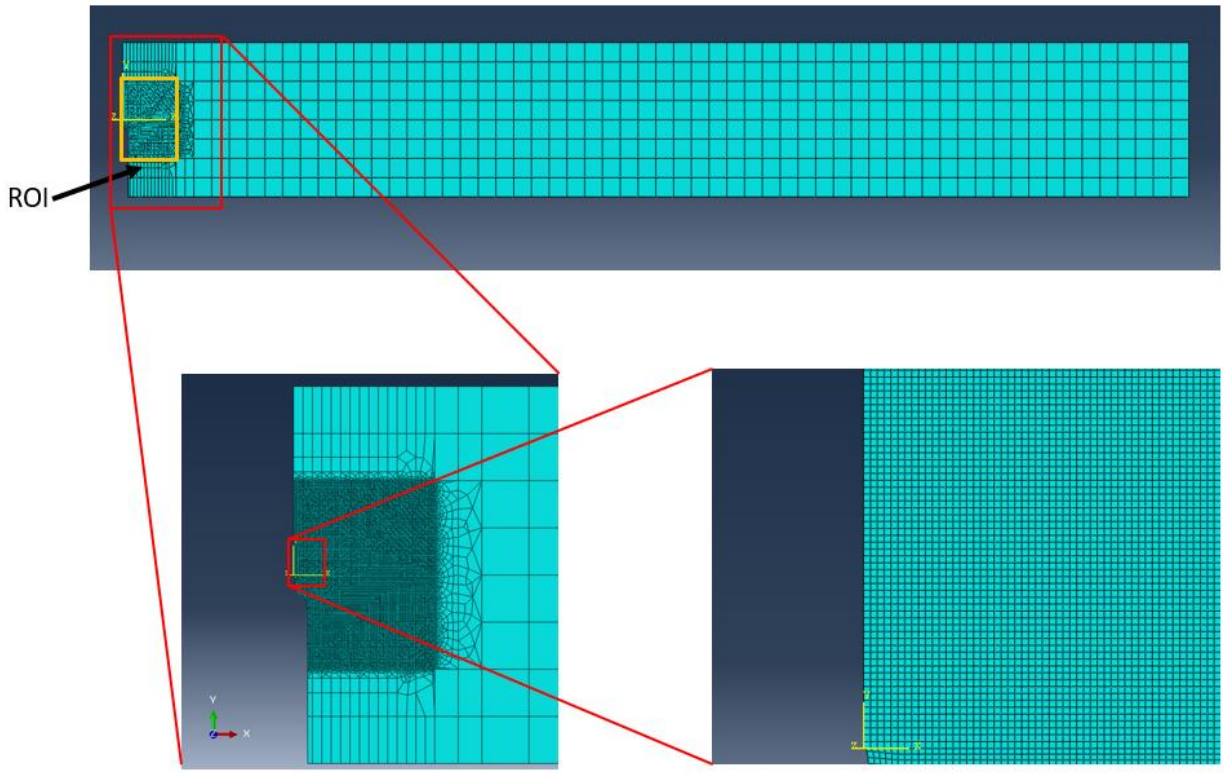

Figure 3.5: Region of interest defined and variability of meshing of the model

3.2.2 Defining mechanical properties

A number of mechanical properties of the bovine cortical bone was necessary to run an analysis in the model. The mechanical properties required were those needed to define the bi-linear CDM law (Figure 3.2). First, the elastic moduli, as well as the Poisson ratio, for the longitudinal and transverse directions were defined. To define these values, studies measuring these properties were sought from the literature. However, values reported in literature showed a considerable level of variability even within the same study. This is understandable as bone is a heterogenous biological material and its mechanical properties change based on its constituents and porosity [112,113]. To determine a single value for each elastic modulus and Poisson ratio, a trial and error optimisation method was used. Starting with the average values given in literature, the values were adjusted until the linear portion of load versus load-line deflection curve generated from the model fit the curve produced in experimental testing. However, this value had to be within the reported mean ± standard deviation for these mechanical properties reported in the literature. The average values utilised were adopted from Reilly and Burstein [110] and Li et al. [111].

Further, the strength of the bovine cortical bone material in the different failure modes had to be defined. The strength as stated here, refers to the elastic/proportional limit on the stress-strain curve for that failure mode and not necessarily the ultimate strength. The strength was defined in the longitudinal tension, compression and shear directions as well as transverse tension, compression and shear directions. This is a requirement in ABAQUS. The strength values signified the stress at which microdamage formation began for any particular failure mode (this is the same as σ_{eq}^{0} as defined in the CDM bi-linear law). Similar to the elastic moduli and Poisson ratios, the strength values can vary significantly from one bovine cortical bone to another. To ascertain a specific value to use for a particular specimen, a similar trial and error optimisation approach was taken such that the load-deflection curves from the experiment and model matched closely. In addition, using stress-strain plots from Reilly and Burstein [110] and Li et al. [111], estimated ranges of the elastic/proportional limit strains in the compressive and tensile failure modes were determined (

Table 3.1). Using these values and Equation (3.14), estimated strength values can be obtained and the trial and error optimisation approach can be used to further refine the load versus deflection curve to fit closely to the one generated experimentally.

$$\sigma_0 = \varepsilon_0 E \tag{3.14}$$

where σ_0 is the strength, ε_0 is the elastic limit strain and E is the elastic moduli selected using the trial and error optimisation approach. All these are specific to the failure mode of interest.

The longitudinal and transverse shear strengths were however kept constant for the different analyses. These values used were adopted from Turner et al. [114].

Finally, the fracture energies for longitudinal tension and compression as well as transverse tension and compression were defined. To define these, Equation (3.8) from Section 3.1.2. was re-visited. The failure strains for the various failure modes of interest were adopted from Reilly and Burstein [110] (

Table 3.1). The mesh size of our ROI as stated earlier was 10µm and was meshed with quadratic elements. The characteristic length of a quadratic element is half its size [88]. Hence the characteristic length was 5µm for the elements in the ROI. σ_{eq}^{0} is equivalent to the Hashin failure

strength in the direction for which the fracture energy is being calculated. With all these properties defined, the fracture energies were calculated.

Table 3.1: The elastic limit and ultimate(failure) strains for bovine cortical bone in the different failure modes (Adapted from [110] and [111])

Failure mode	**Elastic limit strain range**	**Ultimate strain**
Longitudinal tension	0.0045±0.00055	0.02
Longitudinal compression	0.01±0.00045	0.016
Transverse tension	0.0044±0.00045	0.007
Transverse compression	0.009±0.00105	0.042

The strengths and fracture energies were only defined for the elements in the ROI. The stresses in the elements outside the ROI were not expected to reach the Hashin failure strengths of the different failure modes. This was verified in the model by plotting the stress field distribution at failure (see Results section). This meant there was no need for the strengths and fracture energies to be defined as only the linear portion of the CDM bi-linear law will be required in these elements. Similar to the mesh size variation, this was done to reduce computation time and allow easier convergence of the model to the final solution.

Tables showing the various mechanical properties values used in the different analyses (for verification and validation) carried out with the model are presented in the Appendix.

3.2.3 Defining the viscosity parameter(η) for the viscous regularisation scheme

Fondrk et al. [115] proposed a damage model for the non-linear behaviour of cortical bone under tension. In their model, they suggested three different mechanisms to account for the non-linear behaviour of bone: damage accumulation, viscoelasticity and plasticity. However, in the initial stages of developing their damage model, they defined a damage model without plasticity. This, they called a 'perfectly damaging model'. Normally, after loading past the "yield point" of cortical bone and then unloading, there exists a level of irrecoverable strain due to irreversible effects of plasticity (Figure 3.6). However, in the 'perfectly damaging model', due to the lack of plasticity, there is no irrecoverable strain for this model. Despite this shortcoming, the "perfectly damaging model" is a good approximation of the non-linear behaviour of cortical bone during the loading

stage as it matches closely with the loading portion of an experimental stress strain curve, only deviating for the unloading regime of the curve (Figure 3.6).

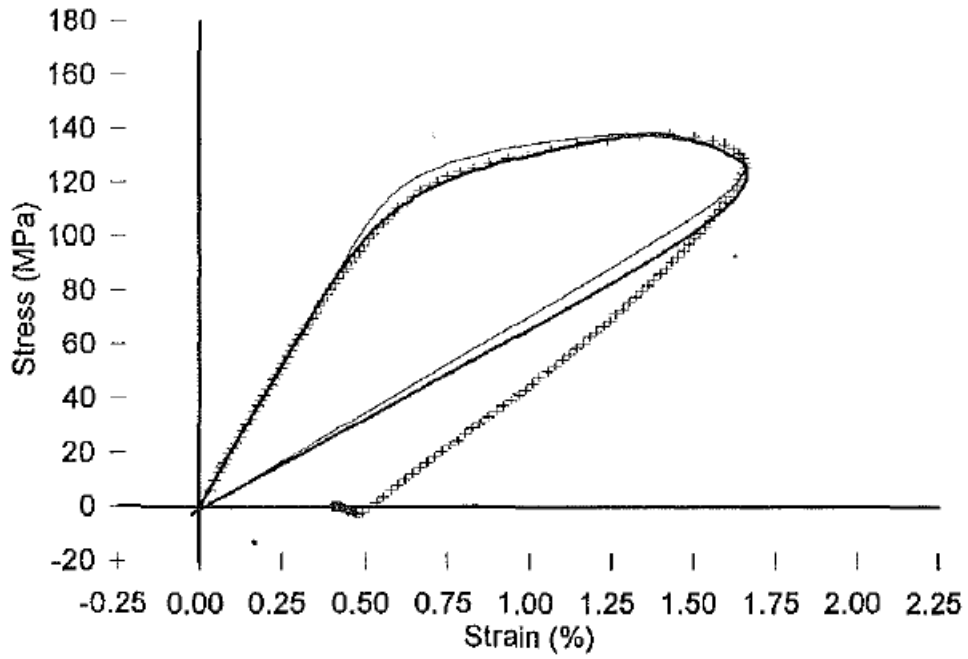

Figure 3.6: Perfectly damage model simulation from Fondrk et al.[115] *compared to an experimental stress-strain curve for bovine cortical bone. The crosses represent the experimental results whiles the solid line the model simulated stress strain curve.: Perfectly damage model simulation from Fondrk et al.*[115] *compared to an experimental stress-strain curve for bovine cortical bone. The crosses represent the experimental results whiles the solid line the model simulated stress strain curve.*

The formulation of the CDM model in ABAQUS in this study, makes it synonymous to this perfectly damaging model in Fondrk et al. [115]. The damage variable represents the damage accumulation mechanism while the enhanced viscous regularisation scheme introduces the viscoelastic mechanism. ABAQUS does not allow plasticity to be defined when using the Hashin failure criteria function, hence plasticity is not defined for the CDM model.

Further, Fondrk's perfectly damaging model is analogous to a standard linear solid (SLS) model for a viscoelastic solid (See Figure 3.7) when damage and plasticity do not occur. Since the viscosity parameter (η) represents the relaxation time of the perfectly damaging model, it is also analogous to the relaxation time for the SLS model. This viscosity parameter is defined for the perfectly damaging model when no damage has occurred.

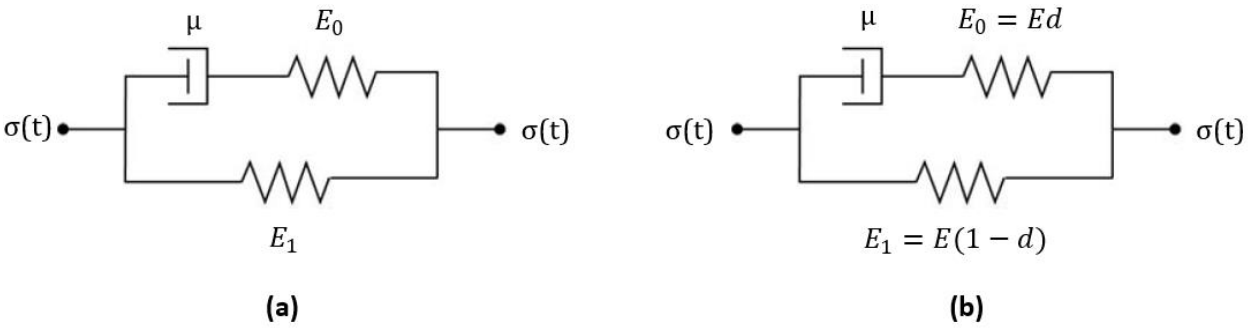

Figure 3.7: (a) representation of the standard linear solid (SLS) model for a viscoelastic element, and (b) representation of the perfectly damaging model proposed by Fondrk et al. d represents the damage variable.

In the CDM model, a controlled displacement was applied, hence a constant strain condition (stress relaxation response) will be considered. For a constant strain condition, the relaxation time for the stress relaxation response of a SLS is given as:

$$\tau = \frac{\mu}{E_0}$$

where μ is the viscosity co-efficient of the material/system.

Therefore, for the perfectly damaging model, the viscosity parameter (η) is also given as:

$$\eta = \frac{\mu}{E_0}$$

For bovine cortical bone, Fondrk et al.[115, 116] found E_1, which is known as the relaxed modulus to be $0.88 \pm 0.03E^0$ where E^0 is the instantaneous (initial) elastic modulus.

From the SLS model formulation,

$$E^0 = E_0 + E_1$$

Therefore, $E_0 = 0.12 \pm 0.03E^0$ for cortical bone, once relaxed to equilibrium. Also, the viscosity co-efficient (μ) was reported to be 103.5 MPa.s [115]. Using these values, the viscosity parameter range for each fracture direction can be calculated. In a longitudinally directed fracture, transverse stresses are applied and hence the transverse elastic modulus will be used. Assuming an average transverse modulus of 10.1 GPa, which is consistent with the value used in the CDM model simulations, the longitudinally directed viscosity parameter will be between 0.07-0.11s. In transversely directed fracture, longitudinal stresses are applied and hence a longitudinal elastic

modulus of 18.7 GPa was used, again consistent with the value used in the CDM model. This gives rise to a transversely directed viscosity parameter between 0.04 to 0.06s.

For each direction, a single value was picked from each respective range for a specific specimen CDM simulation such that the experimental load versus deflection curve was matched by the CDM model equivalent. The viscosity parameter values for different simulations are reported in the Appendix along with the other mechanical properties.

3.2.4 Verification of bi-linear CDM law

An important step in modelling is the verification step. In this step, simple loading conditions are imposed on the model for which the expected outcome is known. For a transversely directed crack specimen in a pure Mode-I bending test, the most critical mode of failure will be in the longitudinal tensile mode. To verify the CDM model obeyed the bi-linear law as established in Section 3.1.2., a simple tensile test in the longitudinal direction was performed with the mechanical properties defined. This test was conducted because it considers the most critical failure mode: longitudinal tension. Further, it is the failure mode of interest for achieving the objective of the model, which is to simulate microdamage formation ahead of the crack tip in the SENB specimen. The region ahead of the crack tip experiences tension and since the crack is growing transversely, the material fractures across the longitudinal direction.

To perform the test, a simple plate was modelled in 2D assuming plane stress of dimensions 0.01×0.1mm (Figure 3.8). The block was fixed at one end and a displacement control defined at the other end to simulate a simple tensile test in the longitudinal direction (Figure 3.8). The plate was meshed with square quadratic elements of size 10μm. Using Equation (3.8) , the fracture energy was calculated. Two different types of this test were run with the stress-strain curve of the model then plotted for each type. First, a test was run without the implementation of the viscous regularisation scheme. It was expected that the stress strain curve of this type will mimic the CDM bi-linear law, verifying that the model obeys the law. Secondly, the same test was run but with the viscous regularisation scheme implemented in this instance. This was to show the effect of this rate-dependent behaviour on the model. For additional verification, this procedure was repeated for the transverse tension failure mode. The mechanical properties used for these verification tests are reported in the Appendix.

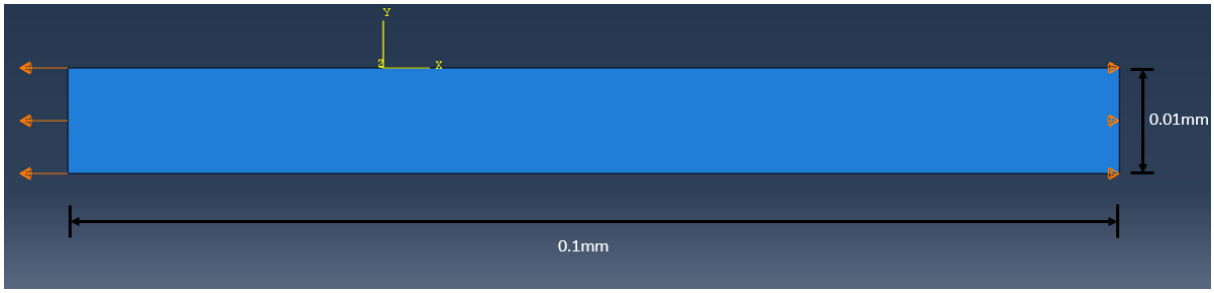

Figure 3.8: Simple plate model for verification of CDM bi-linear theory

3.2.5 Running the CDM model

After defining the boundary conditions and mechanical properties for the CDM model as well as verifying the bi-linear law, the model was run in ABAQUS/Standard as an implicit analysis. This mimicked the quasi-static loading that occurred in the physical SENB experiments [78]. A time step of 0.001 was used with 1000 sub-steps required to complete the analysis. The reaction force and displacement of the node on which the displacement control load was assigned, (Figure 3.4) was tracked throughout the analysis. Using these two parameters, the load versus load-line deflection curve was plotted for the CDM model.

3.2.6 Mesh sensitivity test

A mesh sensitivity test was carried out to study the mesh independency of the model. This was performed by meshing the ROI with quadratic square elements of different sizes (0.0075, 0.01, 0.015, 0.03, 0.05 mm) and generating the load versus deflection curves for each mesh size model. It was expected that these load versus deflection curves matched to signify the mesh independency of the model. The mechanical properties were kept constant for all mesh sizes except the fracture energies. The fracture energies have been shown to be dependent on the characteristic length of the elements which is a function of mesh size (Equation (3.8)). The fracture energies were therefore calculated to match the mesh size being used in the various sensitivity test. The various fracture energies used for the different mesh sizes are reported in the Appendix.

3.3 Experimental validation using DIC

The next step after building the model was to validate it using experimental data. To do this, the loading configuration (3-point SENB test) modelled was carried out on two bovine femoral cortical bone specimens. Using a microscope equipped with a camera, images were taken during the test

and digital image correlation (DIC) was used to measure the full field strain distribution ahead of the crack tip. Using the strain field measurement from DIC, the area of microdamage formation can be determined and compared to that generated by the model. The SENB specimens were prepared by combining testing guidelines from both ASTM Standard E1820 [117] and D6068 [118]. For instance, the sharpening of the starter notch as required for the bending test was done by using a razor blade as stipulated in D6068 (see Section 3.3.2). However, a modification was made to the testing span stipulated in both standards. The testing span is the distance between the roller supports for the bending test (Figure 3.9). Both standards require the testing span to be four times the height of the specimen. However, to prevent high shear stresses from being induced around the crack tip due to the composite and anisotropic behaviour of cortical bone, a testing span of ten times the height was used. This was consistent with previous work by our group [60,78]. From the above, specimens of dimensions 4×4×50mm were prepared with a sharpened starter crack of 2mm long. This meant a testing span of 40mm was used (Figure 3.9). These dimensions were also consistent with the dimensions used in the model.

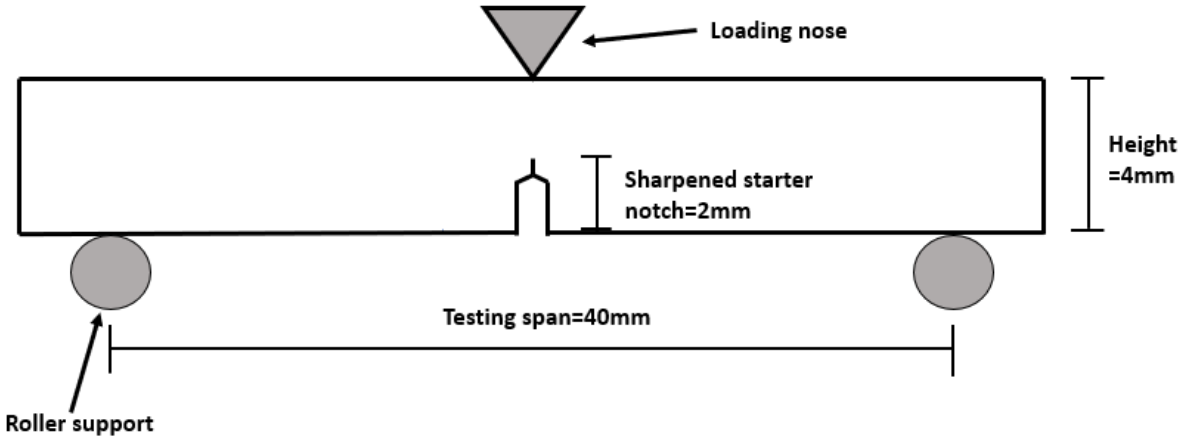

Figure 3.9: Testing configuration and dimensions of important parameters in accordance with ASTM E1820 and D6068 testing standards

3.3.1 Rough and fine cutting of SENB specimen

The femur of a young cow was sourced from a local abattoir and kept frozen at -20°C. Cutting of the femur to produce the SENB specimens was carried out at room temperature. Prior to cutting, the femur was thawed and rid of any soft tissue using a scalpel and a sharp razor blade. The femur was then re-frozen and, in that state, the epiphysis at both ends of the femur was cut off using a

14” Craftex CX104 wood cutting band saw (Busy Bee tools, Concord, ON, Canada). This left the diaphysis of the femur for further cutting. The diaphysis was approximately 100mm in length. Using the band saw again, the diaphysis was split into two halves along the long axis of the bone. The split halves were allowed to thaw and the bone marrow removed. This produced two hollow semi cylindrical specimens of bovine femoral cortical bone. The diaphysis was split in two to allow for ease of cutting in the subsequent steps.

A vertical mini computer numerical control (CNC) mill (model 5410, Sherline products, Vista, California, US) was then used to cut a rectangular block out of one half of the diaphysis. This cutting was done dry as the mill works by dry cutting. The half-diaphysis was securely mounted on the table of the mini-CNC mill using step block hold-down sets (Sherline products, Vista, California, US). A piece of rough sandpaper was placed under the half diaphysis to prevent slipping during cutting by the mill. Using 1/8” end mill cutter, a rectangular block of about 70mm in length and 15mm in width was cut out of the half-diaphysis. The rectangular block was cut out from the middle portion of the diaphysis. This ensured that the straightest and thickest portion was cut out. The cutting of the rectangular block was done by cutting the trace of the rectangular block dimensions (15×70mm) at a 1mm depth from the periosteum surface of the half-diaphysis. The end mill cutter was then stepped down a further millimeter and another cut along the trace of the rectangular block was done. This process continued until the block was detached from the rest of the half-diaphysis. The end mill cutter was run at a speed of about 2000rpm with the table feed rate set at 15mm/min (set as f15 in the gcode). After obtaining the rectangular block, it was flattened on both the endosteum and periosteum side using a ¼ inch end mill cutter. Again, the flattening is carried out by running the cutter at a cutting depth of 1mm from the highest point on the surface and stepping it down until the surface of the block is completely flattened. A lower speed of about 1500rpm was used but the table feed rate of 15mm/min was maintained. Finally, the ends of the rectangular block along the long axis of the bone was cut off. This was because the step blocks were mounted at these ends hence were not flattened with the rest of the rectangular block. This fine cutting process produced a final rectangular block approximately 5mm in thickness, 15mm in width and 50mm in length.

Next, two parallel beams were cut from the block with the aid of a low speed metallurgical saw (Isomet, Buehler, Lake Bluff, IL, US). The metallurgical saw was equipped with a 300µm diamond

wafering blade (15HC diamond, Isomet, Buehler, Lake Bluff, IL, US). Cutting by the low speed saw is done wet. To cut the beams, the rectangular block from the previous cutting step was mounted securely in an irregular specimen chuck (Buehler, Lake Bluff, IL, US). To begin, a thin slice of the rectangular block at the end closest to the wafering blade was cut off. This was done to ensure all further cuts produced beams with parallel sides. The cut was performed by screwing the chuck with the mounted block unto the support arm of the metallurgical saw. The wafering blade was set to a 250rpm speed (roughly 8 on the speed knob). The weight at the end of the support arm that held the mounted specimen away from the blade was taken off and other weights were put at the front end of the support arm. The cutting arm was lowered gently unto the already rotating blade and allowed to cut through the block under gravity. After, the thin slice is cut off, the current position of the rectangular block was considered as a zero position. A micrometer screw gauge was attached to the support arm which allowed measurement of the movement of the support arm in relation to the wafering blade. Using the micrometer screw gauge, the rectangular block was moved 4.5mm. The 4.5mm shift accounted for the 4mm width cut wanted, 0.3mm for the width of the wafering blade and 0.2mm as allowance for cutting and polishing. The cutting procedure for the thin slice cut was repeated to cut two beams. This gave rise to two rectangular beams roughly 4.2mm in width, 5mm in thickness and 50mm in length, where the thickness is measured from the endosteum surface to the periosteum surface (across the radial direction)

3.3.2 Polishing and notching of SENB specimen

After obtaining the two rectangular beams, they were then polished. The polishing was done using circular metal bonded diamond disc 8” in diameter (UltraPrep, Buehler, Lake Bluff, IL, US). These diamond disc had diamond particles embedded on their surfaces. Three diamond discs with different sized diamond particles: 45,15 and 9µm were utilised. The beams were first polished using the 45µm disc, followed by the 15µm disc and lastly the 9µm disc. The polishing was done by hand. The polishing was performed by spreading a thin layer of water over the diamond disc and with lightly applied pressure on the beam, the surface of interest is run over the disc in about 100-150 circular cycles. The polishing was done on all surfaces of the beams apart from the cross-sectional surfaces. The surfaces of the beams corresponding to the periosteum and endosteum surfaces were tracked as this will be important for ensuring accurate notching. A final polishing stage was undertaken to give a finer and smoother surface. A finer and smoother surface aided in the strain measurements with DIC. This final stage used a polycrystalline diamond suspension

(MetaDi Supreme, Buehler, Lake Bluff, IL, US) to polish the surfaces. The size of the diamonds suspended in the slurry were 6µm. This polishing was done in a similar manner to that with the diamond disc with the water being replaced with the diamond slurry and the disc with a synthetic rayon polishing cloth (MicroCloth, Buehler, Lake Bluff, IL, US). All the polishing stages were performed such that the beams had their final dimensions of 4±0.05mm in width, 4±0.05mm in thickness and 50±1.0mm in length. The width and thickness of the beams was measured using a digital micrometer screw gauge. These dimensions were taken at three different positions, the two edges and one at the mid-section of the beams and these values were averaged out to get a final single value for each dimension. The length was measured using a ruler. These dimensions were crosschecked once to ensure their accuracy.

The last step in preparing the SENB specimens was creating a notch in each. The notching stage was divided into two steps: a macro-notching stage and micro-notching stage. The notching process was carried out in this manner to replicate closely the ASTM E1820 guidelines for a SENB specimen. The macro-notch was machined using the low speed metallurgical saw (Isomet, Buehler, Lake Bluff, IL, US). The macro-notch was cut in the mid span of the beams along the circumferential direction as shown in Figure 3.10. The depth of the macro-notch was 1.8mm. The depth was measured by a customised micrometer screw gauge attached to the low speed saw.

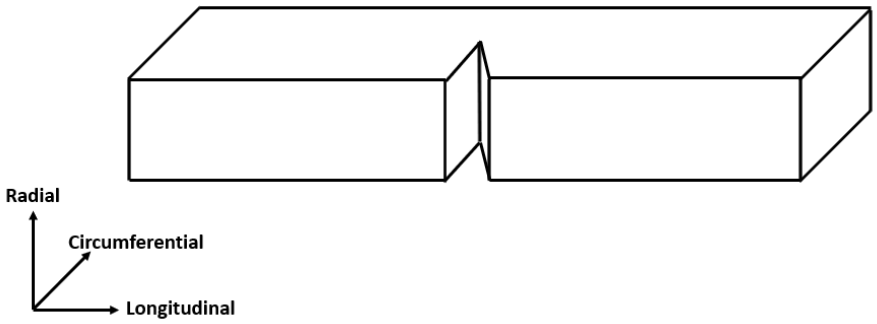

Figure 3.10: Diagram showing direction in which macro-notching was done

The beams were mounted securely one at a time into a dressing blade chunk. The beams were mounted such that the midspan of the beam in the circumferential direction aligned with the

diamond wafering blade. With the mounted beam a few millimeters back, the wafering blade was started and set to a speed of 250rpm (8 on the speed knob). The mounted beam was gradually brought towards the rotating wafering blade using the handwheel at the end of the chunk. At the first hint of the beam touching the blade, the micrometer gauge is zeroed. The beam is gradually moved into the blade using the handwheel of the chunk until the micrometer reads a depth of 1.8mm has been cut. Once at this point, the beam was gradually pulled away from the wafering blade and the macro-notch was done.

For the micro-notch, the vertical mini-CNC mill was utilised. The micro-notch was cut using an ultra-sharp razor blade (American Line, Extra Keen Single Edge Blades). The razor blade was securely held in a custom razor blade holding system and screwed into the end mill holder of the mini-CNC mill. The macro-notched beam was securely fixed on the table of the mill with the step block hold down sets. The surface with the macro-notch faced upward to allow the mounted razor blade to slide through. A rough sandpaper was put under the clamped macro-notched beam to prevent slipping as the micro-notch was created. To allow for easy creation of the sharpened (micro) notch, 1-2 drops of 1µm diamond suspension slurry was used as a lubricant. The drops were allowed to flow into the base of the macro-notch. The razor blade was then gently guided and slid through the macro-notch until it touched the base of the macro-notch. This position was the zero position. The mini-CNC mill was then programmed to move the razor blade across the base of the macro-notch and then stepped down by 0.02mm to create a cut ahead of the base of the macro-notch. This sequence of moving the razor blade across the base of the previous cut and stepping down by 0.02mm was repeated until a micro-notch of 0.2mm was achieved. Figure 3.11 shows the micro-notch (pre-crack) ahead of the macro-notch for one of the specimens. The combined length of the macro and micro-notch was 2mm, half the thickness of the beam. This finalised the preparation of the SENB specimen.

After notching, the beams were wrapped with gauzes soaked in phosphate buffer saline (PBS) solution containing one millimole (mM) of calcium ions and re-frozen at -20˚C. The preparation of the beams took about 6 hours and dried up during the process. Wrapping a gauze soaked in PBS around the beams allowed them to return closely to their initial physiological state and keep them in this state until mechanical testing was performed [119]. Further, the protocol used in the preparation was adopted to reduce damage to the beams during their preparation. It was mainly

done by reducing the heat production during the different forms of cutting and polishing. This explains why a 1mm depth step by step cutting was adopted for the CNC mill cutting, water was used in polishing as well as the beams lubricated for micro-notching.

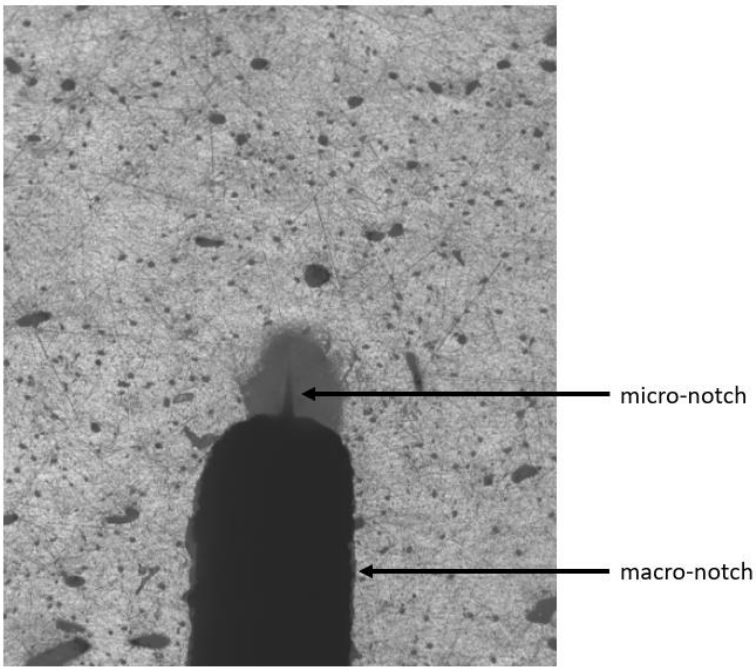

Figure 3.11: An example of a micro-notch (pre-crack) ahead of the macro-notch of the one of the SENB bovine cortical bone specimens used. This image was taken under a microscope

3.3.3 Mechanical testing

Prior to mechanical testing, the frozen SENB specimens were thawed and soaked in PBS solution containing one mM calcium ions for 5 hours both at room temperature. As discussed in Section 1.7, analysis with DIC requires the surface under analysis to have a large greyscale gradient for more accurate results. An earlier study done in our lab (unpublished) showed that the use of a speckle pattern on the 6µm polished specimen surface of interest provided the best greyscale gradient for the DIC analysis compared with other alternatives including the natural 6µm polished specimen surface with no speckle pattern. Therefore, after soaking the specimen in PBS solution, a speckle pattern was created on the surface of interest (either the endosteum or periosteum surface) using high resolution toner powder (Xerox Phaser 6000 laser toner cartridge). The diameter of a single toner powder was approximately 5-6µm. This speckle pattern was created just before the three-point bending test was performed. The toner powder was placed in an atomiser jar. The atomiser jar allowed the creation of a cloud of the toner powder over the surface of interest.

The toner powder in the cloud eventually settled on the surface creating a randomised pattern on the specimen surface (Figure 3.12). A thin layer of hair spray was applied to the surface of interest before the toner powder was sprayed on it to act as an adhesive. This was important for accurate DIC results, as the random speckle pattern created must deform along with the specimen surface.

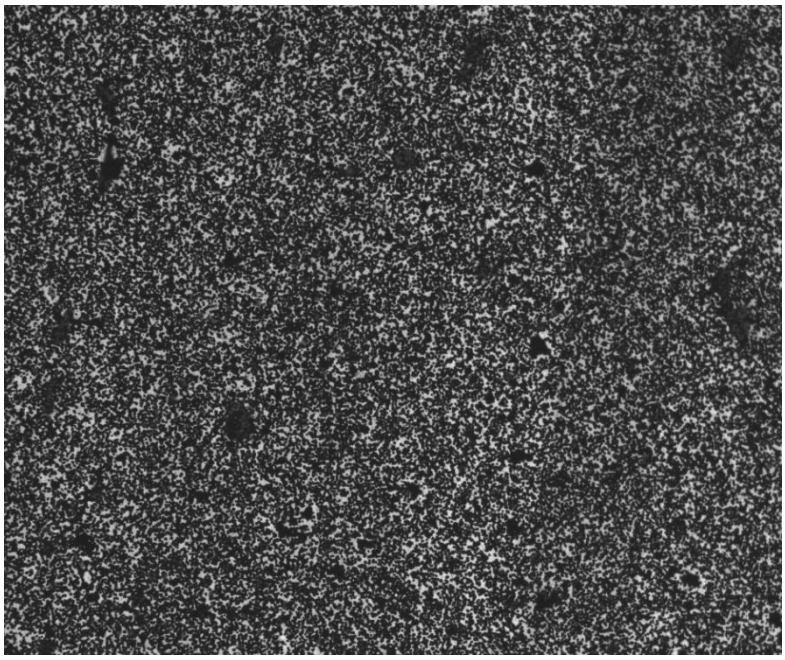

Figure 3.12: The randomised speckle pattern generated on the SENB bovine cortical specimen for DIC analysis

Immediately after the creation of the speckle pattern, the SENB specimen underwent a three-point bending test. The bending test was carried out with µTS universal mechanical testing machine (Psylotech, Evanston, IL, US). The test system was mounted on a vibration isolating workstation (Vision IsoStation, Newport Corp., California, US). This workstation prevents ambient vibration (10-50Hz) from influencing the performance of devices mounted on it. Also mounted unto the vibration isolated workstation and over the test system was a microscope (Olympus Corp., Center Valley, PA, US) embedded with a 5 megapixel camera (HSI, Correlated solutions, Irmo, SC, US) (See Figure 3.13). The specimen was mounted such that the loading nose was placed on the unnotched side of the specimen at the midspan. In other words, the loading nose was placed directly in line with the notch (Figure 3.9). This was necessary to obtain a pure Mode I loading configuration. Further, a 5X magnification objective lens (Olympus Corp., Center Valley, PA, US) attached to the microscope was used to focus on the region around the pre-crack (micro-notch) in

the specimen. The specimen was then preloaded to 1N and the test was run until rupture. The test was run in displacement control at a rate of 0.2mm/min. The force and load-line deflection of the beam was recorded at a sampling rate of 20Hz. The force was measured by a 1.6kN capacitive, windowing load cell (100N range, 50mN resolution) while the deflection was measured by a windowing, capacitive displacement sensor with a 100nm resolution.

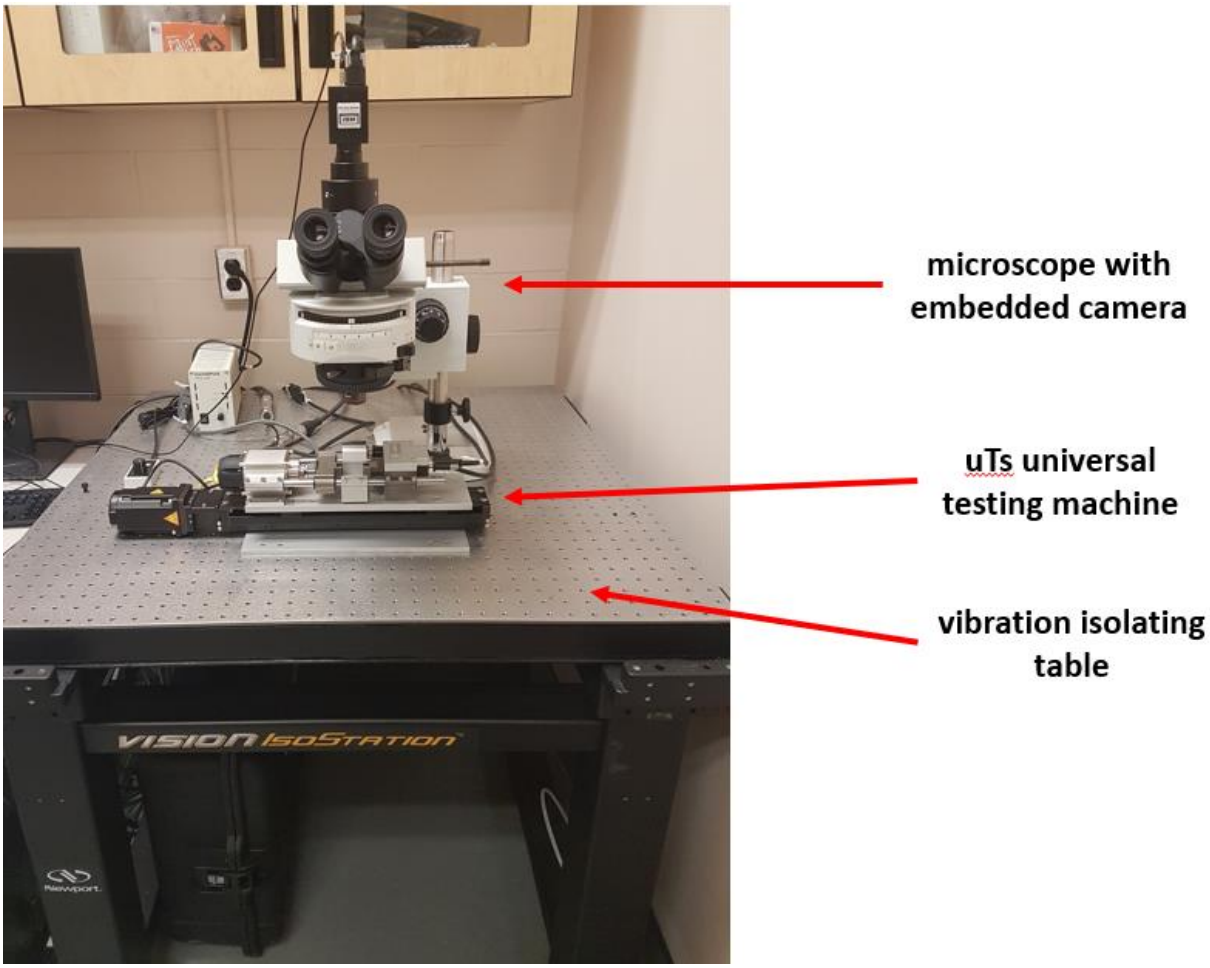

Figure 3.13: Psylotech micro test system with a microscope embedded with a high-speed camera mounted over it on a vision isostation table

Throughout the test, images of the region around the pre-crack were taken at a 20Hz frequency by the camera embedded in the microscope. The images were then analysed using the DIC analysis software, Vic 2D (v6, Correlated solutions, Irmo, SC, US). The software was used to calculate the strain field distribution around the region of the crack. The analysis was carried out by defining as large as possible rectangular region of interest ahead of the crack tip (Figure 3.14). A subset size between 81-100 and step size of 7 were used then defined over this ROI. These values were

suggested by the software based on an internal algorithm that estimates the best possible values to use. The zero-normalised squared difference criterion was used as the correlation criterion and an optimised 8-tap interpolation scheme was used. The analysis was run to first calculate the full-field displacement distribution and afterwards the full field strain distributions. The strain field distribution result from the DIC was discretized to show the region of microdamage formation ahead of the pre-crack tip. To know the threshold strain, beyond which microdamage formation should have occurred for a particular specimen, the equation below was used.

$$\varepsilon_t = \frac{X^T}{E_1} \tag{3.15}$$

where ε_t is the threshold strain beyond which microdamage has occurred, X^T is the Hashin longitudinal tensile strength defined and E_1 is the longitudinal elastic modulus defined for the particular specimen.

The calculated strain value was verified by comparing it to the threshold strain value for MDPZ formation in that specimen's CDM model simulation. Finally, the size of the MDPZ from the DIC analysis was compared to that generated by the CDM model in order to validate the model.

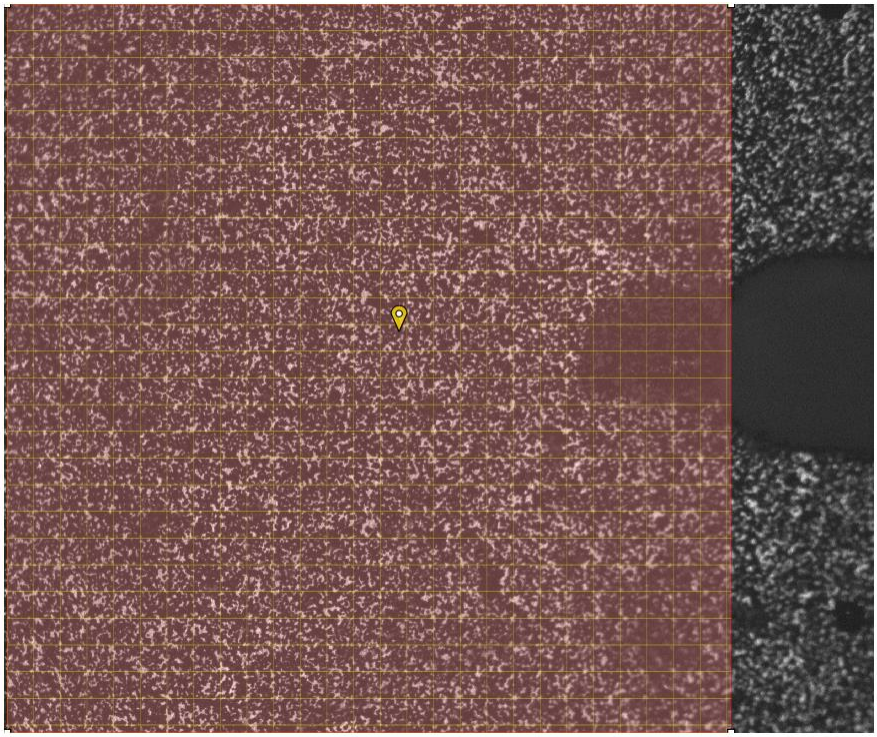

Figure 3.14: Region of interest defined around crack tip showing subset gridlines for DIC analysis

The area of the MDPZ defined using the DIC strain field measurements at different secant modulus percent losses (5%, 10%,15%, maximum initial modulus losses) were measured using ImageJ software (NIH, Bethesda, Maryland, USA). This was accomplished by using the color threshold function in the software (See Figure 3.15). The color threshold allowed the MDPZ zone to be selected and the area determined using the Analyze-measure function in the software.

Additionally, the crack mouth opening displacement (CMOD) was measured using DIC. A narrower rectangular field of interest was chosen for this analysis (Figure 3.16). This field of interest allowed the maximum displacement to occur at or close to the crack mouth and therefore roughly represented the CMOD throughout the bending test. The same DIC settings used in capturing the microdamage process zone was also utilised in analysing for the CMOD measurements.

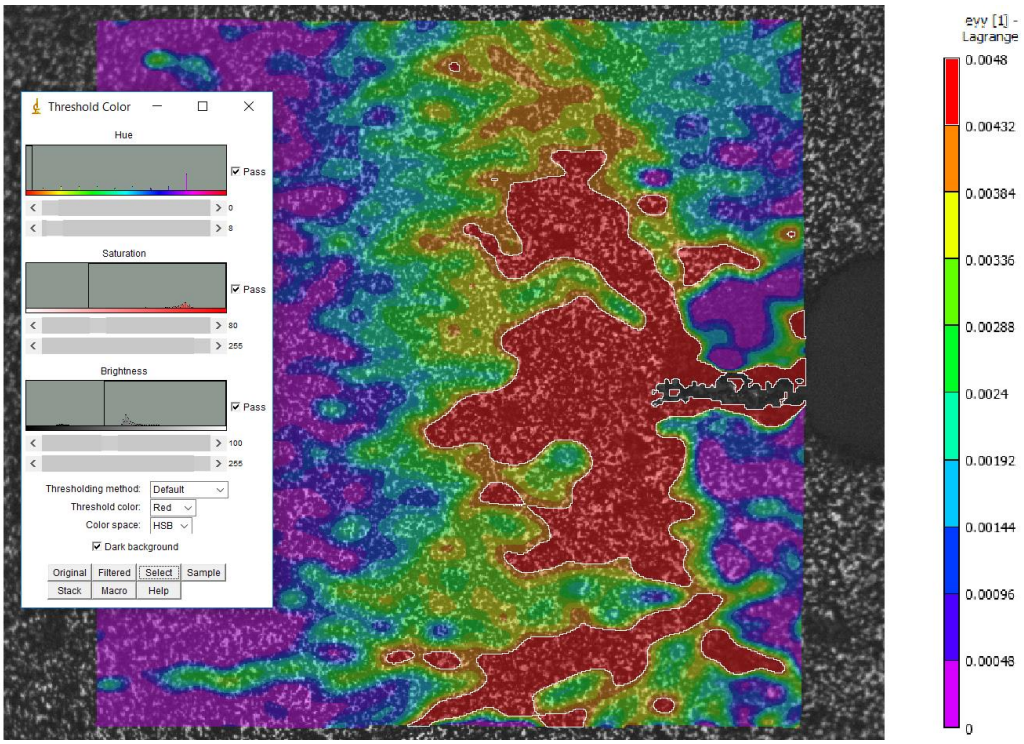

Figure 3.15: The threshold color function for selecting the MDPZ determined using DIC

3.4 Comparison with microdamage imaging study

For further validation of the CDM model, the model was compared to experimental results obtained in the MDPZ imaging study in Willett et al. [78]. In the MDPZ imaging study, the MDPZ size and shape was approximated to an ellipse and the height and width of the MDPZ for the different specimens (5 specimens were used) were measured at different percent secant stiffness loss. The height and width of the MDPZ generated with the CDM model was compared to the reported height and width curves from the experimental study. The load versus load-deflection curves were also compared to ascertain if they matched.

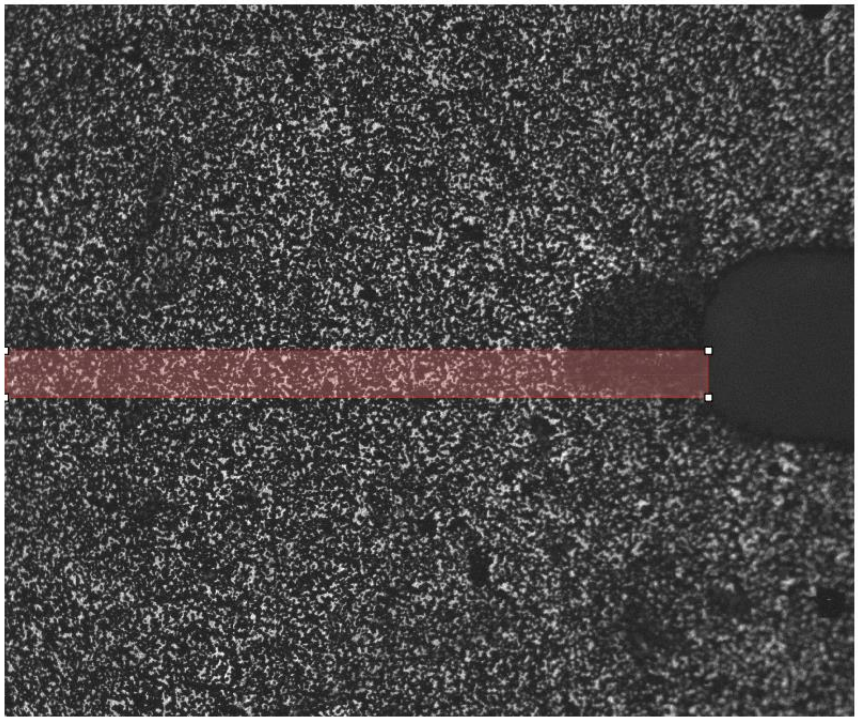

Figure 3.16: Region of interest defined for crack mouth opening displacement measurements using DIC

3.5 Application of model to two case studies

To show the applicability of the model, the model was used to simulate two different case studies of bovine cortical bone as compared to work done in Willett et al. [78]. The first was to simulate

the MDPZ for a longitudinal directed crack as opposed to the transverse directed crack study in Willett et al. [78]. This is simply done by switching directions in the model. In other words, the longitudinal and transverse direction in the transverse directed crack becomes the transverse and longitudinal directions in the longitudinal directed crack respectively. It was expected that a narrower MDPZ will be formed for the longitudinal transverse directed crack compared to the transversely directed crack

The second was based on work previously done in Prof. Willett's research program [57]. In that study, "normal" bovine cortical bone was irradiated with 33 kGy dose of gamma-radiation. This was to mimic the sterilisation process structural bone allografts undergo before implantation in patients with significant bone sized defects. This irradiated specimen was simulated in the model to determine its MDPZ. A combination of mechanical properties defined for irradiated bovine cortical bone in [120] and the load versus load-line deflection curve obtained from [57] for one of the irradiated SENB bone specimens (same dimensions as defined for the model) were used to define mechanical properties for the model to generate the MDPZ. The specific load versus load-line deflection curve picked from [57] was one whose initial bending stiffness matched closely to the one picked from the MDPZ imaging study in [78]. This allowed for the elastic moduli to remain the same as those used in the simulation for the specimen from [78]. Further, Willett et al. [120] reported about a 5% decline in yield strength and a 40% decline in failure strain for irradiated specimens compared to ones that were not been irradiated. Using a 5% decline rule for Hashin strengths and a 40% decline rule for failure strains, the Hashin strengths and fracture energies were calculated from those used in the simulation for the specimen from [78]. The viscosity parameter was then defined to fit the CDM model's load versus load-line deflection curve to the experimentally determined one. Since the mechanical properties were defined based on those of the bovine tibia specimen simulation, it was used as a comparative control in this case study. The crack was directed in the circumferential direction on the transverse plane for the irradiated bone specimens also. It was expected that a narrower MDPZ will be formed in the irradiated cortical bone as compared to the non-irradiated ones [121].

The various mechanical properties utilised in the model for each case study are reported in the Appendix.

Chapter 4

Results

4.1 Verification of bi-linear CDM law

To verify, the CDM bi-linear law as defined, the model was used to run a simple tensile test in the longitudinal direction. Figure 4.1 shows the stress versus strain curve for the longitudinal tensile test and was adopted from one of the elements used to mesh the specimen. It should be noted that since it was a simple tensile loading configuration, all elements in the model behaved the same in terms of stress and strain. The stress versus strain curve was clearly observed to follow the CDM bi-linear law for the longitudinal tension failure mode. The stress reached its peak at the Hashin failure strength which was defined as 95MPa (Appendix). From this point, the stiffness began to degrade and reached zero at a strain of 0.02, which was the defined failure strain for this failure mode (see

Table 3.1). This demonstrates that the elements obey the CDM bi-linear law as assigned.

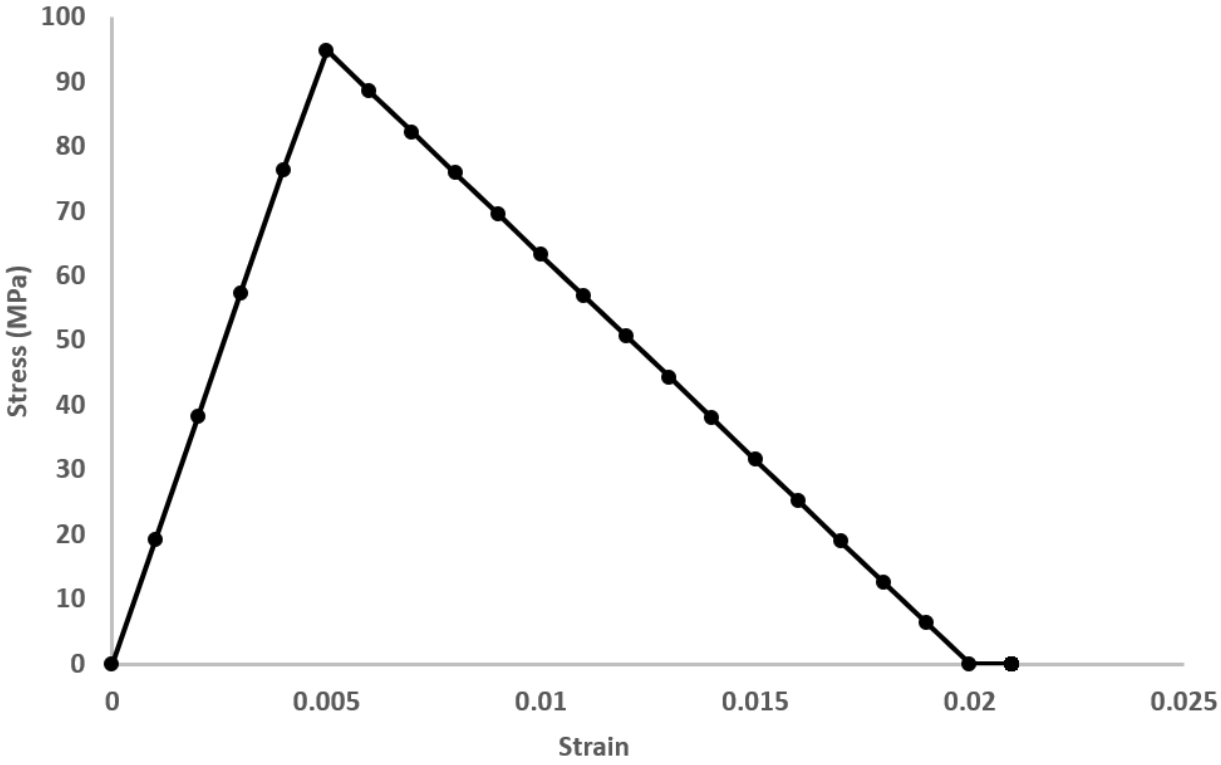

Figure 4.1: Stress-strain curve generated from model depicting the CDM bi-linear law for the longitudinal tension failure mode

However, in the CDM model, a viscous regularisation scheme was incorporated to introduce viscoelastic effects. Figure 4.2 shows the change in the stress versus strain when this scheme is implemented in the simple longitudinal tensile test. It is noticed that this scheme allows the elements to exceed their Hashin strength and failure strain limits. The importance of this behaviour will be elaborated on in Chapter 5.

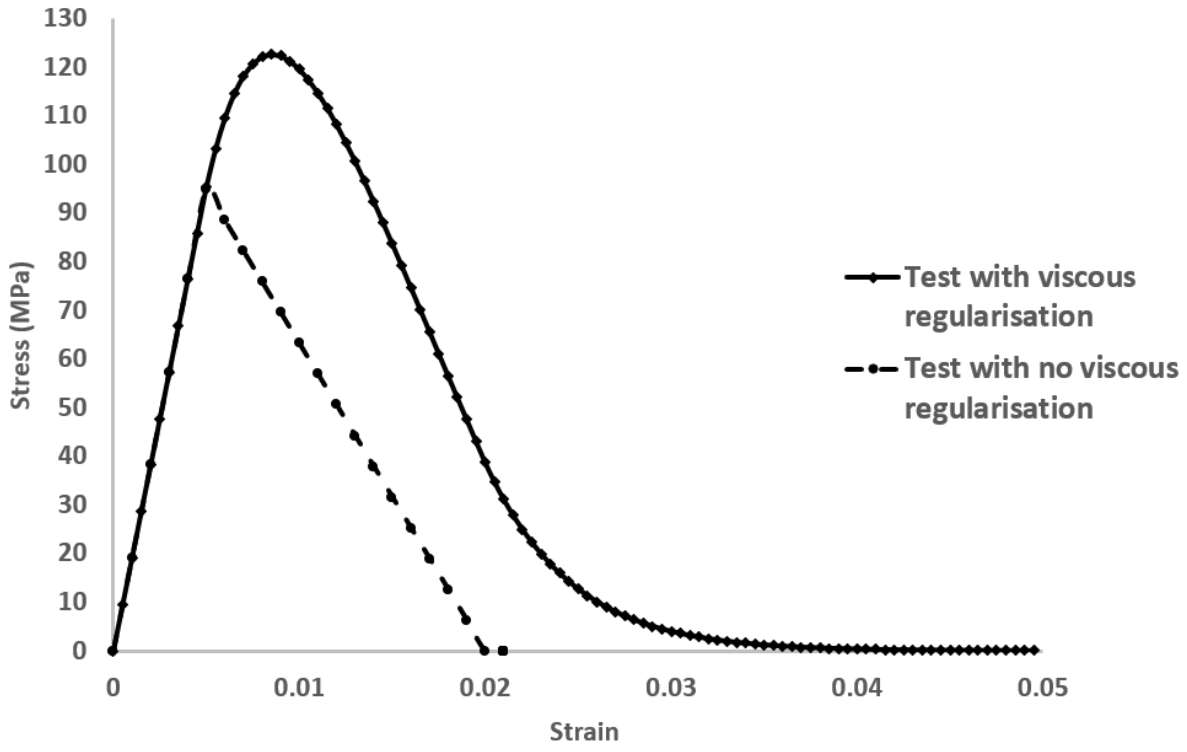

Figure 4.2: Stress-strain curve generated from model depicting the change in CDM bi-linear law for the longitudinal tensile failure mode when viscous regularisation scheme in ABAQUS is implemented (solid line)

Figure 4.3 shows the equivalent stress-strain relationship but for a transverse tensile loading configuration. Similarly, the stiffness is constant till it reaches the Hashin transverse tensile strength (defined as 50MPa) then begins to degrade from this point until it reaches zero at the failure strain of 0.007.

Figure 4.4 shows the change in the stress versus strain curve when the viscous regularisation scheme was implemented for the same transverse loading configuration mentioned above. Similar to the longitudinal case, the Hashin strengths and failure strains limits are exceeded.

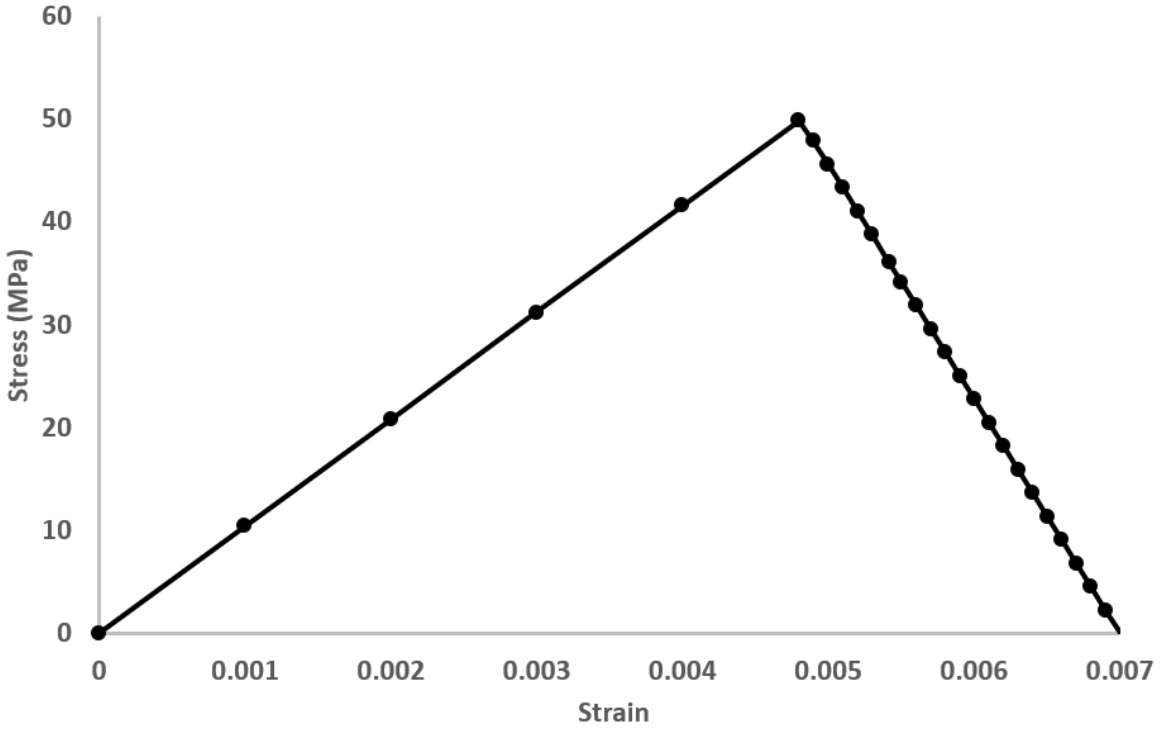

Figure 4.3: Stress-strain curve generated from model depicting the CDM bi-linear law for the transverse tension failure mode

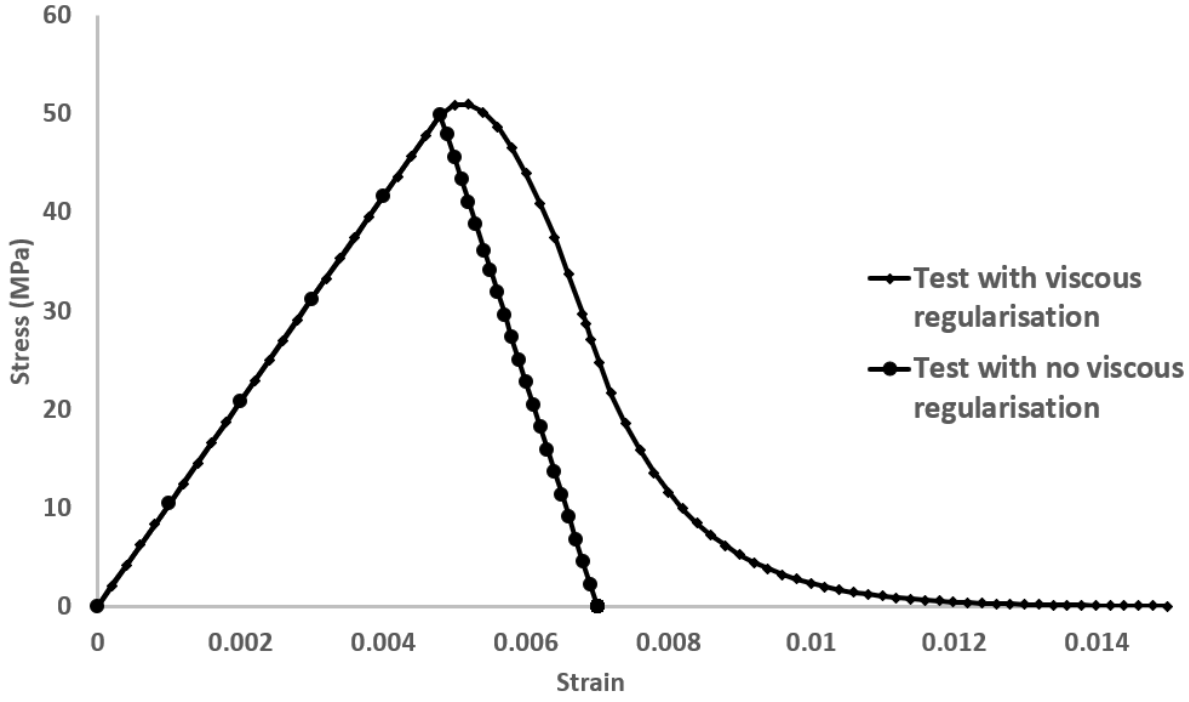

Figure 4.4: Stress-strain curve generated from model depicting the change in CDM bi-linear law for the transverse tensile failure mode when viscous regularisation scheme in ABAQUS is implemented (solid line)

4.2 Verification of material definition, mesh pattern and mesh size

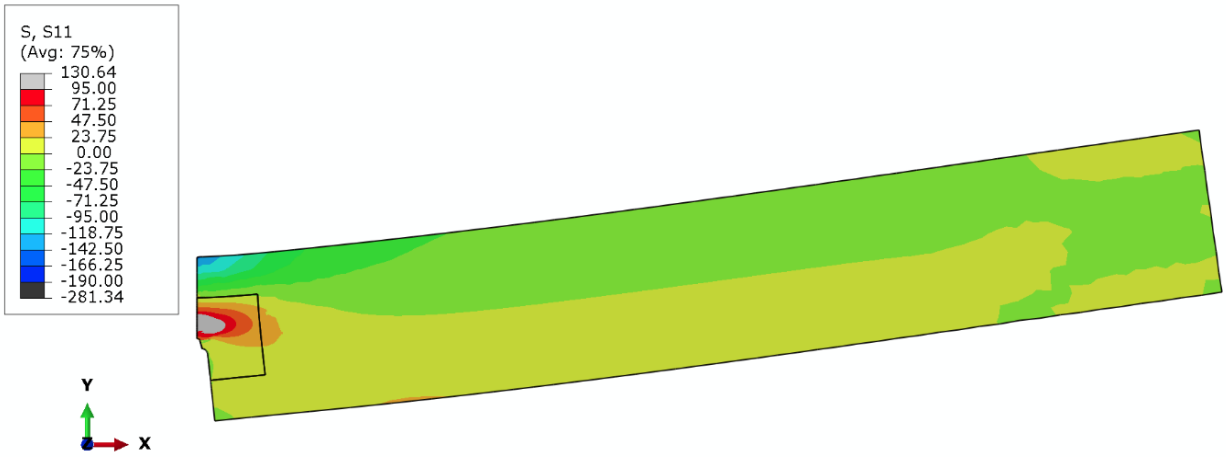

Figure 4.5: Stress field distribution in the longitudinal direction (S11) for the SENB specimen at complete failure (fracture). The grey region denotes the area that has exceeded the longitudinal tension Hashin strength at fracture. The black lines within the SENB specimen enclose the area prescribed as the region of interest.

Figure 4.5 represents the stress distribution in the longitudinal direction across the sample model approximately at the point of rupture of the bovine specimen. The Hashin failure strengths for the longitudinal direction was set at 95MPa and 190MPa for tension and compression respectively. From the legend in Figure 4.5, grey or black regions will represent regions exceeding the defined longitudinal tension and compression Hashin failure strengths respectively. The black lines within the SENB specimen (Figure 4.5) enclose the area prescribed as the region of interest (ROI) for microdamage formation. In the methods chapter (Section 3.2.1 and 3.2.2), it was stated this ROI was meshed with smaller quadratic elements with stiffness degradation capability while the rest of the specimen was meshed with larger linear elements without stiffness degradation capability. It can be noticed that outside the ROI, the stress induced is mostly between -70MPa to 23MPa, which are well below their respective Hashin failure strengths. This confirms that the approach of meshing with larger linear elements as well as not assigning stiffness degradation capability for the area outside the ROI is reasonable and does not affect the final results obtained from the CDM model.

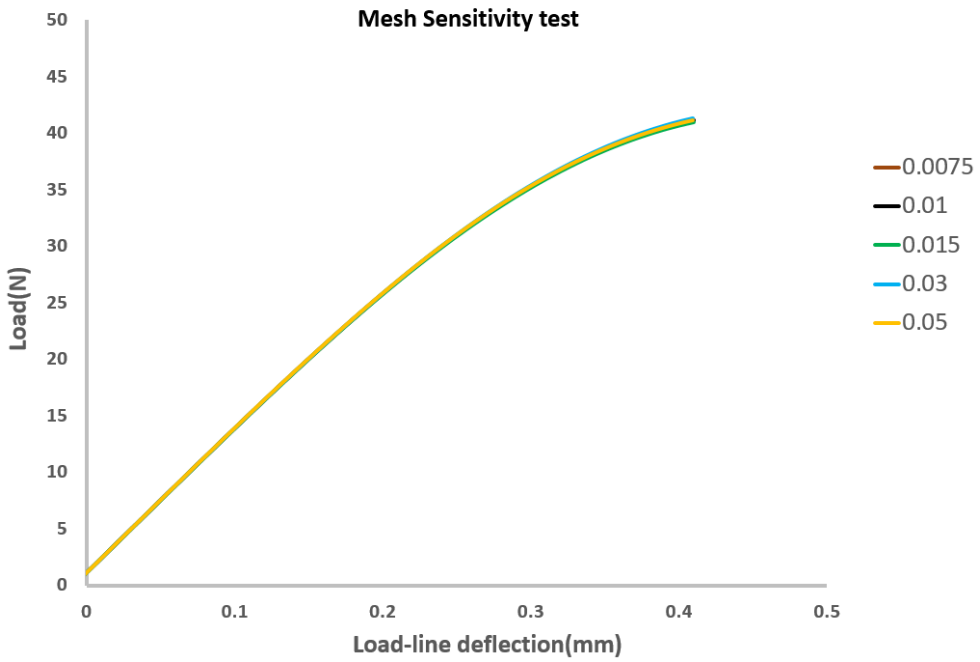

Figure 4.6: Load- deflection curves generated from the model for different mesh sizes of the ROI. The numbers in the legend represent the mesh size in microns.

As shown in Figure 4.6, the same load versus load-line deflection curve was generated from the model for different mesh sizes. This shows the model is independent of mesh size. It should however be noted that, the fracture energies prescribed in the model were changed to match the mesh size used.

4.3 CDM model and experimental validation results for bovine femur specimens

4.3.1 Microdamage process zone from CDM model

The microdamage process zone (MDPZ) generated with the CDM model for the two femur specimens used for the experimental validation with DIC are shown in Figure 4.7 and Figure 4.8. The grey coloured region in the various images represent the MDPZ. This is the region that has reached or exceeded the longitudinal tension Hashin failure strength. This is reflected in the model as a value of 1 or greater for the HSNFTCRT output (shown in legend). The P values used in the two figures represent the percentage secant modulus loss. For instance, P10 signifies a 10% loss of stiffness from the initial stiffness from the linear portion of the load versus load-line deflection

curve. The MDPZ had a near elliptic shape expanding greatly as the model proceeded to rupture, represented as Pmax. This is consistent with experimental results from Willett et al. [78].

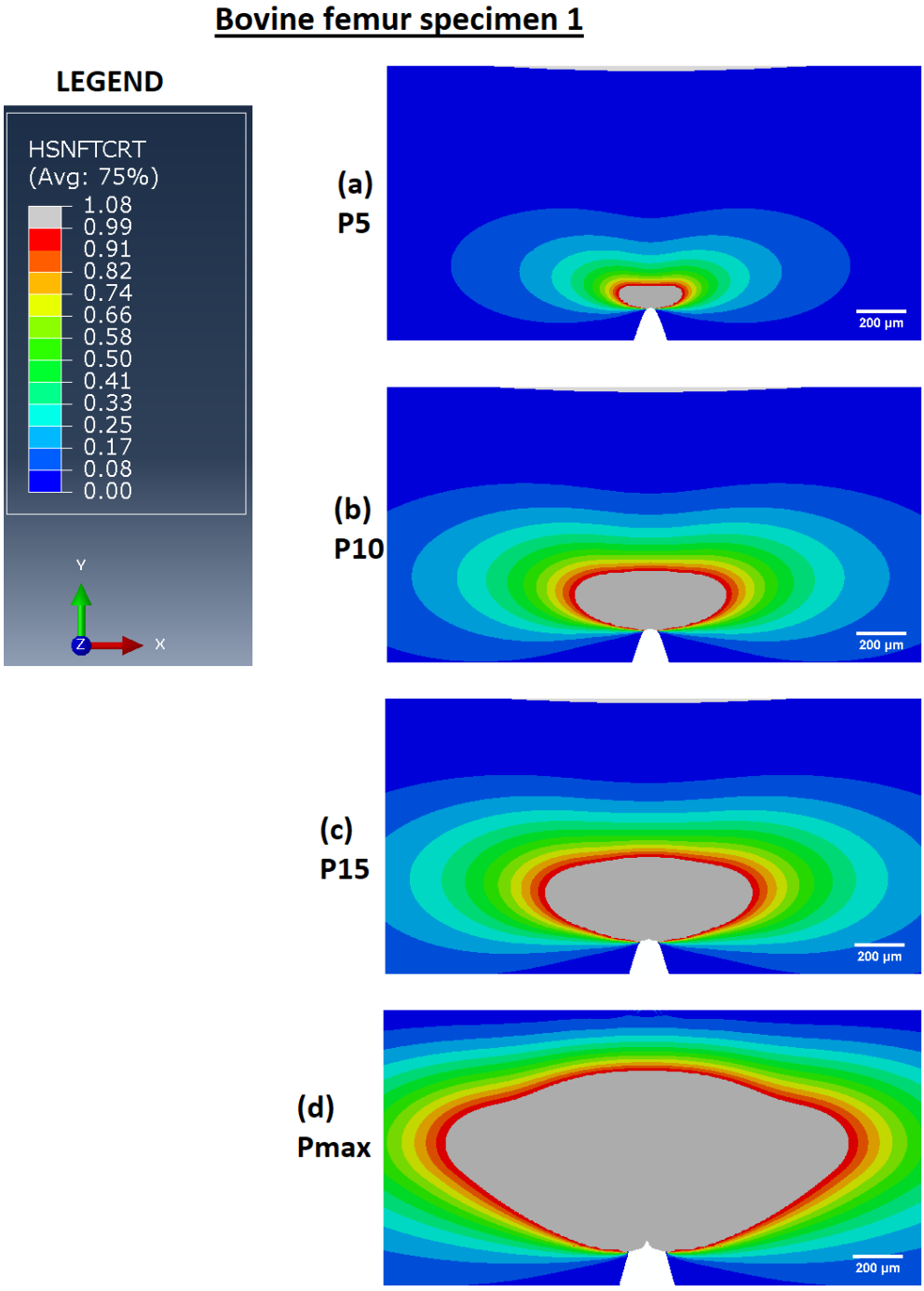

Figure 4.7: Microdamage process zone at different % secant stiffness loss (represented by P) for bovine femur specimen 1. The grey regions represent the microdamage process zone ahead of the crack tip. P5 means 5% secant stiffness loss, P10 means 10% secant stiffness loss, P15 means 15% secant stiffness loss and Pmax means maximum stiffness loss (stiffness is zero)

Figure 4.9 and Figure 4.10 demonstrate that indeed the CDM model was able to closely replicate the experimentally determined test curves.

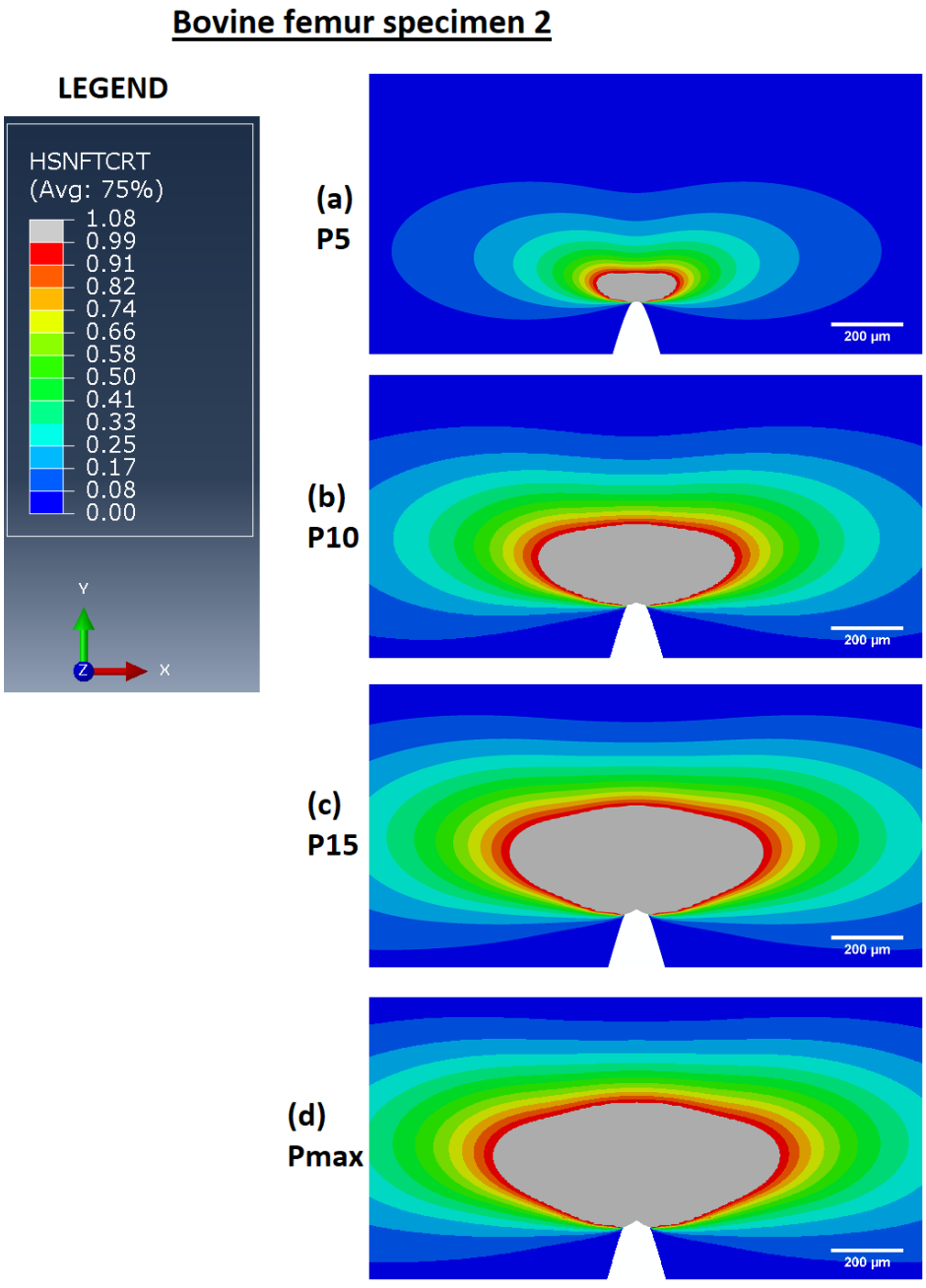

Figure 4.8: Microdamage process zone at different % secant modulus loss (represented by P) for bovine femur specimen 2. The grey regions represent the microdamage process zone ahead of the crack tip. P5 means 5% secant stiffness loss, P10 means 10% secant stiffness loss, P15 means 15% secant stiffness loss and Pmax means maximum stiffness loss (stiffness is zero)

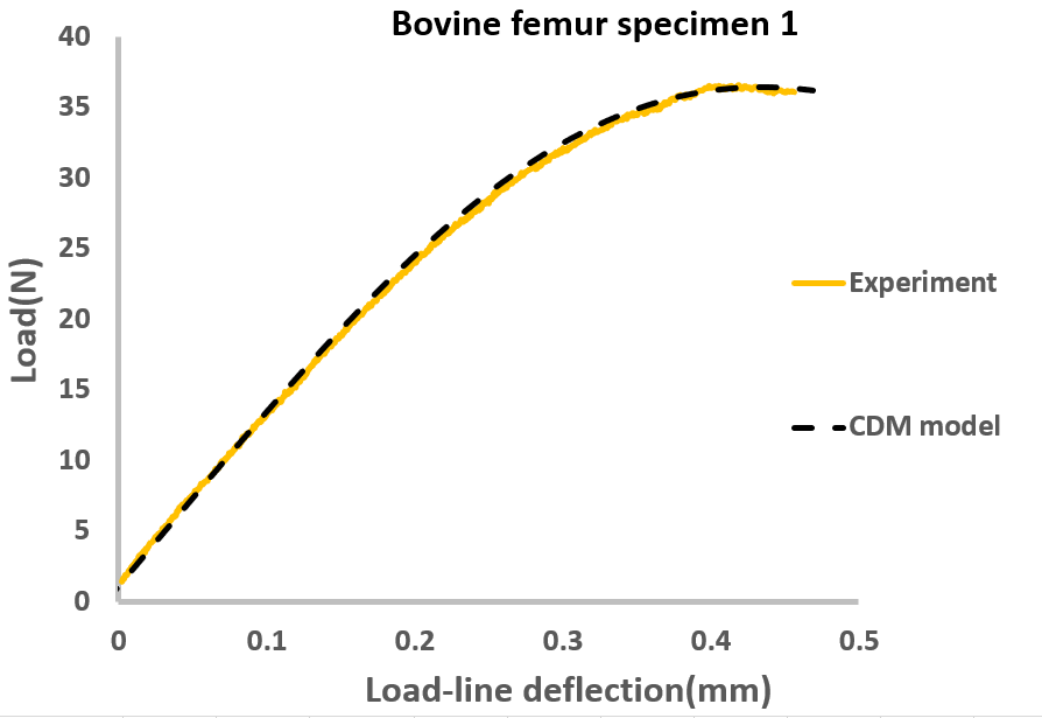

Figure 4.9: Load versus load line deflection curves comparison for bovine femur specimen 1

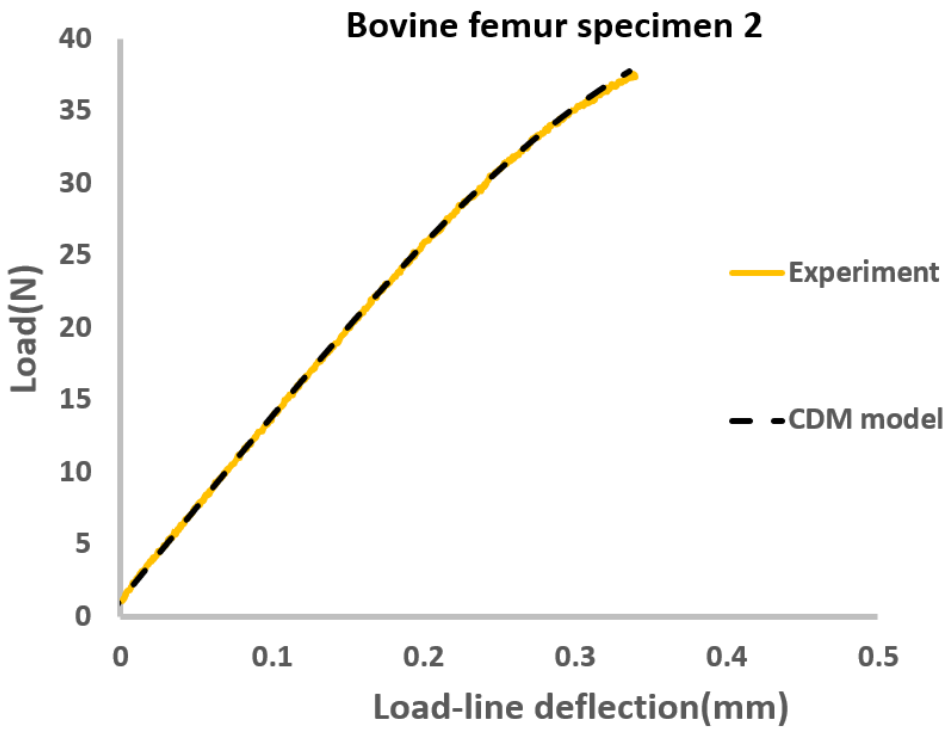

Figure 4.10: Load versus load line deflection curves comparison for bovine femur specimen 2

4.3.2 Model sensitivity to viscous regularisation

The load versus load-line deflection for the model run with a 10-fold lower viscosity parameter (η) is presented in Figure 4.11 (shown as CDM model with lower viscous regularisation). It was noticed that compared to the curves from experiment and the CDM model with a higher viscous regularisation, the lower viscous regularisation model produced a far smaller load versus deflection curve. It is important to remember that the only difference between the load-deflection curves for the two CDM models shown in Figure 4.11 is the viscosity (viscous regularisation) parameter as all other mechanical properties, geometry, mesh pattern, mesh size and boundary conditions were kept constant between the two. Figure 4.12 compares the MDPZ (the grey region represents the MDPZ for both models) between the two CDM models of varying viscosity parameter at a deflection of 0.22mm (this deflection represents the P10 deflection for the higher viscous parameter model). As observed, that the model with the lower viscosity parameter formed a longer but narrower MDPZ. The longer and narrower MDPZ means there will be greater crack growth for the lower viscous regularisation model. This can be shown by plotting the DAMAGEFT output for both models as done in Figure 4.13. The DAMAGEFT outputs 1 or more for elements that have completely failed. These elements can therefore be used to approximate crack growth. As can be seen in Figure 4.13, there is no crack growth for the higher viscous regularisation model but considerable crack growth for the lower viscous regularisation model. These show the importance of viscoelastic effects to modelling the MDPZ.

4.3.3 Microdamage process zone from experimentation using DIC

Figure 4.14 and Figure 4.15 show the microdamage process zone (MDPZ) measured using DIC for two bovine femur SENB specimens. The MDPZ is represented by the regions coloured red and reporting a strain greater than 0.004. It was noticed that damage caused to the bone material in machining the pre-crack (micro-notch) was coloured red in the DIC analysis under low loads (P5). This was accounted for in any comparisons in which the DIC MDPZ was used. Similar to the MDPZ from the model, the DIC's MDPZ grows greatly until rupture. However, unlike the model's MDPZ where it is continuous, the DIC's MDPZ is dispersed as a result of microstructural interactions and heterogeneity.

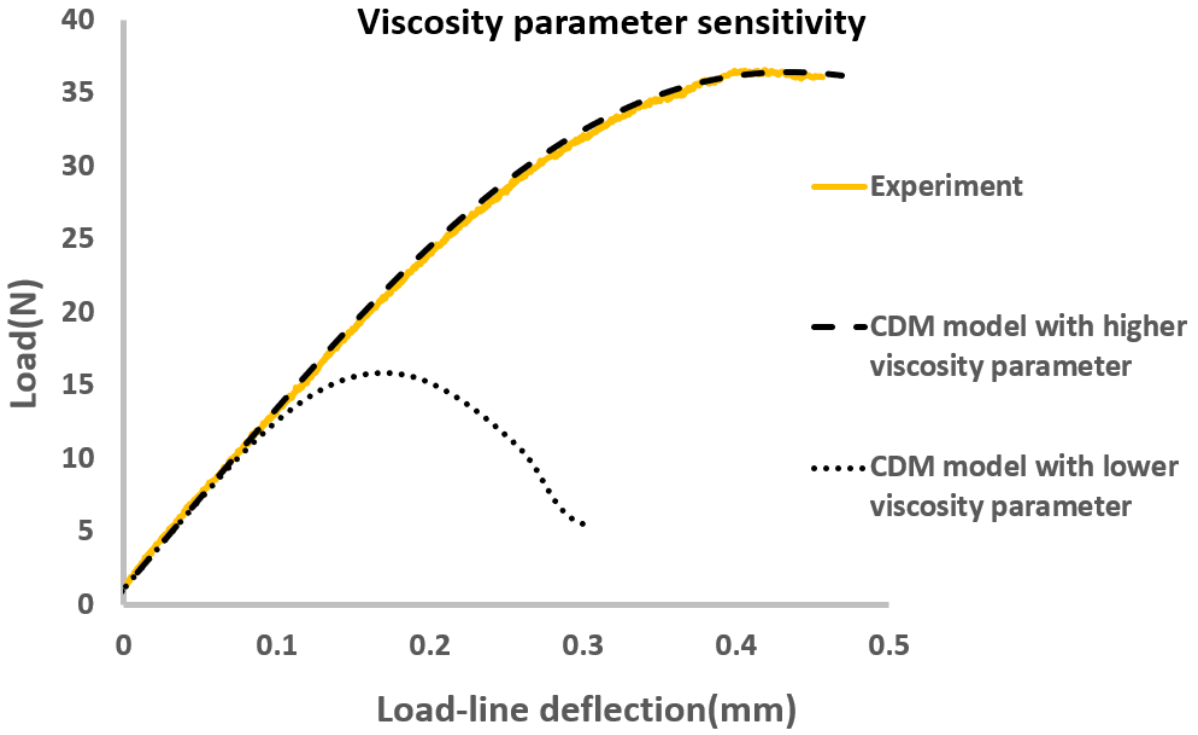

Figure 4.11: Load deflection curves for experimental femur specimen and two variations of CDM model simulations

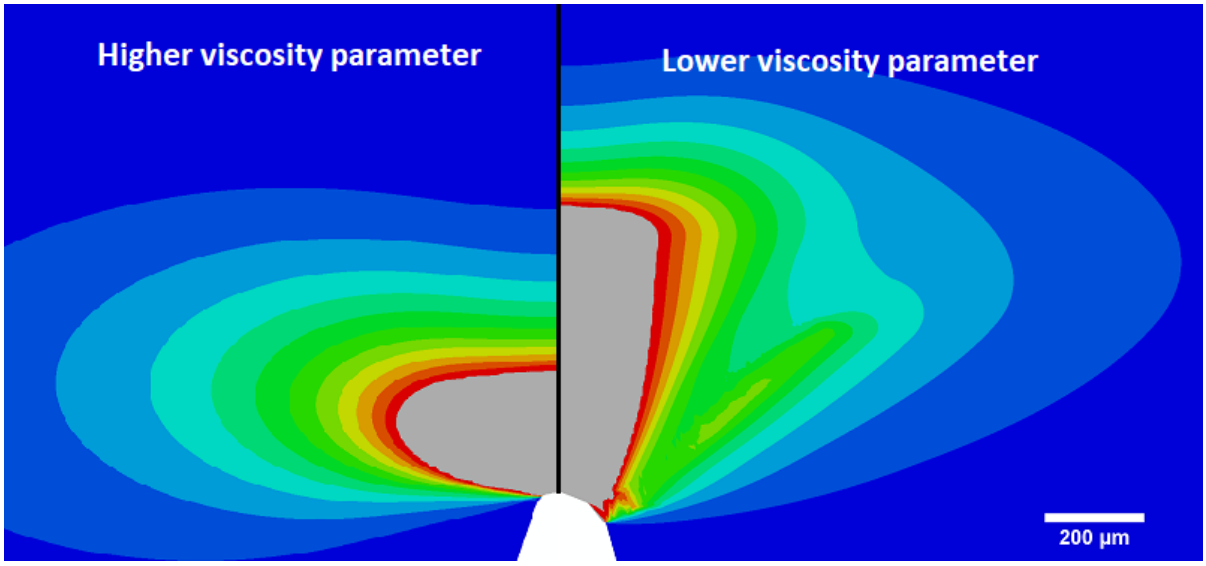

Figure 4.12: A comparison between MDPZ for a higher viscosity parameter model and a lower viscosity parameter model. The left side represents that of the higher viscosity parameter while the right side, the lower viscosity parameter model.

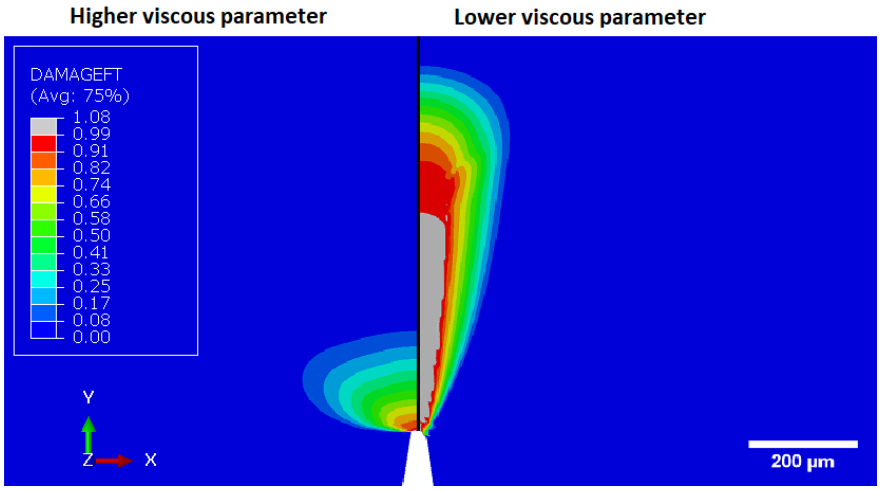

Figure 4.13: A comparison between completely failed elements for a higher viscosity parameter model and a lower viscosity model. The completely failed elements are representative of crack propagation. The left side represents that of the higher viscosity parameter whiles the right-hand side, the lower viscosity parameter

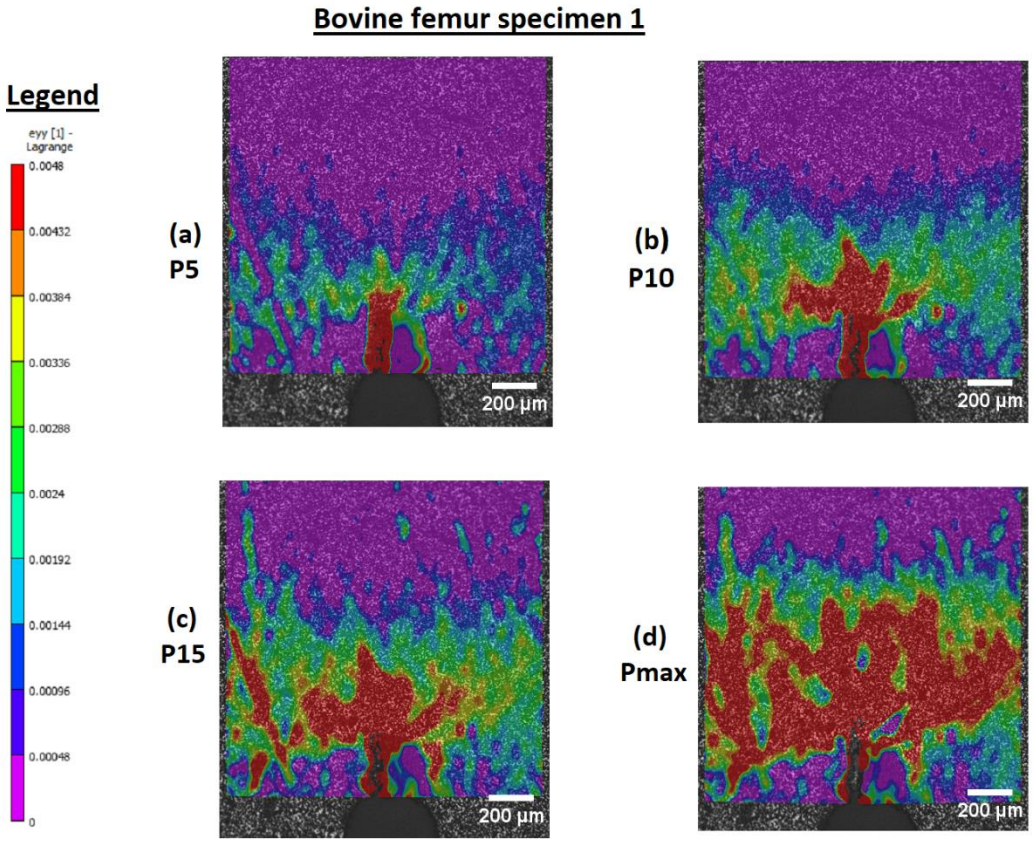

Figure 4.14: Microdamage process zone (MDPZ) for bovine femur specimen 1 determined using DIC. The red coloured regions represent the areas of microdamage formation. eyy represents strain in the direction normal the crack tip, P5 means 5% secant stiffness loss, P10 means 10%

secant stiffness loss, P15 means 15% secant stiffness loss and Pmax means maximum stiffness loss (stiffness is zero)

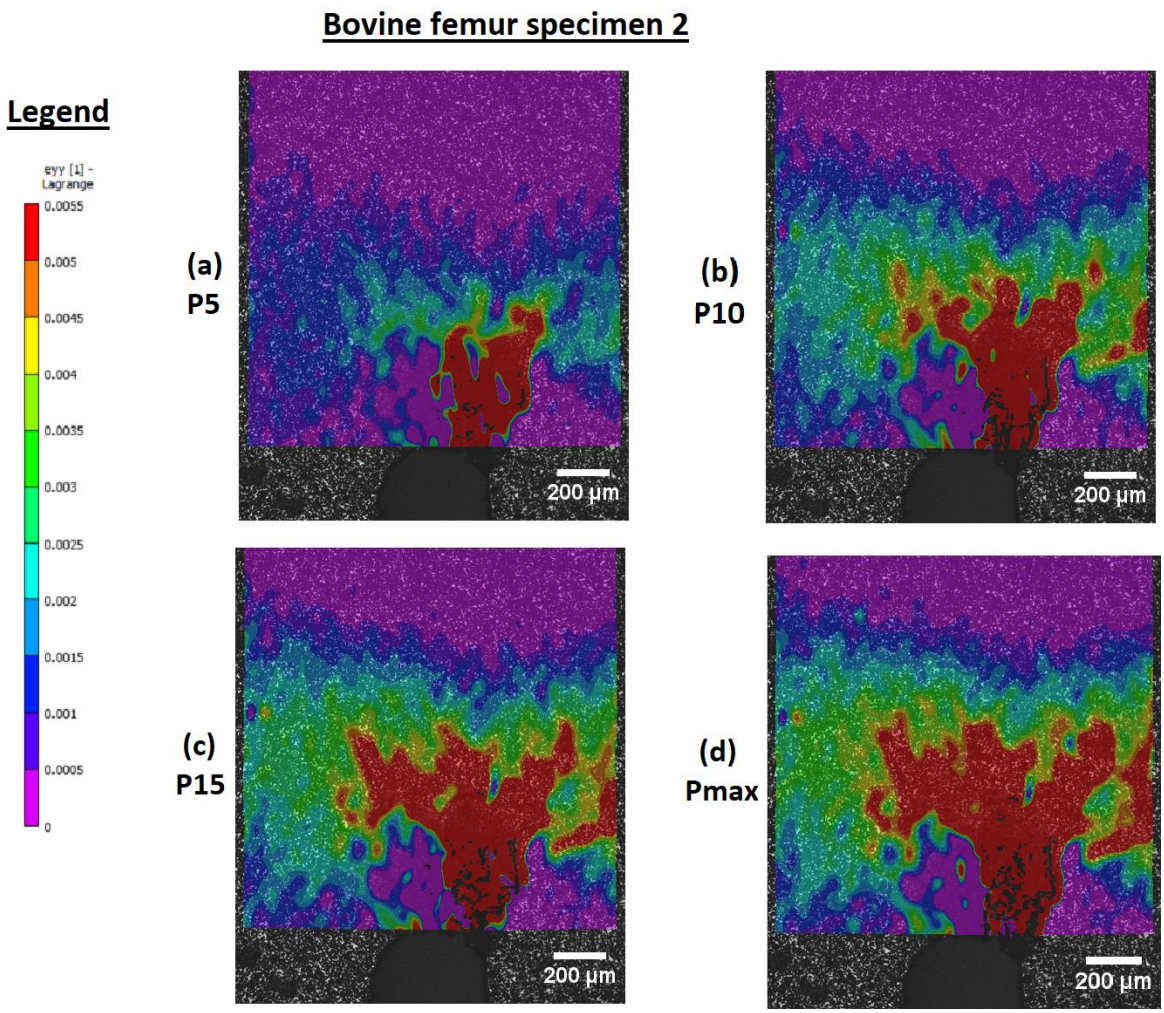

Figure 4.15: Microdamage process zone (MDPZ) for bovine femur specimen 2 determined using DIC. The red coloured regions represent the areas of microdamage formation. eyy represents strain in the direction normal the crack tip, P5 means 5% secant stiffness loss, P10 means 10% secant stiffness loss, P15 means 15% secant stiffness loss and Pmax means maximum stiffness loss (stiffness is zero)

4.3.4 Comparison between CDM model and experimentally generated microdamage process zone

To validate the CDM model, the microdamage process zone generated with the model was compared to that measured experimentally using DIC. The MDPZ of the CDM model at different P values was approximated to an ellipse and projected onto its equivalent P value MDPZ image obtained from DIC. This is shown in Figure 4.16 and Figure 4.17, with the white ellipse over each

image depicting the approximated size and shape of the CDM model's MDPZ. It was observed that due to disperse nature of the MDPZ captured with DIC, portions of it extended beyond the MDPZ region defined with the CDM model. However, the size and shape of the CDM model's MDPZ approximated well with that of the DIC generated MDPZ.

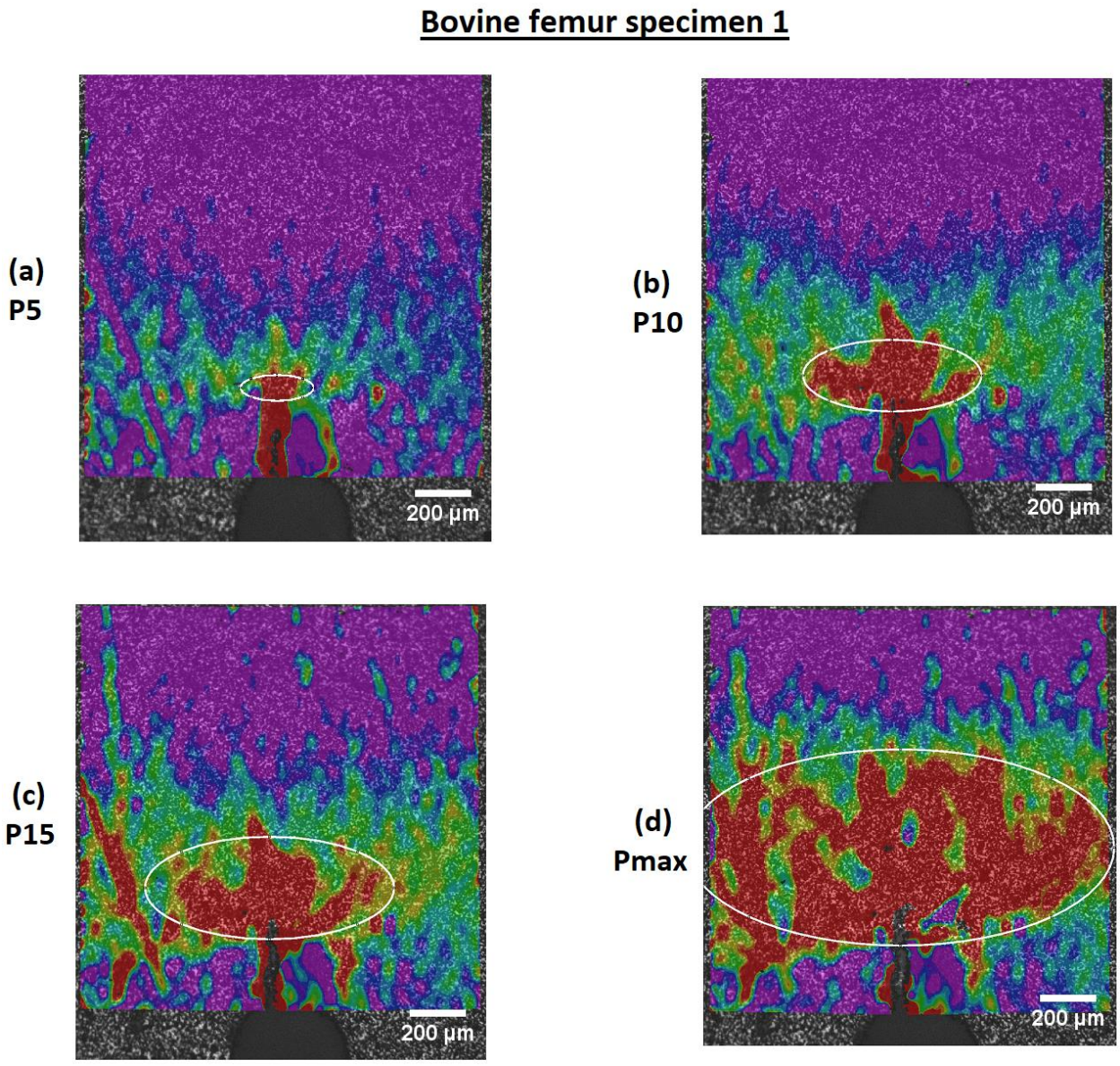

Figure 4.16: Comparison of CDM model and DIC measured microdamage process zones at different P values for bovine femur specimen 1. The white coloured ellipses imposed over each image represent the approximate size and shape of the CDM model's equivalent P value MDPZ. P5 means 5% secant stiffness loss, P10 means 10% secant stiffness loss, P15 means 15% secant stiffness loss and Pmax means maximum stiffness loss (stiffness is zero)

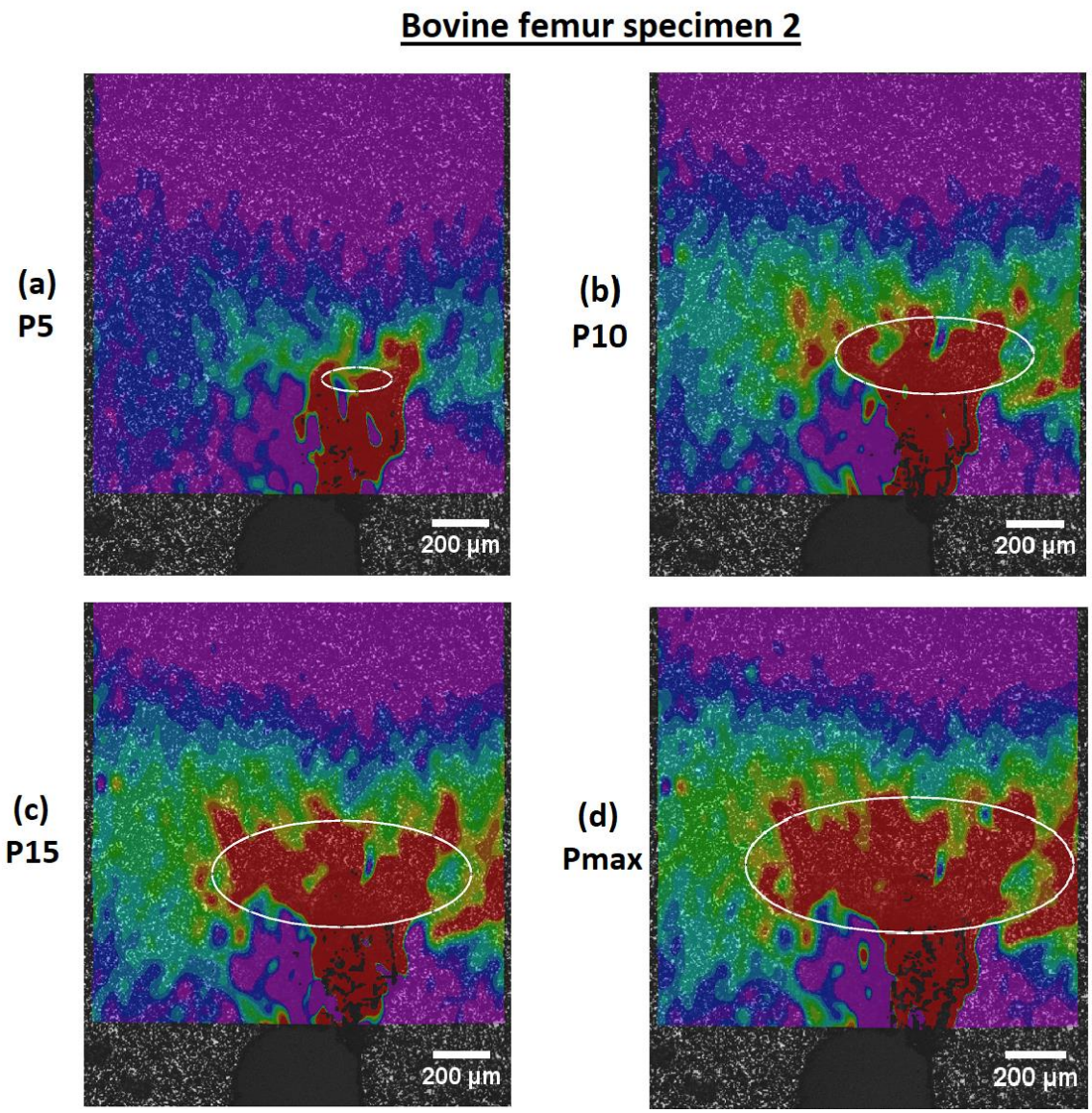

Figure 4.17: Comparison of CDM model and DIC measured microdamage process zones at different P values for bovine femur specimen 2. The white coloured ellipses imposed over each image represent the approximate size and shape of the CDM model's equivalent P value MDPZ. P5 means 5% secant stiffness loss, P10 means 10% secant stiffness loss, P15 means 15% secant stiffness loss and Pmax means maximum stiffness loss (stiffness is zero)

Additionally, to provide a quantitative comparison of the CDM modeled and DIC measured MDPZs, their respective sizes versus P values for the two bovine femur specimens were plotted and are presented in Figure 4.18 and Figure 4.19. Both the experimental and model MDPZ sizes increased with increasing P value following a second order polynomial function for both femur specimens. The CDM model was able to replicate the MDPZ size measured experimentally at lower P values but overestimated the size marginally at higher P values.

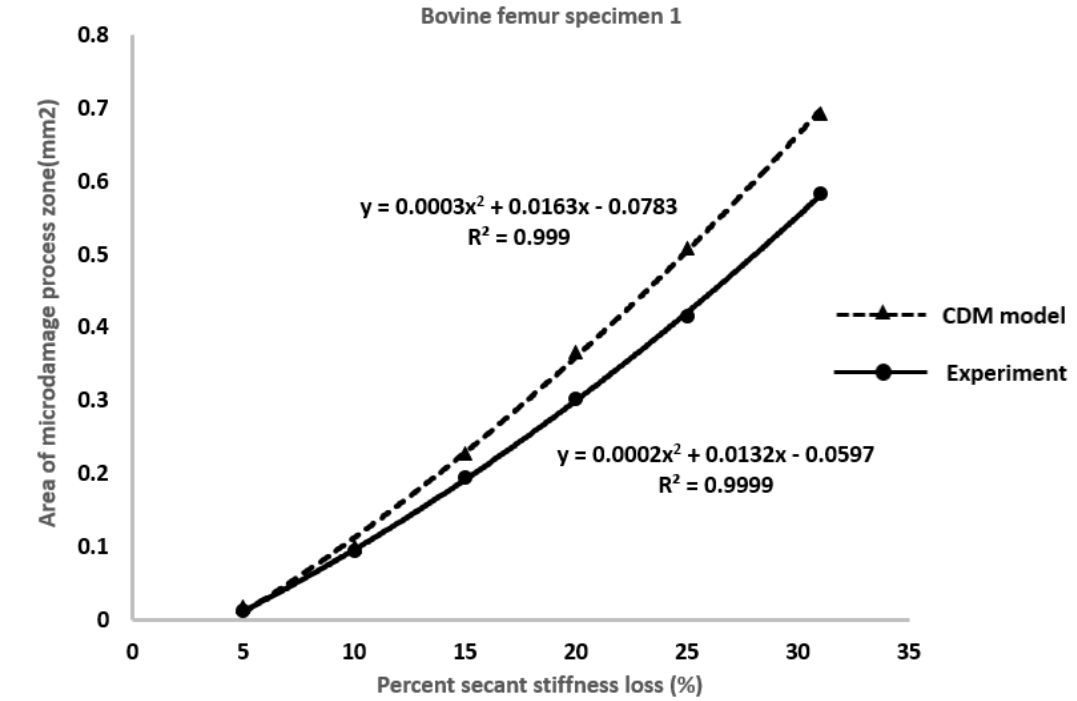

Figure 4.18: The area of the microdamage process zone versus the percent secant modulus loss for bovine femur specimen 1. Comparison between CDM model generated and experimentally measured curves.

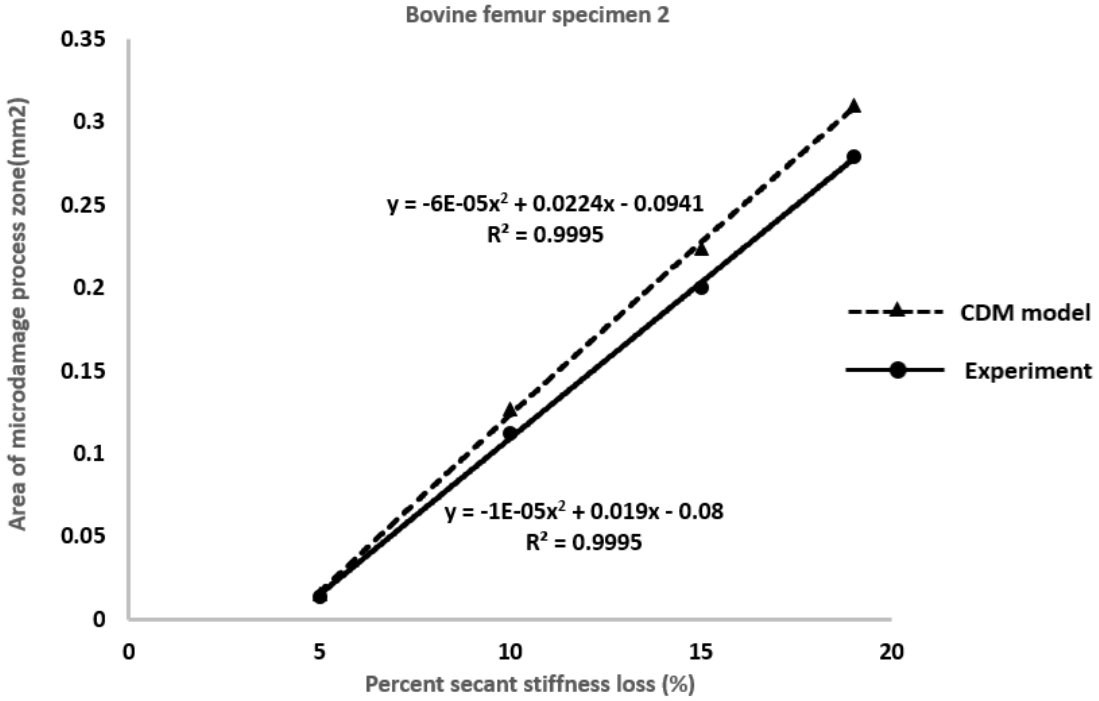

Figure 4.19: The area of the microdamage process zone versus the percent secant modulus loss for bovine femur specimen 2. Comparison between CDM model generated and experimentally measured curves.

For further validation of the model, the crack mouth opening displacement (CMOD) was compared between model and experiment. Figure 4.20 shows the comparison between the load versus CMOD curves from the CDM model and experiment for Femur Specimen 1. The two curves compare very well adding to the validity of the model. A similar curve is not shown for specimen 2 because the crack mouth region was poorly speckled (See Figure 4.21). The red circled area represents the region the crack mouth is found. However, due to poor speckling around that region, DIC consistently lost correlation and hence the CMOD could not be measured experimentally.

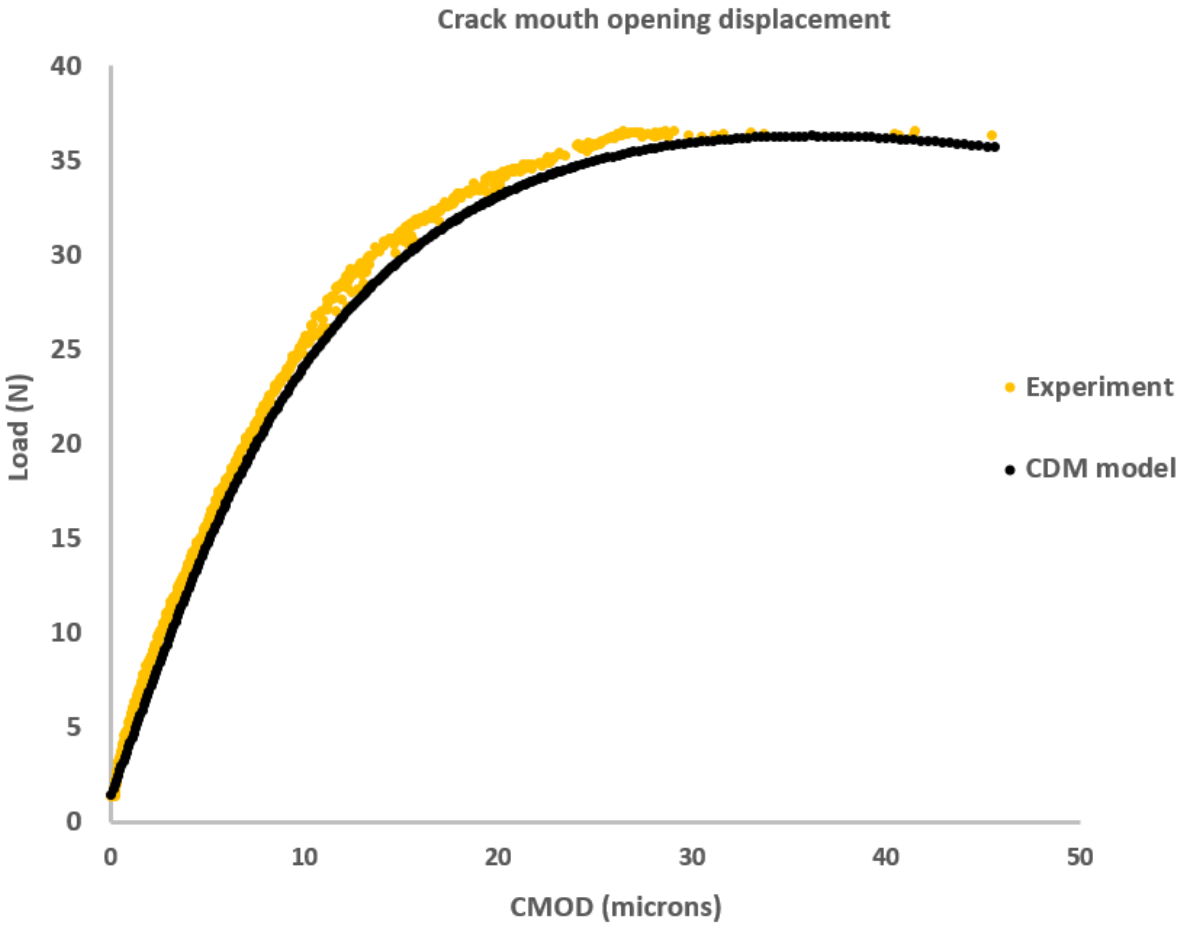

Figure 4.20: Comparison between the load versus CMOD curves generated from the CDM model and experimentally

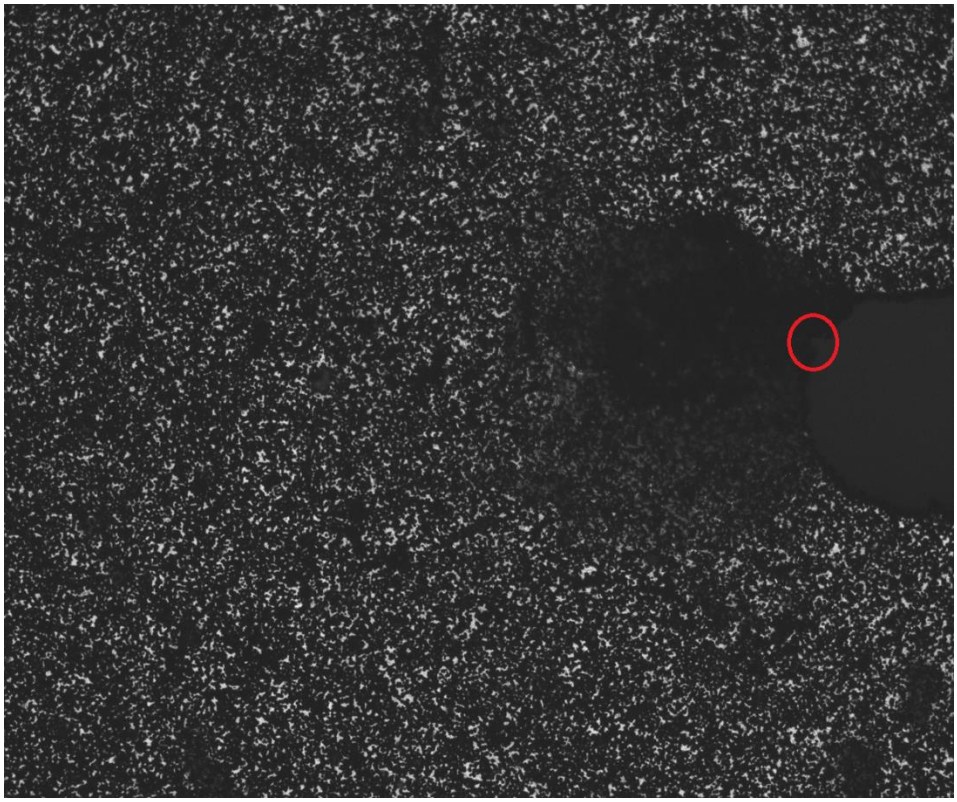

Figure 4.21: Speckle pattern for the region around the crack tip of bovine femur specimen 2

4.4 Comparison of CDM model with previous microdamage imaging work

To further ascertain the validity of the CDM model, its MDPZ was compared to the bovine tibia specimens' MDPZ's imaged in Willett et al. [78]. Figure 4.22 shows the MDPZ progression for the tibia specimen simulated with the CDM model. Consistent with results from the femur specimens, the MDPZ continuously increases in size up to fracture (Pmax). Figure 4.23 shows that the CDM model was able to replicate the experimentally determined load versus deflection curve for this specimen. Furthermore, the CDM model was able to closely replicate the height of the MDPZ measured experimentally, especially at lower P values, but overestimated the height at higher P value (Figure 4.24). This is consistent with the bovine femur specimens where the MDPZ area was overestimated at higher P values. Interestingly however, the CDM model overestimated the width of the MDPZ for all P values, increasingly overestimating the width with increase in percent secant stiffness loss as shown in Figure 4.25.

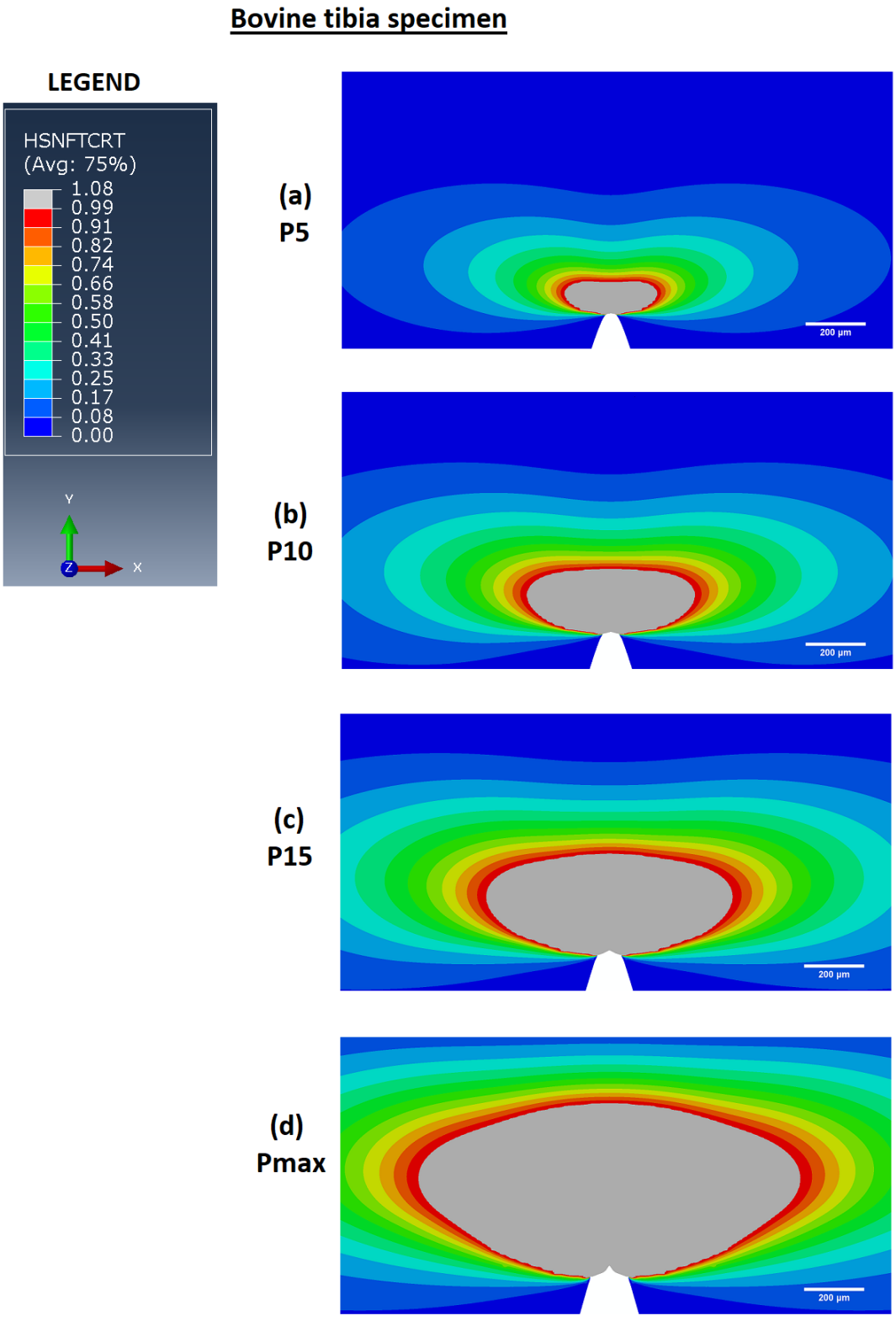

Figure 4.22: Microdamage process zone for a bovine tibia specimen from [78] *generated with the CDM model. P5 means 5% secant stiffness loss, P10 means 10% secant stiffness loss, P15 means 15% secant stiffness loss and Pmax means maximum stiffness loss (stiffness is zero)*

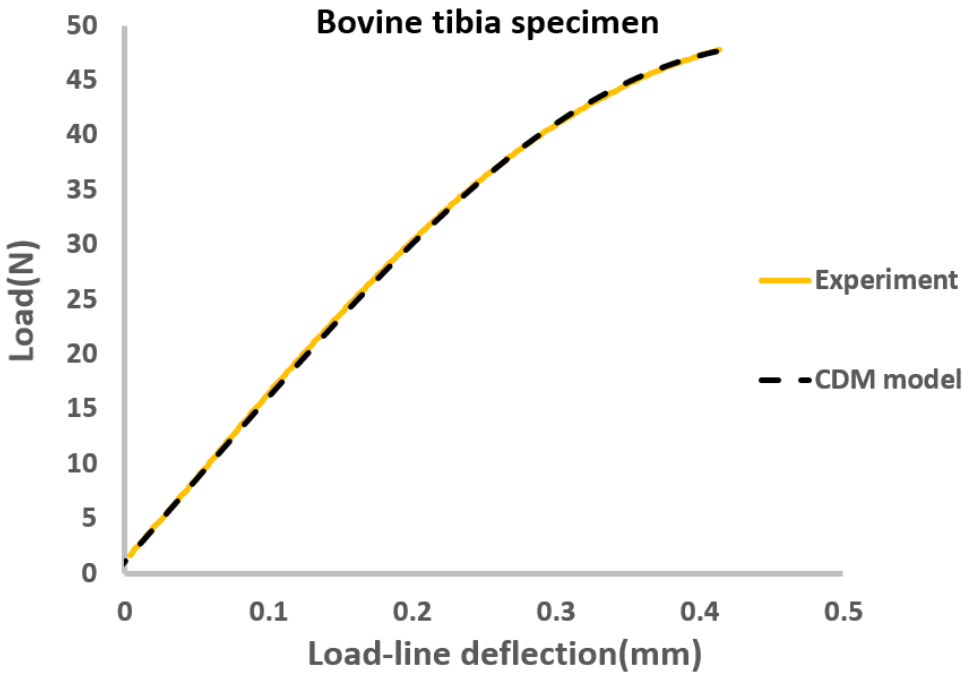

Figure 4.23: Closely matching load versus load-line deflection curves between the CDM model and that generated experimentally from a bovine tibia specimen in [78]

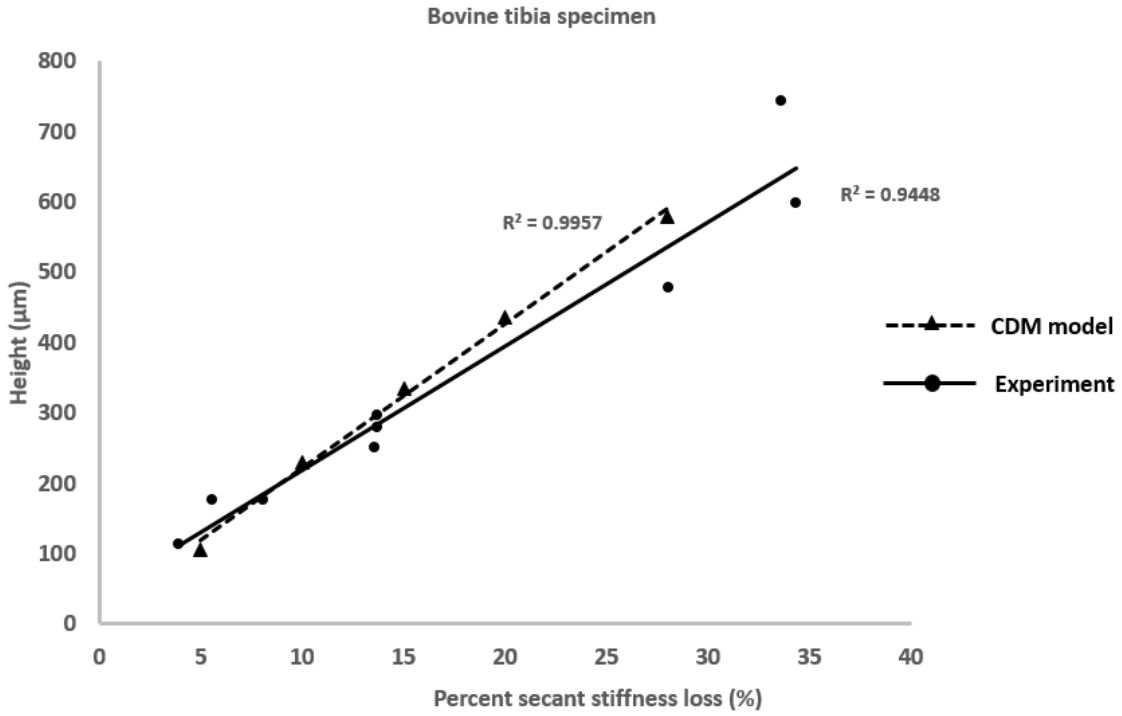

Figure 4.24: Comparison of the height versus P% curves between the CDM model and imaging experiment for bovine tibia specimen.

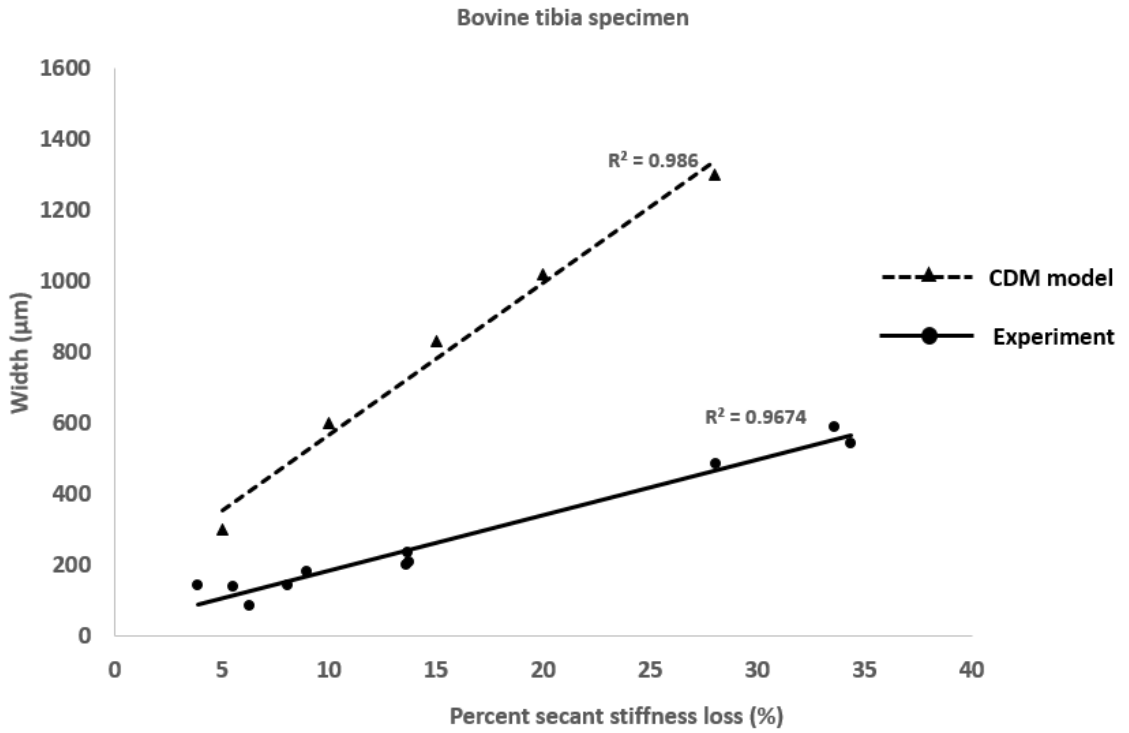

Figure 4.25: Comparison of the width versus P% curves between the CDM model and imaging experiment for bovine tibia specimen

4.5 Case study results

4.5.1 Longitudinal directed crack

Figure 4.26 presents the microdamage process zone (MDPZ) for a longitudinally directed crack generated by the CDM model. It was noticed that the MDPZ for the longitudinal directed crack was narrower compared to the transverse directed crack. This is consistent with the literature. The MDPZ at maximum load (Pmax) for the longitudinal directed crack was compared to the MDPZ at maximum load for the equivalent transverse directed crack and this is shown in Figure 4.27. Figure 4.27 clearly shows how, for the the transverse directed crack, the MDPZ extends out extensively before fracture occurs whiles the longitudinal directed crack has a much narrower MDPZ. The load versus load-line deflection curve of the longitudinal directed crack is presented in Figure 4.28, along with that of its equivalent transverse directed curve. The load versus deflection curve for the longitudinal directed crack is smaller and this is consistent with experimental findings. The maximum load for the longitudinal directed crack occurred at 0.3mm deflection while that for the transverse occurred at 0.42mm.

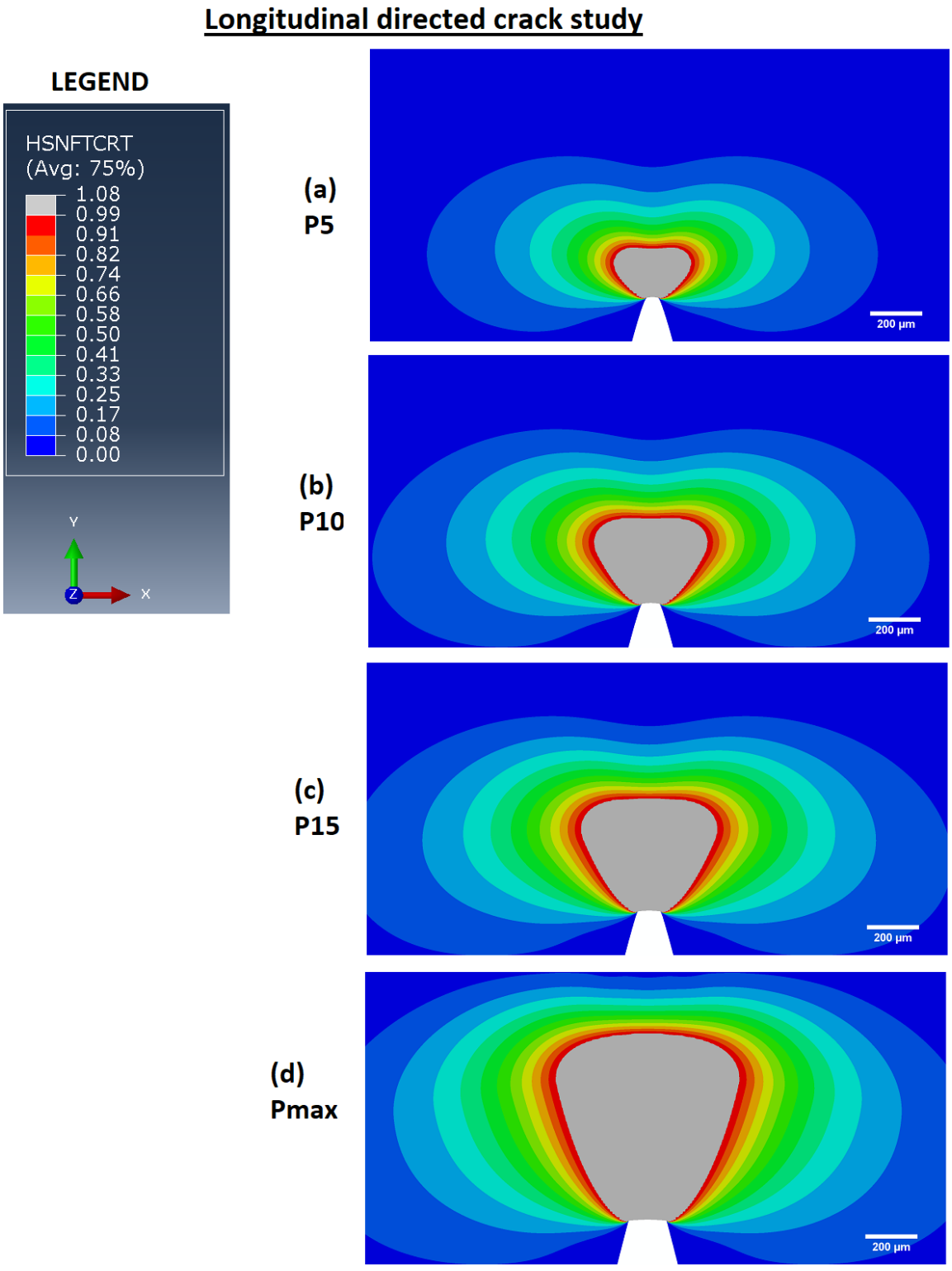

Figure 4.26: Microdamage process zone progression for a longitudinal directed crack simulated with the CDM model. P represents the percentage secant stiffness loss from its bending load vs deflection curve. P5 means 5% secant stiffness loss, P10 means 10% secant stiffness loss, P15 means 15% secant stiffness loss and Pmax means maximum stiffness loss (stiffness is zero)

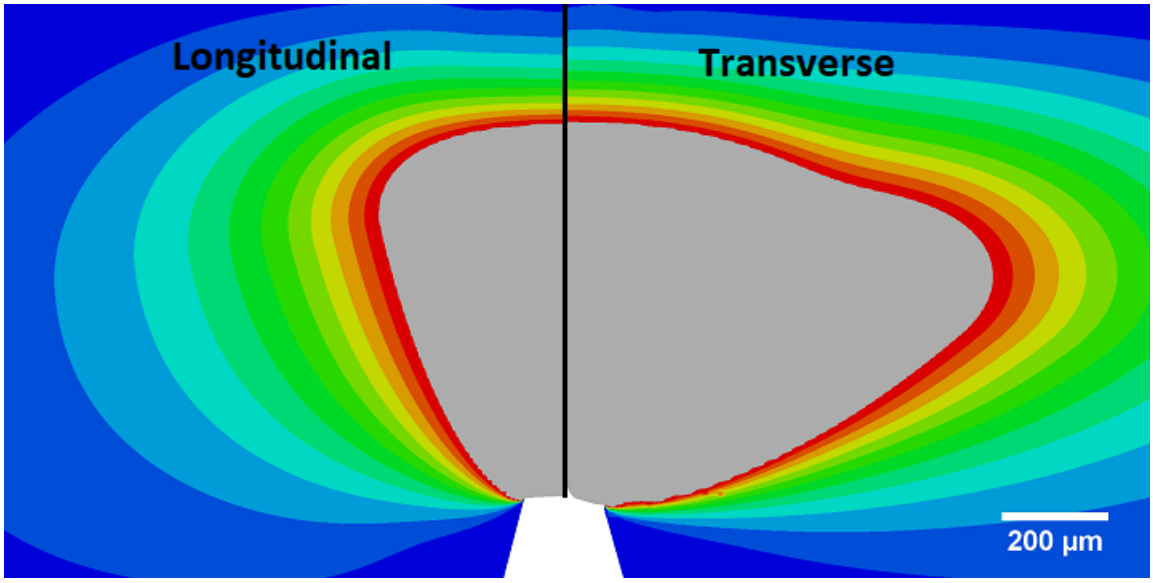

Figure 4.27: A comparison between the MDPZ for a longitudinal and transverse directed crack at their maximum loads (Pmax) both simulated with the CDM model. The left side of the figure represents the MDPZ for the longitudinal directed crack whiles the right side, the MDPZ for the transverse directed crack.

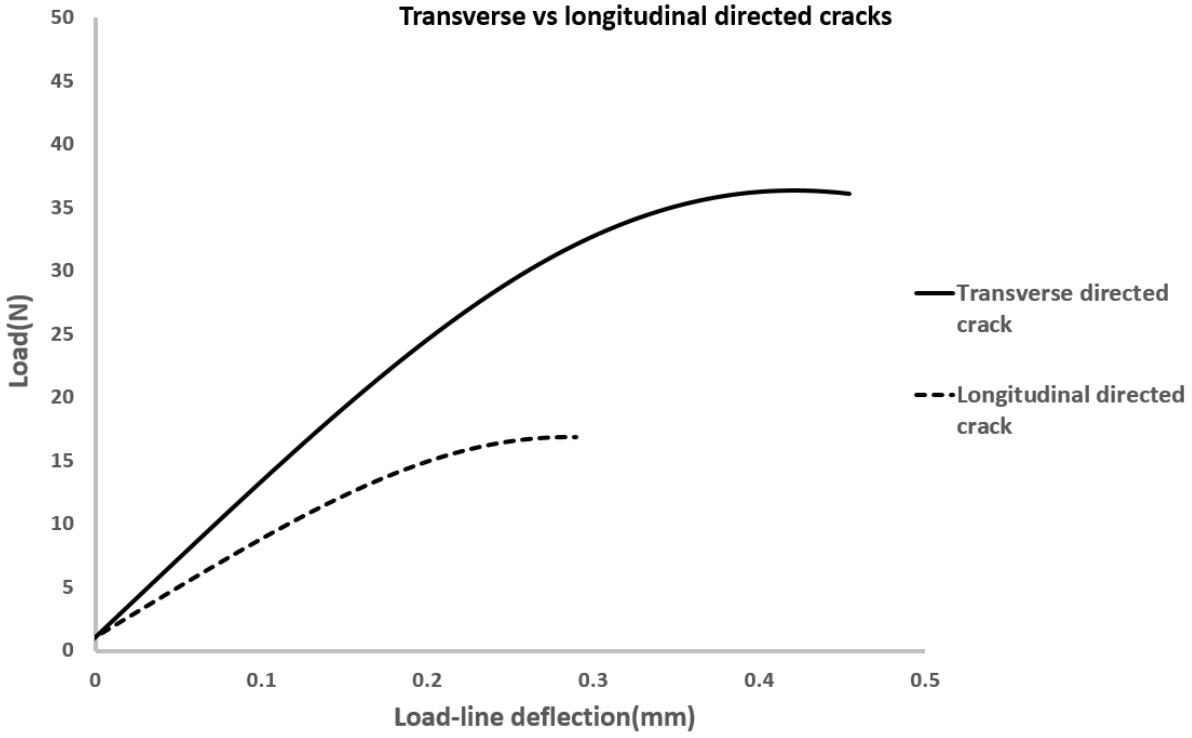

Figure 4.28: Load versus load-line deflection curves for a transverse and longitudinal directed crack generated with the CDM model for the same specimen

4.5.2 Irradiated bovine tibia study

The microdamage process zone progression as a function of its percent secant bending stiffness loss (P%) of an irradiated bovine tibia specimen is presented in Figure 4.29. Consistent with the non-irradiated bovine tibia specimen simulation, the MDPZ continually increased up to Pmax. However, just like the longitudinal directed crack, the irradiated bone had a narrower MDPZ as compared to the non-irradiated transverse directed crack specimen. Figure 4.30 compares the MDPZ for the irradiated and non-irradiated specimen at their respective Pmax (maximum bending loads). This clearly shows the wider MDPZ formed in the case of the non-irradiated. The size of the MDPZ for the irradiated specimen was roughly 40% smaller the size for the non-irradiated specimen. The load versus load-line deflection curves from the experimental data and the CDM model are plotted in Figure 4.31 and shown to closely match. Also, the load deflection curve for the non-irradiated bone specimen simulated with the CDM model is presented. This load deflection curve is seen to be greater than the irradiated ones, signifying greater strength and energy dissipation during fracture.

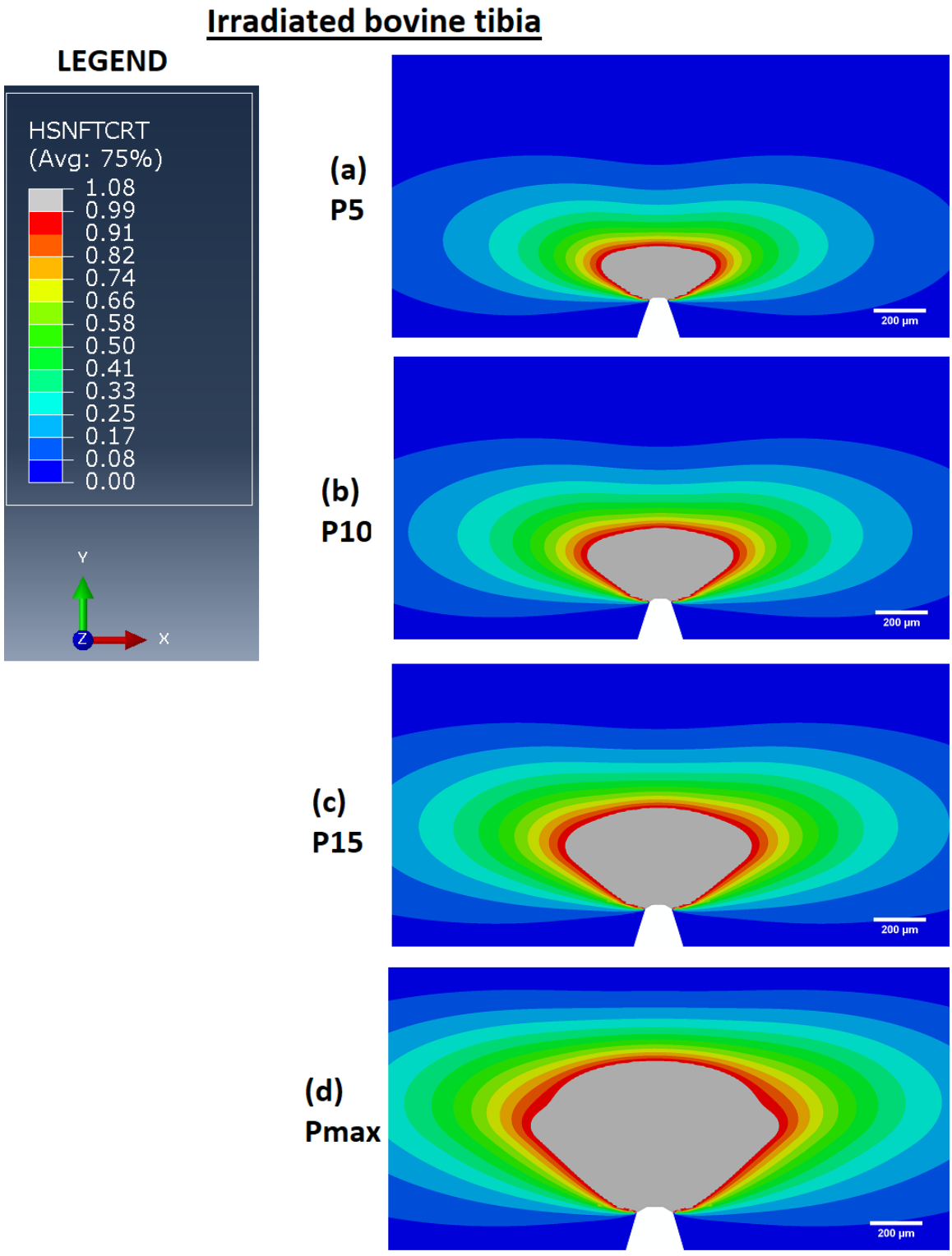

Figure 4.29: Microdamage process zone progression for an irradiated bovine tibia specimen simulated with the CDM model. P represents the percentage secant stiffness loss from its bending load vs deflection curve. P5 means 5% secant stiffness loss, P10 means 10% secant stiffness loss, P15 means 15% secant stiffness loss and Pmax means maximum stiffness loss (stiffness is zero)

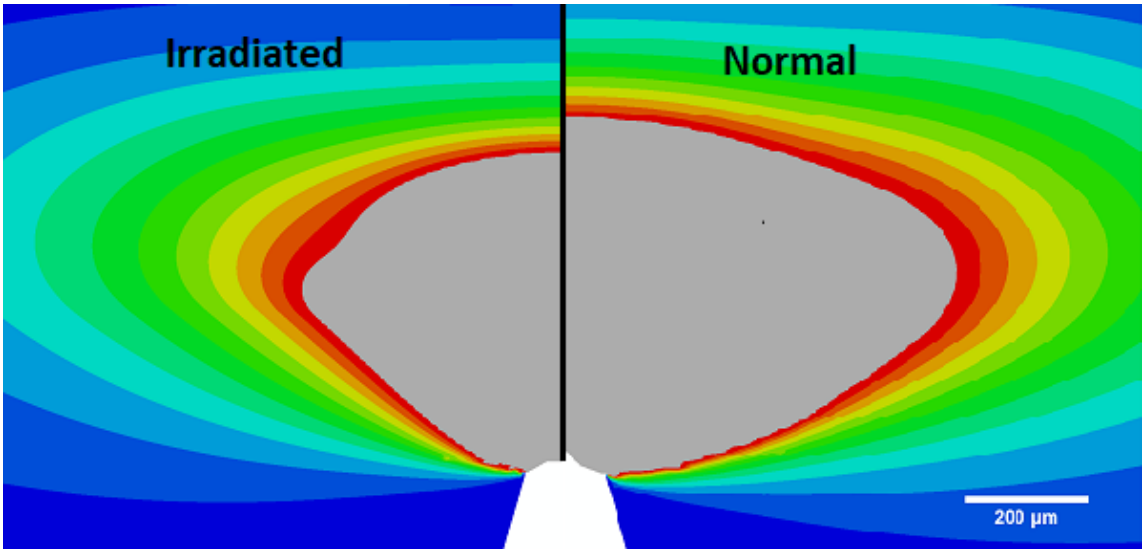

Figure 4.30: A comparison between the MDPZ for an irradiated and non-irradiated specimen at their maximum loads (Pmax) both simulated with the CDM model. The left side of the figure represents the MDPZ for the irradiated specimen whiles the right side, the MDPZ for the non-irradiated. The crack in both specimens were directed transversely.

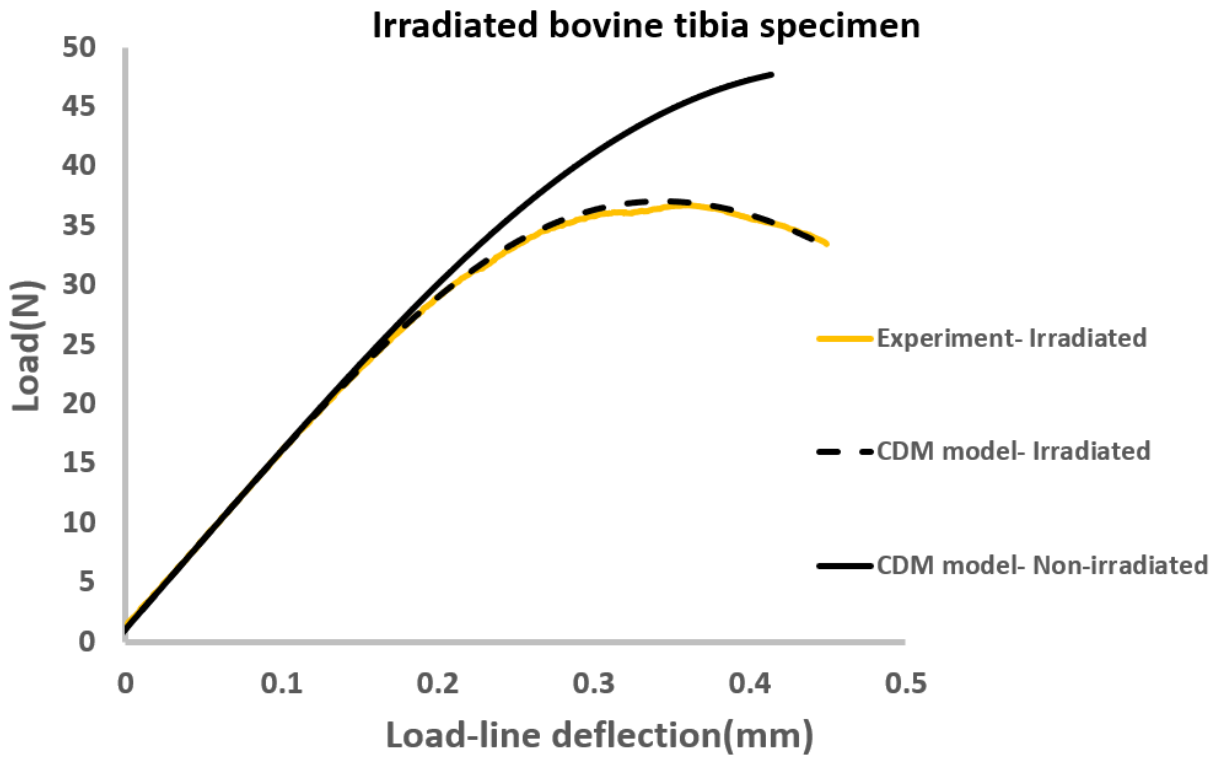

Figure 4.31: Load versus load-line deflection curves of experimental-irradiated, CDM mode-non-irradiated and CDM model-irradiated

Chapter 5

Discussions

5.1 Experimental and analytical comparisons

Results from the CDM model validated against experimental data show that a continuum damage mechanics (CDM) provides a relatively simple but adequate and reliable means of modelling the MDPZ for cortical bone. CDM has been previously used in modelling fracture in a variety of engineered composites and concrete-like materials [122,123]. These materials also undergo a similar microcracking phenomena as a damage mechanism [79]. However, to the best of my knowledge, this is the first time a CDM-FE model has been developed to simulate the MDPZ formed for cortical bone during its fracture process.

In the current study, both the CDM model simulations and experiments carried out on the bovine femur specimens undergoing transverse directed fracture showed extensive formation of the MDPZ, which is consistent with previous experimental findings [55,78,121,124]. This confirms the MDPZ as an important toughening mechanism in bone fracture, as the formation of the MDPZ dissipates energy that would otherwise be available for driving crack growth and blunts the crack tip stresses [125]. This is further evidence that the ability of cortical bone to form this extensive diffuse MDPZ impacts its fracture toughness. Therefore, any physiological or non-physiological factors that may impede the ability of bone to form the MDPZ may affect the bone's fracture toughness.

In validating the CDM model, by comparing the area of the MDPZ between model and experiments (See Figure 4.18 and Figure 4.19), it was interestingly noticed that while at lower P values, there was a good match, there was a slight overestimation by the CDM model at higher P values. This may be because at higher P values (15% and higher), extrinsic toughening mechanisms such as crack bridging would have been engaged. These toughening mechanisms only come into play when the crack begins to propagate [15,35,45]. These extrinsic toughening mechanisms also dissipate energy. However, our CDM model assigns all energy dissipation to MDPZ formation in order to match the load versus deflection curves. This means a slightly larger than expected MDPZ will be formed as more energy is fed into forming the MDPZ than perhaps otherwise should be. Furthermore, it is worth noting that the CDM model increasingly

overestimates the MDPZ size with increasing P value. This is consistent across the bovine femur specimens and also the bovine tibia specimen (See Figure 4.24 and Figure 4.25) from Willett et al. [78]. Another explanation for the disparity may be because of how the areas were measured. For the CDM model, the region of microdamage formation was continuous and homogenous hence the entire area was measured, whereas experimentally, the microdamage formation was heterogenous and only the dispersed regions of microdamage formation was measured. The continuous nature of the MDPZ in the CDM model instead of the more realistic diffuse nature may account for the overestimation of the MDPZ size in the CDM model. In spite of this, the CDM model still replicates the experimental MDPZ quite well, except for the bovine tibia specimen data from Willett et al. [78].

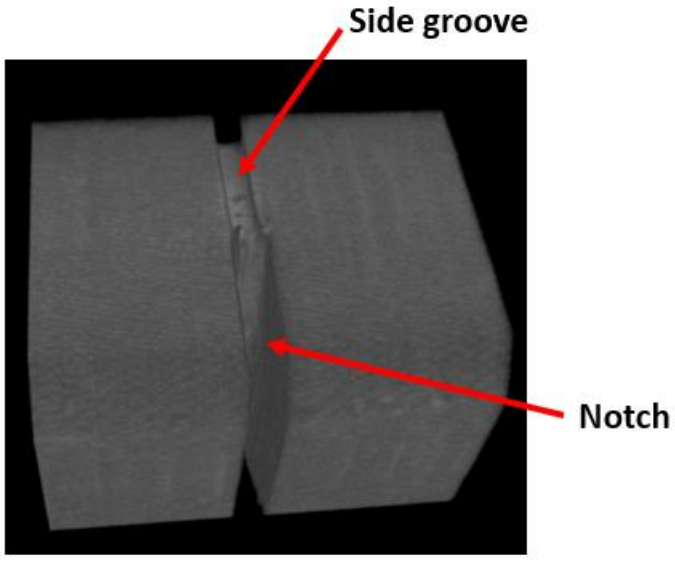

Figure 5.1: A sectioned portion of a SENB tibia specimen from [78] *showing side groove ahead of the sharpened notch. Reprinted from Willett et al, 2017* [78]

Considering, the tibia specimen from Willett et al. [78], though the overestimation of the MDPZ increases with increase in P value in terms of both the width and height, the width is considerably overestimated for all P values. It is hypothesized that this may be due to the existence of side grooves for the experimental tibia specimens. The SENB tibia specimens had side grooves 300µm wide and 400µm deep machined into the region ahead of their sharpened notch (Figure 5.1). Side grooves have been established to create a uniform triaxial state of stress along the crack front [125]. This concept is explained below. Due to the sharpened notch (micro and macro-notch), very high

stresses are imposed normal to the crack front plane (in the y direction in Figure 5.2) when loaded in a SENB test. This high stress, due to Poisson effect, would drive contractions in the other two directions (x and z directions in Figure 5.2). However, the surrounding bone material resists this contraction creating a triaxial state of stress in the region just ahead of the crack tip. Putting it another way, normal stresses are induced in the other two directions as a counter-balance to the inability to contract. This is representative of a plane strain condition. However, moving across the crack front (z direction in Figure 5.2), the induced stress is almost zero near the surface of the specimen and zero at the free surface [125] . This is shown in Figure 5.3 where zero on the "distance along z" axis occurs at the mid-point of the crack front. Therefore, on the surface of the specimen, the stress state is more representative of a plane stress formulation as no triaxial stress state is induced on the surface. By creating side grooves, the portion of the material at or closer to a plane stress formulation is removed and only a plane strain condition is imposed ahead of the crack front.

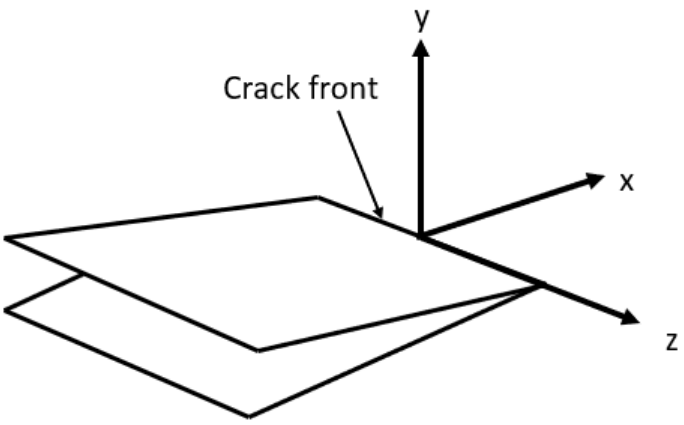

Figure 5.2: An illustration of the crack front showing the different axes from the mid-point

More so, it has been established in ductile metals that the size of their plastic zone (analogous to MDPZ) differs under the two loading configurations [125]. Figure 5.4 shows the estimated plastic zones for plane strain and plane stress loading configurations with the plane strain formulation having a smaller plastic zone. These plastic zones were formulated from modified forms of the linear elastic fracture mechanics (LEFM) approaches [31,125]. Though FE approaches have also been used to show slightly different plastic zones, the LEFM based ones are considered reasonable estimates [125]. The smaller plastic zone in the plane strain configuration is a result of the high

triaxial state of stress impeding plastic flow [125]. The creation of the plastic zone in ductile metals is due to plasticity mechanisms which is different from the mechanism of microdamage formation.

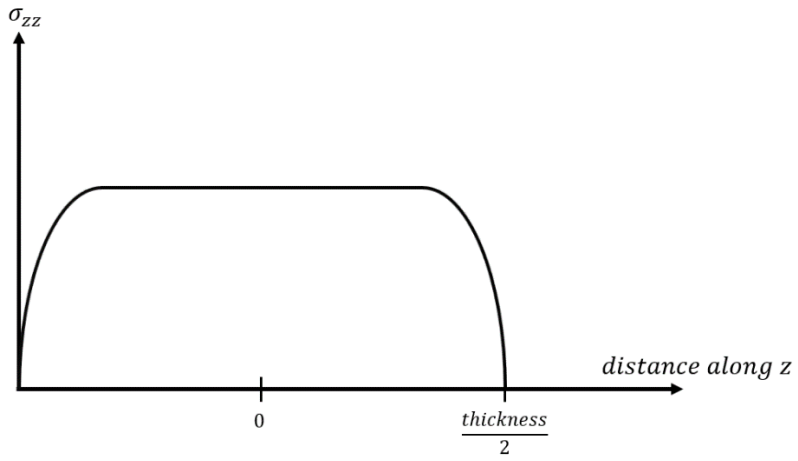

Figure 5.3: Transverse stress profile induced in the through thickness region near the crack front

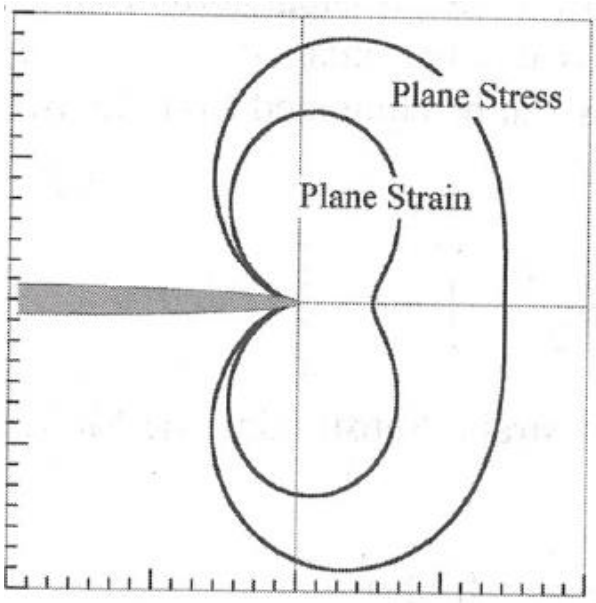

Figure 5.4: The different plastic zone formed for plane strain and plane stress loading configuration. Reprinted from Anderson, 2005 [125]

Though this principle of plane strain and plane stress effect on plastic zone size has been established for other materials such as ductile metals, it has not been well established for cortical bone. The shape and size of the MDPZ imaged in Willett et al. [78] is different from the characteristic plastic zone shape and size for ductile materials under plane strain formulation but, rather closely resembles the plane stress process zone shape for nacre [126]. However, the model

seems to suggest a larger MDPZ forms in cortical bone under a plane stress loading configuration. This claim is further supported by the DIC experiment in which MDPZ is mapped using only surface strains from surface deformations. The specimens in the DIC experiment did not have side grooves. Therefore, there is a possibility the surface might be under plane stress. This suggests a need to investigate the potential change in MDPZ shape and size for cortical bone under plane strain and plane stress formulations. This is also necessary as this directly impacts fracture toughness testing of bone. Standard fracture toughness tests are set up for specimens to be tested under a plane strain formulation, because it is the most critical and conservative loading configuration [125]. To ensure the specimen is under plane strain formulation, a thicker specimen is used to make sure the high triaxial stress state dominates the low triaxial stress states near the surfaces or edges [125]. Studies have been done to establish a minimum thickness criterion for standard materials in fracture toughness test [117]. An investigation into MDPZ shape and size under plane stress and strain formulations with cortical bone might help establish a more suitable criteria for defining minimum thickness specific to fracture toughness testing of cortical bone.

Moving on to the case studies, the longitudinal directed crack was seen to form a smaller MDPZ compared to the transverse directed crack. This result is consistent with literature on the mechanisms of cortical bone fracture in these two directions [35,40,77]. Akkus et al. [77], using histology, studied the formation of MDPZ in both longitudinal and transverse directions. Their study, though not stated explicitly, showed a smaller MDPZ for the longitudinal directed crack compared to the transverse directed crack. Other studies have shown this may be due to the presence of the cement lines [33,39]. These cement lines are aligned with the long axis of the bone and highly mineralised. Therefore, during longitudinal directed fracture, the diffuse microcracks accumulate or concentrate in the cement lines. This accumulation therefore prevents the spreading out of the MDPZ as occurs in the transverse direction. The CDM model was able to replicate the expected narrower MDPZ for the longitudinal directed crack (Figure 4.25) which speaks to the model's validity. The smaller MDPZ leads to a smaller dissipation of energy and explains the smaller load versus deflection curve obtained in comparison with the transverse directed crack. It has been shown that the crack growth driving force in the transverse direction can be as much as five times higher than in the longitudinal direction [40].

Burton et al. [121] showed the size of the MDPZ formed during transverse fracture of an irradiated bovine cortical bone was almost 50% smaller than its non-irradiated equivalent. A similar staining technique to the one carried out in Willett et al. [78] was used in the quantification of the MDPZ size in Burton et al's study [121]. They however reported that not all the diffuse microcracking was stained in their study. The CDM model in this study produced a 40% reduction in the formation of the MDPZ for the irradiated specimen as compared to the non-irradiated specimen. Though the percentages are different they compare well considering the fact that, not all the microcracks were stained in their experimental study

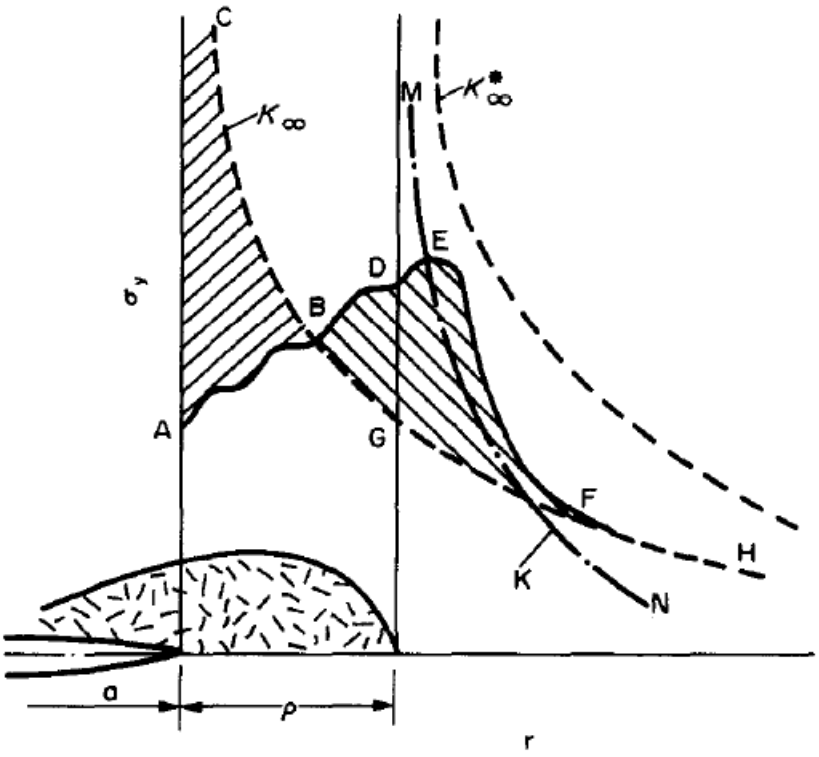

Figure 5.5: Stress profile in the normal direction to the crack tip showing stress redistribution ahead of a process zone. CBGH shows the stress profile that should exist in the absence of the process zone (linear elastic case). ABDEFH shows the redistributed stress as a result of the process zone formed ahead of the crack tip. Area ABC=Area BEF. Reprinted from Zhonghua and Yong,1993 [62]

Zhonghua and Yong in 1993 [62] proposed an analytical cohesion model that predicts the microcrack (microdamage) process zone for microcracking materials. This model was based on modifying LEFM approaches to account for the formation of the process zone ahead of the crack tip. Using this model, they defined the stress distribution profile versus the distance ahead of the

crack tip (r) in the same plane. This is shown as the ABDEFH solid line in Figure 5.5. They argued that the presence of the process zone causes a re-distribution of stresses ahead of the crack tip. In LEFM, the stress distribution profile would follow the CBGH line. The formation of microcracking process zone induces cohesive stresses that pushes the higher stress distribution (area ABC), that would have existed at the crack tip in the LEFM approach, ahead to region (area BEF) close to the edge of the microcracking process zone, and thus re-distributing the stress.

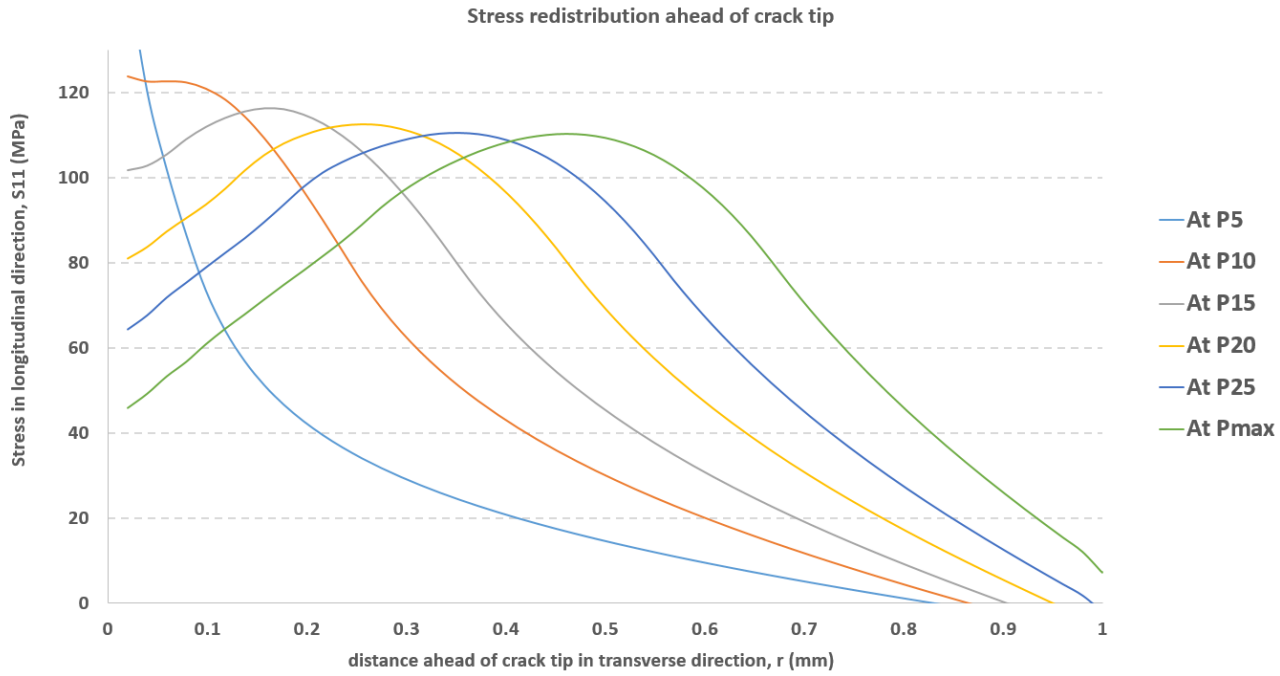

Figure 5.6: Stress in the longitudinal direction versus distance from crack tip in the transverse direction.

Yang and Cox [127], using a cohesive zone law, characterised human bone fracture and also found this stress redistribution ahead of a crack tip. They implemented this law in a finite element software and validated their cohesive law against experimental data. Interestingly, the CDM model also exhibits this stress re-distribution behaviour. Figure 5.6 shows plots of the stress in the longitudinal direction (S11) versus the distance from the crack tip in the transverse direction at different P values during a CDM simulation of a transverse fracture. The figure shows that as the specimen is continually loaded and losses secant stiffness, the peak S11 stress shifts further in front of the original crack tip with the continuous formation of the process zone. Figure 5.7 shows a similar plot to Figure 5.6 but the y-axis reflects the strain in the longitudinal direction (E11).

Using this strain, the height of the MDPZ can be estimated. In this case, any region with strain above 0.0044 in the specimen is expected to be undergoing microdamage formation. Matching the two figures, it is noticed that the MDPZ height matches closely to the location of the peak S11 stress at different P values. This provides an interesting concept into a mechanistic understanding of the cortical bone fracture process. It also adds credence to the concept that failure in bone is strain controlled [41].

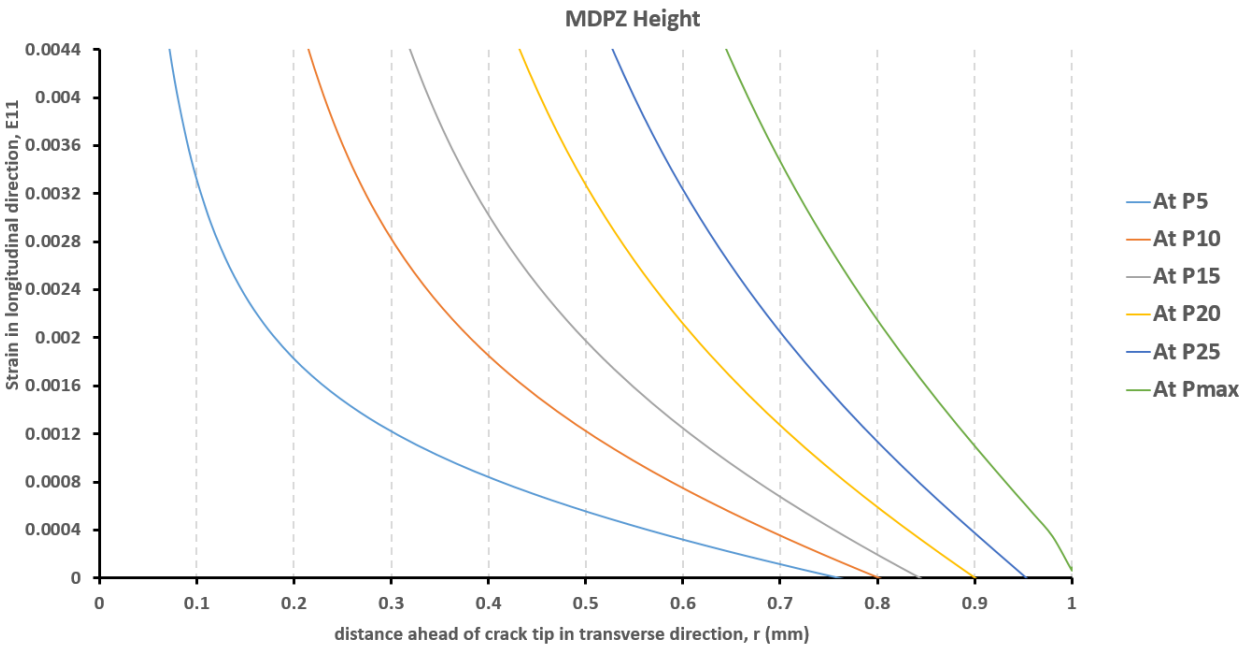

Figure 5.7: A plot of strain in the longitudinal direction versus distance from crack tip in the transverse direction showing the estimated MDPZ height with increasing secant stiffness modulus loss (P).

5.2 Sensitivity of model to viscoelastic/plastic effects

In Figure 4.12 and Figure 4.13, the importance of incorporating viscoelastic/plastic effects in the CDM model was shown. This effect slows down microdamage formation directly ahead of the crack tip and allows the MDPZ to expand laterally. Viscosity effects have been shown to be key to the formation of extensive process zone in naturally occurring composites, such as nacre [128]. Due to viscoelastic/plastic effects, a high strain concentration at an existing flaw/defect leads to a higher rate of deformation around the defect compared to the rest of the material. A higher rate of

deformation means a progressively higher value of stress is required to cause further deformation. In other words, there is strain rate hardening around the defect. This strain rate hardening effect leads to further deformations spreading to other areas of the material requiring lower stresses to deform. This spreading of the deformation causes the formation of a broader process zone [128]. Due to viscoelastic/plastic effects, a high strain concentration at an existing flaw/defect leads to a higher rate of deformation around the defect compared to the rest of the material. A higher rate of deformation means a progressively higher value of stress is required to cause further deformation. In other words, there is strain rate hardening around the defect. This strain rate hardening effect leads to further deformations spreading to other areas of the material requiring lower stresses to deform. This spreading of the deformation causes the formation of a broader process zone [128]. As shown in Figure 4.2 and Figure 4.4, the implementation of viscous regularisation scheme in the CDM model allowed the elements to exceed their Hashin strengths and failure strains and mimicking the strain rate hardening effect. This strain rate hardening effect, leading to a larger process zone, has been showed to amplify the toughness in these naturally occurring composites [129]. This explains the great disparity between the load versus deflection curves for the CDM model with lower and higher viscous regularisation (See Figure 4.11). The viscoelastic/plastic property of cortical bone is mainly provided by the organic phase, mostly made up of collagen [130,131]. These collagen molecules have been found to withstand great deformations [38,39,131]. Although not established, these collagen molecules and their interfaces with the mineral platelets may be the main contributors to cortical bone's strain rate hardening effect. It has been established that the organic phase is vital to bone's fracture toughness especially in the transverse direction [35,47]. In longitudinal fracture, the cement line which is highly mineralised provides the pathway for crack propagation. An extensive MPDZ may not be formed in the longitudinal directed fracture because there is little organic phase to engage the strain hardening effect. Further, in irradiating bone, the collagen connectivity has been found to become degraded [121]. This decrease in collagen connectivity has been suggested to be as a result of collagen peptide chains fragmentation [121,132]. Therefore, the formation of a smaller MDPZ for the irradiated bone as compared to the non-irradiated bone may be due to the damaged collagen molecules not being able to engage in as much strain rate hardening. The sensitivity of the CDM model to viscoelastic/plastic effects adds credence to the importance of collagen to bones' fracture toughness and suggest a strain rate hardening mechanism in cortical bone fracture. More detailed

investigations into the mechanical competence as well as the deformation of bone collagen in cortical bone fracture may provide insights that will allow a better mechanistic understanding of the fracture process.

5.3 Potential applications

The CDM model provides a simpler means of investigation into the fracture process of cortical bone, especially in terms of its MDPZ formation as compared to the experimental staining technique used to determine the MDPZ in previous studies. As already shown, the CDM model was used in determining the MDPZ for a longitudinally directed crack and for a transversely directed crack in an irradiated specimen. This offered meaningful insight into how the MDPZ formation of cortical bone affects its fracture toughness. With further development of the CDM model, it has potential application in investigating the effects of aging and bone damaging diseases on the fracture toughness of bone. It is well established that aging and bone damaging diseases cause a loss in fracture toughness. However, the exact mechanism by which this happens is still debated. The CDM model offers a straightforward means to test hypotheses to provide meaningful insights which can then be used to inform experimental designs for validation of these hypotheses.

The CDM model when further developed, may have potential application in assessing how implantation of devices such as screws, plates, nails and wires alter the fracture toughness of cortical bone in relation to its ability to form a MDPZ around the local defects they cause. This assessment can also be extended to different sized physiological stress concentrators that naturally occur in cortical bone. Additionally, the CDM model provides a means of mapping local stress and strain fields around defects. Something that is difficult to accomplish experimentally. This also gives us a holistic view of how different defects re-distribute their local stresses and strains. These are just a few of the potential applications of the CDM model.

5.4 Limitations of the CDM model

Although, the CDM model has been shown to work well, it still has three significant limitations. First, the model is only two dimensional and a plane stress formulation was used in the analysis of the model as the Hashin criteria function in ABAQUS only works with plane stress elements. As earlier discussed in section 5.1, the presence of a crack creates a high triaxial state of stress within a material and a low triaxial state of stress at the edges or surfaces of the material. This creates a

plane stress condition on the surfaces and a plane strain condition through the thickness of the material along the crack front. For ductile metals, it has been established that a plane stress condition produces a larger plastic zone ahead of the crack as compared to the plane strain condition (See Figure 5.4). That means the surfaces of ductile materials will form a larger plastic zone ahead of a crack front, but this plastic zone reduces in size through the thickness along the crack front. This phenomenon has however not been established in cortical bone. However, if such a phenomenon exists in cortical bone then the CDM model only accurately predicts the MDPZ at the surface of the specimen but not the MDPZ through the thickness along the crack front in the specimen. This limitation becomes especially significant if the CDM model is further developed to study crack propagation in cortical bone fracture.

Secondly, the model does not incorporate the microstructural features of cortical bone. Though the CDM model can closely match the size of the MDPZ in experiments, the absence of microstructural features causes it to deviate a bit from the shape in experiments. As observed from the DIC analysis results, the microstructure causes the MDPZ to be dispersed and not continuous as obtained with the CDM model. Also, it is hypothesized that the absence of the microstructural features may play a role in the deviation of MDPZ size at higher P values for the CDM model

Thirdly, the current formulation does not include any explicit form of plasticity. When cortical bone is unloaded after been loaded beyond its “yield” point, the strain does not return to zero in its stress-strain curve. This indicates the presence of plasticity in the damage process of cortical bone [115]. However, the importance of this plasticity to the formation of the MDPZ is not fully established.

Chapter 6

Conclusion

6.1 Conclusion

A better mechanistic understanding of fracture toughening mechanisms in cortical bone fracture may provide essential clues on how fracture toughness loss with aging and bone damaging diseases occurs. One of such vital toughening mechanisms is the formation of a microdamage process zone. Using a continuum damage mechanics (CDM) approach, a two-dimensional model was built to simulate MDPZ formation in the finite element software, ABAQUS. From this study, it can be mainly concluded that:

1. CDM provides a reliable means of modelling the microdamage process zone that forms during cortical bone fracture as was hypothesized,
2. The CDM model was able to replicate the size of the MDPZ observed experimentally as well as the experimental load-deflection curves,
3. The CDM model has potential to become a tool for investigations into the effect, changes in bone quality may have on its MDPZ formation ability.

Further, to accurately replicate the MDPZ size and shape as well as the load deflection curves from experiments, the model was found to be sensitive to elastic moduli, Hashin failure strengths, fracture energies (defined based on strengths, failure strains and mesh size) and the viscous regularisation parameters. The viscous regularisation parameter was used to introduce viscoelastic/plastic effects into the model, and these effects were vital to the spreading of the MDPZ formation over a broad area. This suggest the existence of a strain rate hardening mechanism in cortical bone fracture. This concept has been established for other naturally occurring composites, such as nacre [128].

Furthermore, the model confirmed there is stress re-distribution ahead of the crack tip as the MDPZ grows adding credence to the concept of strain -controlled failure in cortical bone. The CDM model alludes to a specimen thickness dependence of the MDPZ size and shape but this must be confirmed through further investigations and experimentation.

With further development and additional validation of the CDM model, it can become a useful tool in studies investigating the impact of bone quality changes on the fracture toughness of bone, especially in terms of its ability to form the MDPZ, and for predicting bone robustness in various applications

6.2 Future works

The CDM showed potential in gaining insights into how fracture toughness in terms of the MDPZ is affected by bone quality changes. However, the CDM model requires further development and validation to achieve higher fidelity and reliability for potential applications. Some of the next steps for a higher fidelity model are listed below:

1. The development of a three-dimensional CDM model will better replicate MDPZ formation. This will be essential if indeed the MDPZ size and shape is sensitive to specimen size. It will also provide a means to gain insight into how MDPZ formation may vary through the thickness of cortical bone during fracture.
2. The incorporation of microstructural features of cortical bone into the model will also be an essential addition. The microstructure of bone has been found to also delay crack growth by engaging other extrinsic toughening mechanisms, such as crack deflection and crack bridging [15,35]. Due to the lack of microstructure in the current CDM model, MDPZ is the only occurring extrinsic toughening mechanism and as stated earlier may account for the deviation of the CDM model MDPZ size from experiments at higher P values. The addition of microstructure may therefore enable a more accurate representation of the MDPZ at higher P values.
3. A viscous regularisation scheme in ABAQUS was implemented to introduce viscoelastic/plastic effects into the model. A more explicit incorporation of these viscoelastic/plastic effects will lead to a higher fidelity model. This will involve incorporating experimental creep data directly into the model.
4. The incorporation of viscoelastic/plastic effects into the model can be additionally validated by comparing the enhanced failure strains as a result of these effects (the strain at which the stress became zero increased from 0.02 to about 0.04. (See Figure 4.1 and Figure 4.2) to the actual experimental strains at which the crack is propagating measured with DIC effects. This

might require a higher magnification lens than the 5X used in this study to clearly see the crack propagating and map out the actual strains at crack propagation.

5. Further, the incorporation of crack propagation into the model will broaden its applicability. For instance, the model can then be used to investigate how the changes in MDPZ size and shape affect crack propagation in cortical bone.
6. In this study, the MDPZ was modelled for bovine cortical bone. Though a good first step, bovine cortical bone has some distinct differences from human cortical bone. The dominant form of bone type in bovine cortical bone is plexiform bone but that of human cortical bone is osteonal bone. The osteonal bone consist of concentric lamellae layers around a haversian canal while plexiform bone is made up by alternating layers of lamellae sheets with non-lamellae sheets which are highly mineralised [20]. Also, previous work from Woodside et al.[60] have shown that bovine cortical bone undergoes a more sudden fracture while human cortical bone is able to undergo considerable stable tearing before sudden rupture. Hence, an extension of the CDM model to human cortical bone and its validation will be required for its application as a tool for investigations into the human bone fracture.

Letters of copyright permission

Figure 1.2 and 1.3

License Number	4477250026275
License date	Nov 27, 2018
Licensed Content Publisher	Elsevier
Licensed Content Publication	Medical Engineering & Physics
Licensed Content Title	Mechanical properties and the hierarchical structure of bone
Licensed Content Author	Jae-Young Rho,Liisa Kuhn-Spearing,Peter Zioupos
Licensed Content Date	Mar 1, 1998
Licensed Content Volume	20
Licensed Content Issue	2
Licensed Content Pages	11
Start Page	92
End Page	102
Type of Use	reuse in a thesis/dissertation
Portion	figures/tables/illustrations
Number of figures/tables/illustrations	2
Format	both print and electronic
Are you the author of this Elsevier article?	No
Will you be translating?	No
Original figure numbers	figures 1 and 2
Title of your thesis/dissertation	An experimentally validated continuum damage mechanics model of the microdamage process zone during cortical bone fracture
Expected completion date	Dec 2018
Estimated size (number of pages)	130

Figure 1.4 and 1.6

License Number	4477280944218
License date	Nov 27, 2018
Licensed content publisher	Annual Reviews, Inc
Licensed content title	Annual review of materials research
Licensed content date	Jan 1, 2001
Type of Use	Thesis/Dissertation
Requestor type	Academic institution
Format	Print, Electronic
Portion	chart/graph/table/figure
Number of charts/graphs/tables/figures	1
The requesting person/organization is:	Daniel Yaw Dapaah
Title or numeric reference of the portion(s)	Figure 3
Title of the article or chapter the portion is from	On the Mechanistic Origins of Toughness in Bone
Editor of portion(s)	N/A
Author of portion(s)	M. Launey, M.J. Buehler and R. O. Ritchie
Volume of serial or monograph.	40
Issue, if republishing an article from a serial	1
Page range of the portion	32
Publication date of portion	2010
Rights for	Main product
Duration of use	Life of current edition
Creation of copies for the disabled	no
With minor editing privileges	no
For distribution to	Canada
In the following language(s)	Original language of publication
With incidental promotional use	no

The lifetime unit quantity of new product	Up to 499
Title	An experimentally validated continuum damage mechanics model of the microdamage process zone during cortical bone fracture
Institution name	n/a
Expected presentation date	Dec 2018

Figure 1.7

License Number	4486631315967
License date	Dec 12, 2018
Licensed content publisher	Taylor and Francis Group LLC Books
Licensed content title	Fracture mechanics : fundamentals and applications
Licensed content date	Jan 1, 2005
Type of Use	Thesis/Dissertation
Requestor type	Academic institution
Format	Print, Electronic
Portion	chart/graph/table/figure
Number of charts/graphs/tables/figures	1
The requesting person/organization is:	Daniel Yaw Dapaah
Title or numeric reference of the portion(s)	Figure 2.29
Title of the article or chapter the portion is from	Linear elastic fracture mechanics
Editor of portion(s)	N/A
Author of portion(s)	T. L. Anderson
Volume of serial or monograph.	3
Page range of the portion	62
Publication date of portion	2005

Rights for	Main product
Duration of use	Life of current edition
Creation of copies for the disabled	no
With minor editing privileges	no
For distribution to	Worldwide
In the following language(s)	Original language of publication
With incidental promotional use	no
The lifetime unit quantity of new product	Up to 999
Title	An experimentally validated continuum damage mechanics model of the microdamage process zone during cortical bone fracture
Institution name	n/a
Expected presentation date	Dec 2018

Figure 1.8 and 1.9

License Number	4477840136752
License date	Nov 28, 2018
Licensed Content Publisher	Elsevier
Licensed Content Publication	Engineering Fracture Mechanics
Licensed Content Title	A cohesion model of microcrack toughening
Licensed Content Author	Li Zhonghua,Zhao Yong,S. Schmauder
Licensed Content Date	Jan 1, 1993
Licensed Content Volume	44
Licensed Content Issue	2
Licensed Content Pages	9
Start Page	257
End Page	265

Type of Use	reuse in a thesis/dissertation
Intended publisher of new work	other
Portion	figures/tables/illustrations
Number of figures/tables/illustrations	1
Format	both print and electronic
Are you the author of this Elsevier article?	No
Will you be translating?	No
Original figure numbers	figure 2
Title of your thesis/dissertation	An experimentally validated continuum damage mechanics model of the microdamage process zone during cortical bone fracture
Expected completion date	Dec 2018
Estimated size (number of pages)	130

Figure 5.4

License Number	4486791316285
License date	Dec 12, 2018
Licensed content publisher	Taylor and Francis Group LLC Books
Licensed content title	Fracture mechanics : fundamentals and applications
Licensed content date	Jan 1, 2005
Type of Use	Thesis/Dissertation
Requestor type	Academic institution
Format	Print, Electronic
Portion	chart/graph/table/figure
Number of charts/graphs/tables/figures	1
The requesting person/organization is:	Daniel Yaw Dapaah
Title or numeric reference of the portion(s)	Figure 2.34a

Title of the article or chapter the portion is from	Linear fracture mechanics
Editor of portion(s)	N/A
Author of portion(s)	T. L. Anderson
Volume of serial or monograph.	3
Page range of the portion	68
Publication date of portion	2005
Rights for	Main product
Duration of use	Life of current edition
Creation of copies for the disabled	no
With minor editing privileges	no
For distribution to	Worldwide
In the following language(s)	Original language of publication
With incidental promotional use	no
The lifetime unit quantity of new product	Up to 999
Title	An experimentally validated continuum damage mechanics model of the microdamage process zone during cortical bone fracture
Institution name	n/a
Expected presentation date	Dec 2018

Figure 5.5

License Number	4477830731910
License date	Nov 28, 2018
Licensed Content Publisher	Elsevier

Licensed Content Publication	Engineering Fracture Mechanics
Licensed Content Title	A cohesion model of microcrack toughening
Licensed Content Author	Li Zhonghua,Zhao Yong,S. Schmauder
Licensed Content Date	Jan 1, 1993
Licensed Content Volume	44
Licensed Content Issue	2
Licensed Content Pages	9
Start Page	257
End Page	265
Type of Use	reuse in a thesis/dissertation
Portion	figures/tables/illustrations
Number of figures/tables/illustrations	1
Format	both print and electronic
Are you the author of this Elsevier article?	No
Will you be translating?	No
Original figure numbers	figure 4
Title of your thesis/dissertation	An experimentally validated continuum damage mechanics model of the microdamage process zone during cortical bone fracture
Expected completion date	Dec 2018
Estimated size (number of pages)	130

References

[1] O. Johnell and J. A. Kanis, “An estimate of the worldwide prevalence and disability associated with osteoporotic fractures,” *Osteoporos. Int.*, vol. 17, pp. 1726–1733, 2006.

[2] M. J. Haentjens P., “Meta-analysis : Excess Mortality After Hip Fracture Among Older Women and Men,” *Ann. Intern. Med.*, vol. 152, pp. 380–390, 2010.

[3] M. E. Wiktorowicz, R. Goeree, A. Papaioannou, J. D. Adachi, and E. Papadimitropoulos, “Economic implications of hip fracture: health service use, institutional care and cost in Canada.,” *Osteoporos. Int.*, vol. 12, no. 4, pp. 271–278, 2001.

[4] Health Canada, “Canada’s Aging Population,” 2002.

[5] G. M. Kiebzak, “Age-related bone changes.,” *Exp. Gerontol.*, vol. 26, no. 2–3, pp. 171–187, 1991.

[6] S. L. Hui, C. W. Slemenda, and C. C. Johnston, “Age and bone mass as predictors of fracture in a prospective study,” *J. Clin. Invest.*, vol. 81, no. 6, pp. 1804–1809, 1988.

[7] D. Marshall, O. Johnell, and H. Wedel, “Meta-Analysis Of How Well Measures Of Bone Mineral Density Predict Occurrence Of Osteoporotic Fractures,” *Br. Med. J.*, vol. 312, no. 7041, pp. 1254–1259, 1996.

[8] X. G. Cheng *et al.*, “Assessment of the strength of proximal femur in vitro: Relationship to femoral bone mineral density and femoral geometry,” *Bone*, vol. 20, no. 3, pp. 213–218, 1997.

[9] S. C. Manolagas and A. M. Parfitt, “What old means to bone,” *Trends Endocrinol. Metab.*, vol. 21, no. 6, pp. 369–374, 2010.

[10] J. N. Farr and S. Khosla, “Determinants of bone strength and quality in diabetes mellitus in humans,” *Bone*, vol. 82, pp. 28–34, 2016.

[11] E. M. B. McNerny and T. L. Nickolas, “Bone Quality in Chronic Kidney Disease: Definitions and Diagnostics,” *Curr. Osteoporos. Rep.*, vol. 15, no. 3, pp. 207–213, 2017.

[12] S. Viguet-Carrin, P. Garnero, and P. D. Delmas, “The role of collagen in bone strength,” *Osteoporos. Int.*, vol. 17, no. 3, pp. 319–336, 2006.

[13] R. K. Nalla, J. J. Kruzic, J. H. Kinney, and R. O. Ritchie, “Mechanistic aspects of fracture and R-curve behavior in human cortical bone,” *Biomaterials*, vol. 26, pp. 217–231, 2005.

[14] Q. D. Yang, B. N. Cox, R. K. Nalla, and R. O. Ritchie, “Fracture length scales in human cortical bone : The necessity of nonlinear fracture models,” *Biomaterials*, vol. 27, pp. 2095–2113, 2006.

[15] E. A. Zimmermann, B. Busse, and R. O. Ritchie, “The fracture mechanics of human bone : influence of disease and treatment,” *Bonekey Rep.*, vol. 4, no. 743, pp. 1–13, 2015.

[16] J. Y. Rho, L. Kuhn-Spearing, and P. Zioupos, “Mechanical properties and the hierarchical structure of bone,” *Med. Eng. Phys.*, vol. 20, no. 2, pp. 92–102, 1998.

[17] M. J. Olszta *et al.*, “Bone structure and formation: A new perspective,” *Mater. Sci. Eng. R Reports*, vol. 58, no. 3–5, pp. 77–116, 2007.

[18] P. Fratzl, H. S. Gupta, E. P. Paschalis, and P. Roschger, “Structure and mechanical quality of the collagen? Mineral nano-composite in bone,” *J. Mater. Chem.*, vol. 14, no. 14, pp. 2115–2123, 2004.

[19] P. Fratzl and R. Weinkamer, “Nature’s hierarchical materials,” *Prog. Mater. Sci.*, vol. 52, no. 8, pp. 1263–1334, 2007.

[20] S. Weiner and H. D. Wagner, “THE MATERIAL BONE: Structure-Mechanical Function Relations,” *Annu. Rev. Mater. Sci.*, vol. 28, no. 1, pp. 271–298, 1998.

[21] M. J. Buehler, “Nature designs tough collagen: Explaining the nanostructure of collagen fibrils,” *Proc. Natl. Acad. Sci.*, vol. 103, no. 33, pp. 12285–12290, 2006.

[22] W. Weiner, S.; Traub, “Bone Structure : From angstroms to microns,” *FASEB J.*, vol. 6, no. 3, pp. 879–885, 1992.

[23] M. J. Buehler, “Molecular nanomechanics of nascent bone: Fibrillar toughening by mineralization,” *Nanotechnology*, vol. 18, no. 29, 2007.

[24] L. J. Gibson and M. F. Ashby, *Cellular solids: Structure and properties*, 2nd ed. Cambridge University Press, 1997.

[25] M. Fatima, H. Canhao, and J. Eurico, “Bone: A Composite Natural Material,” *Adv.*

Compos. Mater. - Anal. Nat. Man-Made Mater., no. September 2011, 2011.

[26] M. M. Giraud-Guille, "Twisted plywood architecture of collagen fibrils in human compact bone osteons," *Calcif. Tissue Int.*, vol. 42, no. 3, pp. 167–180, 1988.

[27] D. P. Nicolella, Q. Ni, and K. S. Chan, "Non-destructive characterization of microdamage in cortical bone using low field pulsed NMR," *J. Mech. Behav. Biomed. Mater.*, vol. 4, no. 3, pp. 383–391, 2011.

[28] L. F. Bonewald, "The amazing osteocyte," *J. Bone Miner. Res.*, vol. 26, no. 2, pp. 229–238, 2011.

[29] L. J. Gibson, "Biomechanics of cellular solids," *J. Biomech.*, vol. 38, no. 3, pp. 377–399, 2005.

[30] M. F. Ashby, *Materials Selection in Mechanical Design*. USA: Elsevier Ltd., 2011.

[31] C. T. Sun and Z. H. Jin, *Fracture Mechanics*. Oxford: Elsevier Inc., 2012.

[32] A. . A. . Griffith, "The Phenomena of Rupture and Flow in Solids," *Philos. Trans. R. Soc. london. Ser. A, Contain. Pap. a Math. or Phys. character*, vol. 221, no. 1921, pp. 163–198, 2016.

[33] R. O. Ritchie, "How does human bone resist fracture ?," *Ann. New York Acad. Sci.*, vol. 1192, pp. 72–80, 2010.

[34] R. O. Ritchie, M. J. Buehler, and P. Hansma, "Plasticity and toughness in bone," *Phys. Today*, vol. 62, no. 6, pp. 41–47, 2009.

[35] M. E. Launey, M. J. Buehler, and R. O. Ritchie, *On the Mechanistic Origins of Toughness in Bone*, vol. 40, no. 1. 2010.

[36] A. Gautieri, M. J. Buehler, and A. Redaelli, "Deformation rate controls elasticity and unfolding pathway of single tropocollagen molecules," *J. Mech. Behav. Biomed. Mater.*, vol. 2, no. 2, pp. 130–137, 2009.

[37] G. E. Fantner *et al.*, "Sacrificial bonds and hidden length: Unraveling molecular mesostructures in tough materials," *Biophys. J.*, vol. 90, no. 4, pp. 1411–1418, 2006.

[38] G. E. Fantner *et al.*, “Sacrificial bonds and hidden length dissipate energy as mineralized fibrils separate during bone fracture,” *Nat. Mater.*, vol. 4, no. 8, pp. 612–616, 2005.

[39] H. S. Gupta *et al.*, “Nanoscale deformation mechanisms in bone,” *Nano Lett.*, vol. 5, no. 10, pp. 2108–2111, 2005.

[40] K. J. Koester, J. W. Ager, and R. O. Ritchie, “The true toughness of human cortical bone measured with realistically short cracks,” *Nat. Mater.*, vol. 7, no. 8, pp. 672–677, 2008.

[41] R. K. Nalla, J. H. Kinney, and R. O. Ritchie, “Mechanistic fracture criteria for the failure of human cortical bone,” *Nat. Mater.*, vol. 2, no. March, 2003.

[42] R. K. Nalla, J. J. Kruzic, and R. O. Ritchie, “On the origin of the toughness of mineralized tissue : microcracking or crack bridging ?,” *Bone*, vol. 34, pp. 790–798, 2004.

[43] R. O. Ritchie, J. H. Kinney, J. J. Kruzic, and R. K. Nalla, “A fracture mechanics and mechanistic approach to the failure of cortical bone,” *Fatigue Fract. Eng. Mater. Struct.*, vol. 28, pp. 345–371, 2005.

[44] Y. N. Yeni and D. P. Fyhrie, “A rate-dependent microcrack-bridging model that can explain the strain rate dependency of cortical bone apparent yield strength,” *J. Biomech.*, vol. 36, no. 9, pp. 1343–1353, 2003.

[45] R. K. Nalla, J. S. Stolken, J. H. Kinney, and R. O. Ritchie, “Fracture in human cortical bone : local fracture criteria and toughening mechanisms,” *J. Biomech.*, vol. 38, pp. 1517–1525, 2005.

[46] M. J. Buehler, “Atomistic and continuum modeling of mechanical properties of collagen: Elasticity, fracture, and self-assembly,” *J. Mater. Res.*, vol. 21, no. 8, pp. 1947–1961, 2006.

[47] T. L. Willett, D. Y. Dapaah, S. Uppuganti, M. Granke, and J. S. Nyman, “Bone collagen network integrity and transverse fracture toughness of human cortical bone,” *Bone*, vol. 120, no. October 2018, pp. 187–193, 2018.

[48] P. Zioupos, J. D. Currey, and A. J. Hamer, “The role of collagen in the declining mechanical properties of aging human cortical bone,” 1999.

[49] R. Pacifici, R. Rupich, K. C. Vered, and M. Fisher, “Dual Energy Radiography (DER): A Preliminary Comparative Study,” *Calcif. Tissue Int.*, vol. 43, pp. 189–191, 1988.

[50] K. Micha, P. Aspenberg, and H. Siev, “Osteoporosis : the emperor has no clothes,” *J. Intern. Med.*, 2015.

[51] Z. Feng, J. Rho, S. Han, and I. Ziv, “Orientation and loading condition dependence of fracture toughness in cortical bone,” *Mater. Sci. Eng. C*, vol. 11, pp. 41–46, 2000.

[52] T. L. Norman, S. V. Nivargikar, and D. B. Burr, “Resistance to crack growth in human cortical bone is greater in shear than in tension,” *J. Biomech.*, vol. 29, no. 8, pp. 1023–1031, 1996.

[53] Y. N. Yeni and T. L. Norman, “Fracture toughness of human femoral neck: Effect of microstructure, composition, and age,” *Bone*, vol. 26, no. 5, pp. 499–504, 2000.

[54] R. K. Nalla, J. J. Kruzic, J. H. Kinney, and R. O. Ritchie, “Effect of aging on the toughness of human cortical bone : evaluation by R-curves,” *Bone*, vol. 35, pp. 1240–1246, 2004.

[55] D. Vashishth, K. E. Tanner, and W. Bonfield, “Experimental validation of a microcracking-based toughening mechanism for cortical bone,” *J. Biomech.*, vol. 36, pp. 121–124, 2003.

[56] D. Vashishth, “Rising crack-growth-resistance behavior in cortical bone: Implications for toughness measurements,” *J. Biomech.*, vol. 37, no. 6, pp. 943–946, 2004.

[57] C. L. Malik, S. M. Stover, R. B. Martin, and J. C. Gibeling, “Equine cortical bone exhibits rising R-curve fracture mechanics,” *J. Biomech.*, vol. 36, pp. 191–198, 2003.

[58] J. Yan, J. J. Mecholsky, and K. B. Clifton, “How tough is bone ? Application of elastic – plastic fracture mechanics to bone,” *Bone*, vol. 40, pp. 479–484, 2007.

[59] L. A. Pruitt and A. M. Chakravartula, *Mechanics of biomaterials: fundamental principles for implant design*. New York: Cambridg University Press, 2011.

[60] M. Woodside and T. L. Willett, “Elastic – plastic fracture toughness and rising J R -curve behavior of cortical bone is partially protected from irradiation – sterilization-induced

degradation by ribose protectant," *J. Mech. Behav. Biomed. Mater.*, vol. 64, pp. 53–64, 2016.

[61] R. Gauthier *et al.*, "Strain rate influence on human cortical bone toughness: A comparative study of four paired anatomical sites," *J. Mech. Behav. Biomed. Mater.*, vol. 71, no. March, pp. 223–230, 2017.

[62] L. Zhonghua, Z. Yong, and S. Schmauder, "A cohesion model of microcrack toughening," *Eng. Fract. Mech.*, vol. 44, no. 2, pp. 257–265, 1993.

[63] F. A. M. Pereira, M. F. S. F. De Moura, N. Dourado, J. J. L. Morais, J. Xavier, and M. I. R. Dias, "Direct and inverse methods applied to the determination of mode I cohesive law of bovine cortical bone using the DCB test," *Int. J. Solids Struct.*, vol. 0, pp. 1–11, 2017.

[64] D. Vashishth, "Hierarchy of bone microdamage at multiple length scales," *Int. J. Fatigue*, vol. 29, no. 6, pp. 1024–1033, 2007.

[65] A. A. Poundarik and D. Vashishth, "Multiscale imaging of bone microdamage," *Connect. Tissue Res.*, vol. 56, no. 2, pp. 87–98, 2015.

[66] O. C. Yeh and T. M. Keaveny, "Relative roles of microdamage and microfracture in the mechanical behavior of trabecular bone," *J. Orthop. Res.*, vol. 19, no. 6, pp. 1001–1007, 2001.

[67] H. M. Frost, "Presence of microscope cracks in vivo in bone," *Henry Ford Hosp. Bull.*, vol. 8, pp. 25–35, 1960.

[68] S. D. Burr and T. Stafford, "Validity of the bulk staining technique to seperate artifactual from in vivo bone microdamage," *Clin. Orthop. Relat. Res.*, vol. 260, pp. 305–308, 1994.

[69] T. E. Wenzel, M. B. Schaffler, and D. P. Fyhrie, "In vivo trabecular microcracks in human vertebral bone," *Bone*, vol. 19, no. 2, pp. 89–95, 1996.

[70] Z. Wang and T. L. Norman, "Microdamage of human cortical bone: Incidence and morphology in long bones," *Bone*, vol. 20, no. 4, pp. 375–379, 1997.

[71] M. B. Schaffler, K. Choi, and C. Milgrom, "Aging and matrix microdamage accumulation in human compact bone," *Bone*, vol. 17, no. 6, pp. 521–525, 1995.

[72] T. Diab and D. Vashishth, “Effects of damage morphology on cortical bone fragility,” *Bone*, vol. 37, no. 1, pp. 96–102, 2005.

[73] T. Diab and D. Vashishth, “Morphology, localization and accumulation of in vivo microdamage in human cortical bone,” *Bone*, vol. 40, no. 3, pp. 612–618, 2007.

[74] T. Diab, K. W. Condon, D. B. Burr, and D. Vashishth, “Age-related change in the damage morphology of human cortical bone and its role in bone fragility,” *Bone*, vol. 38, no. 3, pp. 427–431, 2006.

[75] W. T. George and D. Vashishth, “Damage mechanisms and failure modes of cortical bone under components of physiological loading,” *J. Orthop. Res.*, vol. 23, no. 5, pp. 1047–1053, 2005.

[76] D. Vashishth *et al.*, “In vivo diffuse damage in human vertebral trabecular bone,” *Bone*, vol. 26, no. 2, pp. 147–152, 2000.

[77] O. Akkus, K. J. Jepsen, and C. M. Rimnac, “Microstructural aspects of the fracture process in human cortical bone,” *J. Mater. Sci.*, vol. 35, no. 24, pp. 6065–6074, 2000.

[78] T. Willett, D. Josey, R. Xing, Z. Lu, G. Minhas, and J. Montesano, “The micro-damage process zone during transverse cortical bone fracture : No ears at crack growth initiation,” *J. Mech. Behav. Biomed. Mater.*, vol. 74, no. June, pp. 371–382, 2017.

[79] A. Carpinteri, *Nonlinear Crack Models for Nonmetallic Materials*. Boston: Kluwer Academic Publishers, 1999.

[80] National Institute of Health, “How can computational modeling accelerate discovery?,” 2016.

[81] G. W. Brodland, “How computational models can help unlock biological systems,” *Semin. Cell Dev. Biol.*, vol. 47–48, pp. 62–73, 2015.

[82] Q. Luo, R. Nakade, X. Dong, Q. Rong, and X. Wang, “Effect of mineral-collagen interfacial behavior on the microdamage progression in bone using a probabilistic cohesive finite element model,” *J. Mech. Behav. Biomed. Mater.*, vol. 4, no. 7, pp. 943–952, 2011.

[83] A. Barkaoui, A. Bettamer, and R. Hambli, “Failure of mineralized collagen microfibrils using finite element simulation coupled to mechanical quasi-brittle damage,” *Procedia Eng.*, vol. 10, pp. 3185–3190, 2011.

[84] A. Raeisi Najafi, A. R. Arshi, M. R. Eslami, S. Fariborz, and M. H. Moeinzadeh, “Micromechanics fracture in osteonal cortical bone: A study of the interactions between microcrack propagation, microstructure and the material properties,” *J. Biomech.*, vol. 40, no. 12, pp. 2788–2795, 2007.

[85] F. J. O’Brien, D. Taylor, and T. C. Lee, “The effect of bone microstructure on the initiation and growth of microcracks,” *J. Orthop. Res.*, vol. 23, no. 2, pp. 475–480, 2005.

[86] S. Mischinski and A. Ural, “Finite Element Modeling of Microcrack Growth in Cortical Bone,” *J. Appl. Mech.*, vol. 78, no. 4, p. 041016, 2011.

[87] S. Mischinski and A. Ural, “Interaction of microstructure and microcrack growth in cortical bone: A finite element study,” *Comput. Methods Biomech. Biomed. Engin.*, vol. 16, no. 1, pp. 81–94, 2013.

[88] *Abaqus documentation 2016, analsysis user guide*. BS Simulia.

[89] E. Budyn, T. Hoc, and J. Jonvaux, “Fracture strength assessment and aging signs detection in human cortical bone using an X-FEM multiple scale approach,” *Comput. Mech.*, vol. 42, no. 4, pp. 579–591, 2008.

[90] A. A. Abdel-Wahab, A. R. Maligno, and V. V. Silberschmidt, “Micro-scale modelling of bovine cortical bone fracture: Analysis of crack propagation and microstructure using X-FEM,” *Comput. Mater. Sci.*, vol. 52, no. 1, pp. 128–135, 2012.

[91] S. Li, A. Abdel-Wahab, E. Demirci, and V. V. Silberschmidt, “Fracture process in cortical bone: X-FEM analysis of microstructured models,” *Int. J. Fract.*, vol. 184, no. 1–2, pp. 43–55, 2013.

[92] J. Lemaitre and R. Desmorat, *Engineering Damage Mechanics*. Berlin: Springer, 2005.

[93] S. C. Cowin, Ed., *Bone Mechanics Handbook*, 2nd ed. CRC Press LLC, 2001.

[94] L. M. Kachanov, *Introduction to Continuum Damage Mechanics*. Dordrecht, The

Netherlands: Martinus Nijhoff, 1986.

[95] G. Z. Voyiadjis and T. Park, “Anisotropic damage effect tensors for the symmetrization of the effective stress tensor,” *J. Appl. Mech. Trans. ASME*, vol. 64, no. 1, pp. 106–110, 1997.

[96] D. Krajcinovic, *Damage Mechanics*. New York: North-Holland Elsevier, 1996.

[97] S. Yoneyama, “Basic principle of digital image correlation for in-plane displacement and strain measurement,” *Adv. Compos. Mater.*, vol. 25, no. 2, pp. 105–123, 2016.

[98] A. Giachetti, “Matching techniques to compute image motion,” *Image Vis. Comput.*, vol. 18, no. 3, pp. 247–260, 2000.

[99] H. W. Schreier, J. R. Braasch, and M. A. Sutton, “Systematic errors in digital image correlation caused by intensity interpolation,” *Library (Lond).*, vol. 39, no. November, pp. 2915–2921, 2000.

[100] M. A. Sutton, S. R. McNeill, J. Jang, and M. Babai, “Effects of subpixel image restoration on digital correlation error estimates,” *Opt. Eng.*, vol. 27, no. 10, pp. 870–877, 1988.

[101] H. W. Schreier and M. A. Sutton, “Systematic errors in digital image correlation due to undermatched subset shape functions,” *Exp. Mech.*, vol. 42, no. 3, pp. 303–310, 2002.

[102] H. A. Bruck, S. R. McNeill, M. A. Sutton, and W. H. Peters, “Digital image correlation using Newton-Raphson method of partial differential correction,” *Exp. Mech.*, vol. 29, no. 3, pp. 261–267, 1989.

[103] B. Pan, K. Qian, H. Xie, and A. Asundi, “Two-dimensional digital image correlation for in-plane displacement and strain measurement : a review,” *Meas. Sci. Technol.*, vol. 20, pp. 1–17, 2009.

[104] M. A. Sutton, J. J. Orteu, and H. Schreier, *Image correlation for shape, motion and deformation measurements: basic concepts, theory and applications*. Springer Science, 2009.

[105] Z. Hashin, “Failure Criteria for Unidirectional Fibre Composites,” *J. Appl. Mech.*, vol. 47, no. June, pp. 329–334, 1980.

[106] L. J. Katz, “Anisotropy of Young’s modulus of bone,” *Nature*, vol. 283, 1980.

[107] I. Lapczyk and J. A. Hurtado, “Progressive damage modeling in fiber-reinforced materials,” *Compos. Part A Appl. Sci. Manuf.*, vol. 38, no. 11, pp. 2333–2341, 2007.

[108] C. G. Dávila and P. P. Camanho, “Failure Criteria for FRP Laminates in Plane Stress,” *J. Compos. Mater.*, vol. 39, no. 4, pp. 323–345, 2005.

[109] G. Duvant and J. L. Lions, *Inequalities in mechanics and physics*. Berlin: Springer, 1976.

[110] D. T. Reilly and A. H. Burstein, “THE ELASTIC AND ULTIMATE PROPERTIES OF COMPACT BONE TISSUE ”?,” *J. Biomech.*, pp. 393–405, 1975.

[111] S. Li, E. Demirci, and V. V. Silberschmidt, “Variability and anisotropy of mechanical behavior of cortical bone in tension and compression,” *J. Mech. Behav. Biomed. Mater.*, vol. 21, pp. 109–120, 2013.

[112] J. D. Currey, “Effects of differences in mineralization on the mechanical properties of bone.,” *Philos. Trans. R. Soc. Lond. B. Biol. Sci.*, vol. 304, no. 1121, pp. 509–518, 1984.

[113] D. W. Wagner, D. P. Lindsey, and G. S. Beaupre, “Deriving tissue density and elastic modulus from microCT bone scans,” *Bone*, vol. 49, no. 5, pp. 931–938, 2011.

[114] C. H. Turner, T. Wang, and D. B. Burr, “Shear strength and fatigue properties of human cortical bone determined from pure shear tests,” *Calcif. Tissue Int.*, vol. 69, no. 6, pp. 373–378, 2001.

[115] M. T. Fondrk, E. H. Bahniuk, and D. T. Davy, “A damage model for nonlinear tensile behavior of cortical bone.,” *J. Biomech. Eng.*, vol. 121, no. 5, pp. 533–41, 1999.

[116] M. Fondrk, E. Bahniuk, D. T. Davy, and C. Michaels, “Some viscoplastic characteristics of bovine and human cortical bone,” *J. Biomech.*, vol. 21, no. 8, pp. 623–630, 1988.

[117] ASTM, *Standard test method for measurement of fracture toughness*. West Conshohocken, PA: ASTM international, 2014.

[118] ASTM, *Standard test method for determining J-R curves of plastic materials*. West Conshohocken, PA: ASTM international, 2010.

[119] J. D. Currey, “The effects of drying and re-wetting on some mechanical properties of cortical bone,” *J. Biomech.*, vol. 21, no. 5, pp. 439–441, 1988.

[120] T. L. Willett, B. Burton, M. Woodside, Z. Wang, A. Gaspar, and T. Attia, “γ-Irradiation sterilized bone strengthened and toughened by ribose pre-treatment,” *J. Mech. Behav. Biomed. Mater.*, vol. 44, pp. 147–155, 2015.

[121] B. Burton, A. Gaspar, D. Josey, J. Tupy, M. D. Grynpas, and T. L. Willett, “Bone embrittlement and collagen modi fi cations due to high-dose gamma-irradiation sterilization,” *Bone*, vol. 61, pp. 71–81, 2014.

[122] P. F. Liu and J. Y. Zheng, “Recent developments on damage modeling and finite element analysis for composite laminates: A review,” *Mater. Des.*, vol. 31, no. 8, pp. 3825–3834, 2010.

[123] H. Kuna-Ciskał and J. J. Skrzypek, “CDM based modelling of damage and fracture mechanisms in concrete under tension and compression,” *Eng. Fract. Mech.*, vol. 71, no. 4–6, pp. 681–698, 2004.

[124] D. Vashishth, K. E. Tanner, and W. Bon, “Contribution , development and morphology of microcracking in cortical bone during crack propagation,” *J. Biomech.*, vol. 33, pp. 1169–1174, 2000.

[125] T. L. Anderson, *Fracture mechanics: Fundamentals and Applications*. Boca Raton: CRC Press LLC, 2005.

[126] F. Barthelat and H. D. Espinosa, “An experimental investigation of deformation and fracture of nacre-mother of pearl,” *Exp. Mech.*, vol. 47, no. 3, pp. 311–324, 2007.

[127] B. N. Cox and Q. Yang, “Cohesive zone models of localization and fracture in bone,” *Eng. Fract. Mech.*, vol. 74, no. 7, pp. 1079–1092, 2007.

[128] R. K. Chintapalli, S. Breton, A. K. Dastjerdi, and F. Barthelat, “Strain rate hardening: A hidden but critical mechanism for biological composites?,” *Acta Biomater.*, vol. 10, no. 12, pp. 5064–5073, 2014.

[129] F. Barthelat, R. Rabiei, and A. K. Dastjerdi, “Multiscale toughness amplification in

natural composites," *Mater. Res. Soc. Symp. Proc.*, vol. 1420, no. 4, pp. 61–66, 2012.

[130] N. Sasaki, Y. Nakayama, M. Yoshikawa, and A. Enyo, "Stress relaxation function of bone and bone collagen," *J. Biomech.*, vol. 26, no. 12, pp. 1369–1376, 1993.

[131] M. J. Buehler, S. Keten, and T. Ackbarow, "Theoretical and computational hierarchical nanomechanics of protein materials: Deformation and fracture," *Prog. Mater. Sci.*, vol. 53, no. 8, pp. 1101–1241, 2008.

[132] A. Dziedzic-Goclawska, A. Kaminski, I. Uhrynowska-Tyszkiewicz, and W. Stachowicz, "Irradiation as a safety procedure in tissue banking," *Cell Tissue Bank.*, vol. 6, no. 3, pp. 201–219, 2005.

[133] https://commons.wikimedia.org/wiki/File:Medical_X-Ray_imaging_IYN05_nevit.jpg

[134] https://commons.wikimedia.org/wiki/File:Elliptical_crack_in_infinite_plate.png

Appendix: mechanical properties tables

E represents Young's modulus

G represents Shear modulus

v represents Poisson ratio

X represents Hashin longitudinal failure strength

Y represents Hashin transverse failure strength

G_c represents the fracture energy

η represents the viscosity parameter.

The superscripts T, C and S stand for tension, compression and shear respectively while the subscripts 1, 2 and 3 stand for the longitudinal, circumferential (transverse) and radial axes of the specimen

Table A.1: Verification of bi-linear CDM law mechanical properties used for both longitudinal and transverse tensile tests

Elastic moduli	Value (MPa)
E_1	19100
E_2	10400
v_{12}	0.275
G_{12}	4100
G_{13}	4100
G_{23}	3300

Hashin Strengths	Value (MPa)
X^T	95
X^C	190
X^S	50
Y^T	50
Y^C	105
Y^S	70

Fracture energies per element	Value (N/mm)
$G_{C(1)}^{T}$	0.00475
$G_{C(1)}^{C}$	0.0076
$G_{C(2)}^{T}$	0.00875
$G_{C(2)}^{C}$	0.011

Viscosity parameters	Value
η_1	0.07
η_2	0.05

Table A.2: Mesh sensitivity test mechanical properties excluding fracture energies. These mechanical properties were consistent throughout the different mesh size test.

Elastic moduli	Value (MPa)
E_1	19100
E_2	10400
v_{12}	0.275
G_{12}	4100
G_{13}	4100
G_{23}	3300

Hashin Strengths	Value (MPa)
X^T	95
X^C	190
X^S	50
Y^T	50
Y^C	105
Y^S	70

Viscosity parameters	Value
η_1	0.08
η_2	0.05

The different fracture energies used for the different ROI mesh sizes are presented below:

Table A.2.1: Fracture energy for ROI mesh size= 0.0075mm

Fracture energies per element	Value (N/mm)
$G_{C(1)}^{T}$	0.003563
$G_{C(1)}^{C}$	0.0057
$G_{C(2)}^{T}$	0.000656
$G_{C(2)}^{C}$	0.00827

Table A.2.2: Fracture energy for ROI mesh size= 0.01mm

Fracture energies per element	Value (N/mm)
$G_{C(1)}^{T}$	0.00475
$G_{C(1)}^{C}$	0.0076
$G_{C(2)}^{T}$	0.000875
$G_{C(2)}^{C}$	0.011

Table A.2.3: Fracture energy for ROI mesh size= 0.015mm

Fracture energies per element	Value (N/mm)
$G_{C(1)}^{T}$	0.007125
$G_{C(1)}^{C}$	0.0114
$G_{C(2)}^{T}$	0.00131
$G_{C(2)}^{C}$	0.0165

Table A.2.4: Fracture energy for ROI mesh size= 0.03mm

Fracture energies per element	Value (N/mm)
$G_{C(1)}^{T}$	0.01425
$G_{C(1)}^{C}$	0.0228
$G_{C(2)}^{T}$	0.002625
$G_{C(2)}^{C}$	0.033

Table A.2.5: Fracture energy for ROI mesh size= 0.05mm

Fracture energies per element	Value (N/mm)
$G_{C(1)}^{T}$	0.02375
$G_{C(1)}^{C}$	0.038
$G_{C(2)}^{T}$	0.004375
$G_{C(2)}^{C}$	0.05513

Table A.3: Bovine femur specimen 1 mechanical properties

Elastic moduli	Value (MPa)
E_1	18300
E_2	9900
v_{12}	0.275
G_{12}	4100
G_{13}	4100
G_{23}	3200

Hashin Strengths	Value (MPa)
X^T	80
X^C	190
X^S	40
Y^T	50
Y^C	105
Y^S	70

Fracture energies per element	Value (N/mm)
$G_{C(1)}^{T}$	0.004
$G_{C(1)}^{C}$	0.0076
$G_{C(2)}^{T}$	0.0007
$G_{C(2)}^{C}$	0.011

Viscosity parameters	Value
η_1	0.07
η_2	0.05

Table A.3.1: Viscosity parameter sensitivity test done with bovine femur specimen 1 mechanical properties. The only change from the mechanical properties of the bovine femur specimen 1 is in the viscosity parameter values.

Elastic moduli	Value (MPa)
E_1	18300
E_2	9900
v_{12}	0.275
G_{12}	4100
G_{13}	4100
G_{23}	3200

Hashin Strengths	Value (MPa)
X^T	80
X^C	190
X^S	40
Y^T	50
Y^C	105
Y^S	70

Fracture energies per element	Value (N/mm)
$G_{C(1)}^{T}$	0.004
$G_{C(1)}^{C}$	0.0076
$G_{C(2)}^{T}$	0.0007
$G_{C(2)}^{C}$	0.011

Viscosity parameters	Value
η_1	0.007
η_2	0.005

Table A.4: Bovine femur specimen 2 mechanical properties

Elastic moduli	Value (MPa)
E_1	19100
E_2	10400
v_{12}	0.275
G_{12}	4100
G_{13}	4100
G_{23}	3300

Hashin Strengths	Value (MPa)
X^T	95
X^C	190
X^S	50
Y^T	50
Y^C	105
Y^S	70

Fracture energies per element	Value (N/mm)
$G_{C(1)}^{T}$	0.00475
$G_{C(1)}^{C}$	0.0076
$G_{C(2)}^{T}$	0.00875
$G_{C(2)}^{C}$	0.011

Viscosity parameters	Value
η_1	0.08
η_2	0.05

Table A.5: Bovine tibia specimen from [78] *mechanical properties*

Elastic moduli	Value (MPa)
E_1	23100
E_2	12800
v_{12}	0.275
G_{12}	4300
G_{13}	4300
G_{23}	3400

Hashin Strengths	Value (MPa)
X^T	110
X^C	203
X^S	50
Y^T	60
Y^C	120
Y^S	70

Fracture energies per element	Value (N/mm)
$G_{C(1)}^{T}$	0.0055
$G_{C(1)}^{C}$	0.00812
$G_{C(2)}^{T}$	0.00105
$G_{C(2)}^{C}$	0.0126

Viscosity parameters	Value
η_1	0.075
η_2	0.05

Table A.6: Longitudinal directed crack case study mechanical properties. These mechanical properties are the same as those used for bovine femur specimen 1.

Elastic moduli	Value (MPa)
E_1	18300
E_2	9900
v_{12}	0.275
G_{12}	4100
G_{13}	4100
G_{23}	3200

Hashin Strengths	Value (MPa)
X^T	80
X^C	190
X^S	40
Y^T	50
Y^C	105
Y^S	70

Fracture energies per element	Value (N/mm)
$G_{C(1)}^{T}$	0.004
$G_{C(1)}^{C}$	0.0076
$G_{C(2)}^{T}$	0.0007
$G_{C(2)}^{C}$	0.011

Viscosity parameters	Value
η_1	0.07
η_2	0.05

Table A.7: Irradiated bovine tibia specimen case study mechanical properties

Elastic moduli	Value (MPa)
E_1	23100
E_2	12800
v_{12}	0.275
G_{12}	4300
G_{13}	4300
G_{23}	3400

Hashin Strengths	Value (MPa)
X^T	105
X^C	193
X^S	48
Y^T	57
Y^C	114
Y^S	67

Fracture energies per element	Value (N/mm)
$G_{C(1)}^{T}$	0.003135
$G_{C(1)}^{C}$	0.004628
$G_{C(2)}^{T}$	0.00059
$G_{C(2)}^{C}$	0.007182

Viscosity parameters	Value
η_1	0.048
η_2	0.032